Superconductivity in topological edge states and gated Dayem bridges

Lennart Bours

Superconductivity in topological edge states and gated Dayem bridges

Ph.D. thesis in Nanoscience

by

Lennart Hubertus Iris Bours

Scuola Normale Superiore di Pisa
November 2016 - Februari 2021

Advisor: Dott. Francesco Giazotto
Advisor: Dott. Elia Strambini
SNS Advisor: Prof. Luigi Rolandi

Tiger got to hunt
Bird got to fly
Man got to sit and wonder
Why why why...

— Kurt Vonnegut

Contents

List of publications

A list of the articles published during my PhD, which fall in the scope of the thesis, in chronological order. Throughout the thesis they will be referred to by their Roman numeral.

I. L. Bours, B. Sothmann, M. Carrega, E. Strambini, E. M. Hankiewicz, L. W. Molenkamp, and F. Giazotto — "Topological SQUIPT Based on Helical Edge States in Proximity to Superconductors". Phys. Rev. Applied 10, 014027 - Published 25 July 2018

II. L. Bours, B. Sothmann, M. Carrega, E. Strambini, A. Braggio, E. M. Hankiewicz, L. W. Molenkamp, and F. Giazotto — "Phase-Tunable Thermal Rectification in the Topological SQUIPT". Phys. Rev. Appl. 11, 044073 - Published 23 April 2019

III. L. Bours, M. T. Mercaldo, M. Cuoco, E. Strambini and F. Giazotto — "Unveiling mechanisms of electric field effects on superconductors by a magnetic field response". Phys. Rev. Res. 2, 033353, - Published 2 September 2020

Publications produced during the PhD but not discussed in this thesis.

- L. Bours, S. Guiducci, A. Mreńca-Kolasińska, B. Szafran, J. C. Maan, and S. Heun — "Manipulating quantum Hall edge channels in graphene through scanning gate microscopy". Phys. Rev. B 96, 195423 - Published 15 November 2017

- A. Iorio, M. Rocci, L. Bours, M. Carrega, V. Zannier, L. Sorba, S. Roddaro, F. Giazotto and E. Strambini — "Vectorial Control of the Spin-Orbit Interaction in Suspended InAs Nanowires". Nano Lett. 2019, 19, 2, 652-657 - Published 6 November 2018

List of abbreviations

Throughout this thesis, the following abbreviations will be used:

- BCS: Bardeen Cooper Schrieffer
- DoS: Density of States
- EBL: Electron Beam Lithography
- N: Normal metal
- PMMA: Polymethyl Metacrylate
- S: Superconductor
- SQUID: Superconducting QUantum Interference Device
- SEM: Scanning Electron Microscopy
- TI: Topological Insulator
- TSQUIPT: Topological Superconducting QUantum Interference Proximity Transistor

Chapter 1

Introduction

Superconductivity is a fascinating phenomenon that speaks to the imagination of laymen and experts alike, and has done so for over a century. In 1911, Kamerlingh Onnes was the first to witness the sudden, dramatic disappearance of all resistance that occurs when a material becomes superconducting. What remains is a material in which a current can flow effortlessly and forever. Moreover, a superconductor will generally try to expel any magnetic field from its interior. For certain kinds of superconductors (known as type 2) a magnetic field can penetrate but only in precise and ordered flux quanta. The superconductor will try to prevent the field from moving, which can be utilized to suspend the material mid-air, a phenomenon that is used to great effect at science demonstrations around the globe.

It took 46 years to go from the discovery of superconductivity to the formulation of a microscopic theory by Bardeen, Cooper and Schrieffer in 1957. A feat that was awarded with the Nobel prize for physics in 1972. The microscopic understanding of superconductivity has not reduced the appeal of the effect in the slightest. Rather, it has strengthened it further, as it became clear that superconductivity is a quintessential macroscopic quantum phenomenon. Essentially, the entire superconductor enters a single, macroscopic quantum state. It is one of the rare cases in which quantum mechanics, typically elusive and restricted to the microscopic realm of atoms and electrons, is borne into our macroscopic world.

It is somewhat ironic then, that the contents of this thesis detail physics that only appears when superconductivity is forced back down into the nano-scale. At the same time, it is not very surprising. Science happens where new tools expose new opportunities. For example, it was Kamerlingh Onnes' newfound ability to cool down metals to a few degrees Kelvin, that lead to his discovery. And lately, in solid state physics, it is the little things that matter.

In response to the ever-growing control over the minutia of matter, modern solid state physics has firmly settled in the mesoscopic, a range in

size that that is between the atomic and the macroscopic. While the term is often used loosely[1], it can be taken to indicate lengths from the nanometre (10^{-9} m) to the micrometer (10^{-6} m) or so.[2] Here, on the doorstep to the quantum world, quantum effects typically do not dominate, but they can play an important role. By cleverly arranging matter and taking advantage of quantum interactions, new and exotic qualities can be teased out, or even designed from scratch. Topological insulators are a prime example of this. By growing specific semiconductors on top of each other, with just the right thickness, a material is created that is insulting in its bulk, yet conducting on the surface. These surface states are far from ordinary too, being Dirac fermions protected by time-reversal symmetry. Fundamental for the effect is a very strong spin-orbit effect in combination with carefully chosen confinement.

Here, also superconductivity finds new opportunities. The first half of this thesis is dedicated to the conjunction of an elementary superconductor with a two dimensional topological insulator. As a consequence of the strongly localized nature of the edge states, an unexpected interplay between the superconductor and the topological insulator arises when they are exposed to small magnetic fields, which the former tries to expel. The emergent physics are described, and the electrical and thermal qualities of a device based on this effect are investigated in detail.

The second part of the thesis concerns the effect of strong electric fields on superconducting constrictions made from thin films. While it has long been thought that electric fields have no discernible effects on superconductors, a recent discovery has put this matter into question. In this work, an attempt to settle the ongoing debate around the mechanism behind the unexpected effect is made. To determine whether or not the effect can be explained by a 'trivial' heating by quasi-particle injection, an experiment that utilizes an ionic liquid (an electrolyte) to gate the superconductor –instead of the typical side-, or back-gate– is performed. Thereafter, with the intent to better understand the nature of the effect, it is investigated in combinations with in-, and out-of-plane magnetic fields. The experiment is accompanied by a recently proposed microscopic theory, that is extended to take into account the magnetic field contribution. Here, spin-orbit coupling makes a serendipitous re-appearance, though our understanding is certainly not definitive.

One intriguing question remains: why was the electric field effect not noticed before? Here it is also likely that the confinement of superconductivity to the mesoscopic plays a crucial role. Perhaps its influence reaches only

[1] A more rigorous definition relates the mesoscopic to the electron phase-coherence length, which whose effects were observed, for example, in seminal experiments on universal conductance fluctuations.

[2] For reference, the distance between atoms in e.g. metals is of the order of 10^{-10} m. On the other side, the thickness of a human hair is 10 - 100 micrometer, or 10^{-5} - 10^{-4} m.

over a short distance, and can therefore only dominate in very small devices. Or perhaps something else happens when superconductivity, by its nature an extended effect, is squeezed to –or even just beyond– its limits. Time will tell.

Thesis structure

The thesis is organized as follows. Chapter 2 is a literary review that serves as an introduction to several concepts, such as the proximity effect, 2D topological insulators, and a peculiar 'Doppler shift-like' effect, which form the foundation for chapters 3 and 4. In the latter, a novel device called the topological superconducting quantum interference proximity transistor (or TSQUIPT) is introduced, and its electrical and thermal properties are presented, respectively. Both chapters are theoretical in nature, as the main results are acquired by numerically modelling the proposed device.

Chapter 5 is another literary review that starts with a historical overview of experiments and theories concerning the interplay between electric fields and superconductivity. An introduction to the *electric field effect*, in which all its major characteristics are listed, follows. The chapter ends with a review of an ongoing discussion: whether or not the effect is adequately explained as heating by quasi-particle injection. An exhaustive summary of arguments for and against is given.

The subsequent chapter 6 details an experiment that aims to settle this debate, and preliminary experimental results are presented and discussed. In chapter 7, the field effect is investigated further, by means of an experiment that combines the electric field with in-, and out-of-plane magnetic fields, in an attempt gain new understanding of possibly underlying mechanisms. The experimental results are accompanied by a recently proposed microscopic theory, which is extended to include the effect of an in-plane magnetic field. The thesis is concluded in chapter 8.

Chapter 2

An introduction to the TSQUIPT

2.1 Introduction

In the following chapters, a device that combines a 2D topological insulator (TI) and superconductivity will be presented and discussed. Such a device, dubbed a Topological Superconducting Quantum Interference Proximity Transistor or TSQUIPT has several interesting properties, and aims to probe and possibly exploit a peculiar effect that modifies the density of states of the topological edge channels. In particular, we will explore the effects of a small magnetic field on electrical and thermal transport. We find that the TSQUIPT can be a very sensitive magnetometer, with an estimated sensitivity of $\approx 0.8\ mV/\Phi_0$, which is on par with state-of-the-art SQUIDs [1] and SQUIPTs [2–4]. Moreover, the TSQUIPT acts as a thermal rectifier, and as the TSQUIPT's density of states can be easily tuned via an external magnetic field, it can also provide active control over electronic heat flow

In this chapter, a short overview of concepts that underlie the physics present in the TSQUIPT, such as 2D TIs, and the superconductor proximity effect, is given. This will lay the groundwork for the discussion of electrical and thermal properties of the TSQUIPT, which will be introduced and studied in the following chapters.

2.2 2D Topological Insulators

The past decade has seen an immense interest in the physics of topological insulators, due to their potential applications in nano-electronics, spintronics and quantum computation, as well as their rich fundamental physics. [5–9]

A topological insulator (TI) is a material that is insulating in its bulk, while its surfaces (for a 3D TI) or edges (for a 2D TI) host conductive states, see Fig. 2.1 for a schematic illustration of the band diagram. Topological

insulators are special in that their surface states are a direct consequence of their bulk band structure. Moreover, because the states feature spin-momentum locking, they are protected by time-reversal symmetry. As a result, electron scattering is strongly suppressed. The only available states have opposite momentum and spin, and for such a scattering event to occur, time-reversal symmetry must be broken by e.g. a magnetic impurity.

The occurrence of time-reversal symmetry protected edge states was first predicted for HgTe/CdTe quantum wells in 1987 [10], and subsequently the study of topological transport and by extension 2D and 3D TIs gained a renewed interest around 2005, due to the discovery of graphene and the investigation of quantum spin Hall phase it can host [11–18]. The topological properties of HgTe/CdTe quantum wells were experimentally confirmed via transport in 2007 [19], and spectroscopic measurements shortly thereafter [20, 21]. Since then, many topological materials, both 2D and 3D in nature have been identified.

Besides HgTe/CdTe 2D TIs [19, 22–26] there also exist InAs/GaSb [27–33] quantum wells which exhibit a similar behaviour. However, there are significant differences in the underlying band structure. In the case of HgTe/CdTe structure, the effect is driven by a strong spin-orbit interaction, that drives the electron band down –and the hole band up– in energy. This, together with confinement leads to the topological phase. InAs/GaSb structures are based on the fact that the bottom of the electron band in InAs, lies slightly below the top of the hole band in GaSb. The electronic states in the InAs and GaSb are then confined such that only one electron and one hole state remain in the InAs and GaSb respectively. The two materials are grown on top of each other such that the two states hybridize, which leads to helical edge modes around the interface. The discussion here is presented with HgTe/CdTe quantum wells in mind.

HgTe/CdTe quantum wells

CdTe is a semiconductor with a 1.6 eV bandgap between the $l = 1$, $J = 3/2$, hole-like valance Γ_8 band and the $l = 0$ electron-like Γ_6 band, see the right panel in Fig. 2.2a. In HgTe the Γ_8 hole-like bands have been lifted above the Γ_6 electron-like band due to a strong spin-orbit interaction. The material ends up being a zero-gap semiconductor, where the conduction band is the light hole subband of Γ_8, while the valance band is the heavy hole subband of Γ_8, see the left panel of Fig. 2.2a.

When these two materials are in contact which each other, the bands will be continuously connected, which leads to a crossing of the Γ_6 and Γ_8 bands at the interface. By sandwiching HgTe between two layers of CdTe, a quantum well is created, as shown in Fig. 2.2b. If the width of the quantum well (i.e. the thickness of the HgTe layer) is smaller than the critical thickness $d_c = 6.3$ nm, the order of the electronic states will be reversed again back to

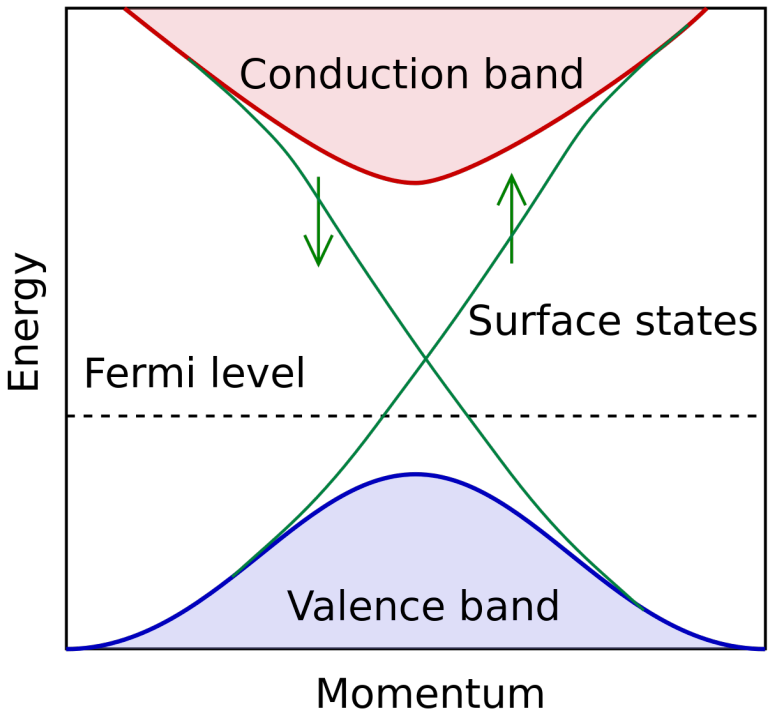

Figure 2.1: A schematic representation of the band structure of a topological insulator. The bulk features a typical insulator band structure, while the surface hosts special states with energies that lie within the bulk band gap that allow normal conduction. These states are subject to spin-momentum locking, meaning that their spin is fixed with respect to their momentum.

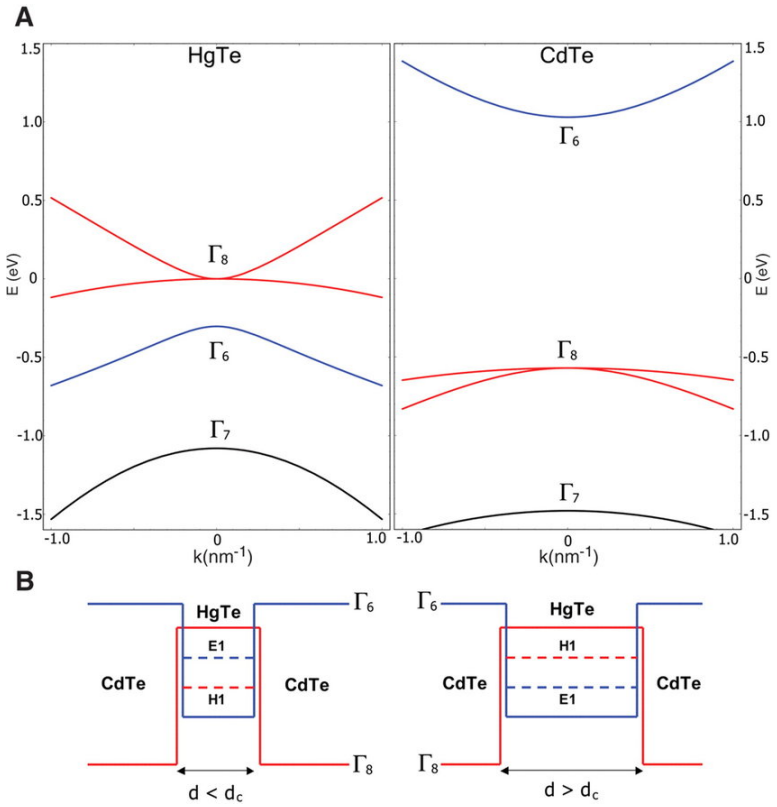

Figure 2.2: a) a schematic illustration the band structure of CdTe near the Γ point, and the band structure of HgTe near the Γ point. b) the HgTe/CdTe quantum well band structure for a thickness $d < d_c$ (normal states) and $d > d_c$ (inverted states).

the normal ordering (hole states below electron states) due to the confinement energy contribution. If on the other hand, the thickness of the HgTe layer is larger than d_c, the electron and hole states remain inverted.

The end result is a 2D layer, in which transport takes place only via the edges of the sample. Due to the strong spin-orbit coupling, the spin and momentum degrees of freedom in the edge states are locked, resulting in helical edge channels [34], i.e., one channel is a spin up state, while the other is spin down. Thus, each edge of a 2D TI hosts one pair of counter-propagating edge states, that have opposite spin [24]. The helical edge states are protected against backscattering by time-reversal symmetry, which guarantees robustness against disorder and perturbations which do not break this symmetry, e.g., non-magnetic impurities. A large number of studies has been put forward on the nature of helical edge states of TIs, including the role of e-e interactions [35–37], breaking of time-reversal symmetry [38–40], and spin properties [41].

2.3 The proximity effect

The term *Holm-Meissner effect* or, more commonly, *proximity effect* is used to describe the phenomenon in which superconductivity 'spills over' into a normal conductor that is in clean contact with a superconductor. [42–45] Due to the non-local, coherent nature of superconductivity, the correlations between electrons forming Cooper pairs can be maintained outside the superconductor, albeit only over short distances. Electron scattering in the normal conductor will lead to the loss of coherence, limiting the induced superconducting correlations to distances over which the coherence can be maintained. The strength of the effect depends on factors such as the paring strength in the superconductor, the volume ratios between the two materials, the quality of the interface, and the coherence length in the normal conductor.

Microscopically, the proximity effect can by understood as a process called Andreev reflection. An electron in the normal conductor that has an energy in the superconducting gap, cannot directly enter the superconductor, as no states are available at its energy level. At the Superconductor-Normal interface, it can either be reflected normally, or enter the superconductor together with another electron with which it can form a pair. In this case, the electron is effectively reflected from the Normal-Superconductor interface as a hole, such that a Cooper pair enters the superconductor. [46]

As a consequence of the effect, the density of states of the normal conductor is changed close to the N - S interface, and a finite pair amplitude is induced. [47–50] The induced superconducting correlations vary depending on the the strength of the proximity effect, and the distance from the interface. By connecting two superconductors via a short normal link, a so-called Superconductor-Normal-Superconductor (S-N-S) junction is created. Then, if the coherence length is of the same order or larger than the length of the weak (i.e., normally less or not superconducting) link, electrons are Andreev reflected back and forth, which leads to the formation of Andreev bound states. These states can carry a supercurrent through the 'normal' or 'weak' region, and, like Cooper pairs, do not carry heat.

As with the S-N interface, also in the S-N-S junction the density of states is affected; a so-called 'mini-gap' is generated therein. The amplitude of this mini-gap is also dependent on the superconducting phase difference between the two leads. It is maximized at $\phi = 0$, and it disappears completely if $\phi = \pi$. [49,50] The presence or absence of such a gap has drastic consequences for electrical and thermal transport [51–53], including properties such as the electronic entropy, relaxation mechanisms, and specific heat of the weak link [54–56]. By controlling the superconducting phase difference, one can manipulate these qualities, varying them between normal-like and superconductor-like.

One convenient way in which the phase ϕ can be controlled, is by closing the two superconducting leads into a ring that is interrupted by the proxi-

mized link. The phase difference is then directly linked to the magnetic flux penetrating the ring due to fluxoid quantization, and can thus be controlled via an external magnetic field in a straightforward manner.

2.4 The SQUIPT

The magnetic flux dependence of the mini-gap induced in an S-N-S junction can be observed and exploited via tunnel spectroscopy on the weak link (i.e. the normal metal) that interrupts a superconducting ring. Such a device is called a Superconducting QUantum Interference Proximity Transistor, or SQUIPT. [57] The absence or presence of the mini-gap has a strong effect on the quasi-particle transport. As a result, the current-voltage characteristics of a SQUIPT depend strongly on the flux through the ring, and the device can be used as an extremely sensitive magnetometer. Furthermore, since only quasi-particles contribute to electronic thermal transport (i.e., Cooper pairs and Andreev bound states do not), the thermal conductance of the weak link is strongly suppressed by the presence of a gap in the density of states. One can thus 'enable' or 'disable' the heat flow through such a device via an external magnetic field. [53]

2.5 Superconductivity in 2D topological insulators

By bringing superconductors and TIs into contact, Superconducting correlations can be induced in the edge channels of the TI via the proximity effect, combining their qualities [58–64]. Compared to superconductivity induced in normal metals or semiconductors, the superconductivity induced in TIs is particularly interesting because it can exhibit both the conventional spin-singlet s-wave pairing, as well as spin-triplet p-wave pairing due to the strong spin-orbit coupling in the TI and particular nature of the edge states.

For this reason, topological Josephson junctions (TJJ) where two superconducting electrodes are coupled to each other via the edge states of a TI to form an S-TI-S junction, have attracted much attention. The presence of p-wave pairing enables, under suitable conditions, the creation of Majorana-like modes in the form of topologically protected zero-energy Andreev bound states [65, 66]. These Majorana modes carry a 4π-periodic Josephson current [67–70], a feature which has been observed in experiment recently [71–73]. Furthermore, they are responsible for a 'zero-bias' peak in the conduction, an anomalous current-phase relation [74, 75] and can be identified by their unique phase-dependent thermal conductance [76].

2.6 The Doppler effect

A Superconducting Quantum Interference Device or SQUID, is a device in which a superconducting ring is interrupted by two tunnel junctions. It was first produced shorty after the discovery of the Josephson effect, and is widely used as a sensitive magnetometer. If a magnetic flux penetrates the superconducting ring, a circulating supercurrent is induced due to fluxoid quantization. The size and sign of the induced current depends on the amount of flux through the junction. The current is zero for multiples of the magnetic flux quantum $\Phi_0 = h/(2e)$, and maximum when the flux is an odd multiple of $\Phi_0/2$.

At first glance, a TJJ appears just like a SQUID. The centre of the TI is insulating, and forms the inside of the ring, while the proximized TI edge states form two weak links. The superconducting leads close the ring, and thus a loop with a continuous superconducting phase is created, that will respond to a magnetic flux through the TI interior.

However, the underlying helical nature of the edge channels modifies the quantum interference that determines how the TJJ responds to a magnetic flux compared to a normal SQUID. [77] One difference between the TJJ and the classical SQUID is that the supercurrent in the latter features a cosine-like dependence on the magnetic flux enclosed by the ring. This is a reflection of the sinusoidal Josephson current-phase relation which is associated with electronic states that have an energy close to or above the superconducting gap. The TJJ on the other hand, also features subgap Andreev bound states that do not only have an energy within the superconducting gap, but are also protected by time-reversal symmetry i.e., not disrupted by non-magnetic disorder. These states are highly anharmonic (sawtooth like) with respect to the Josephson phase difference. [67–70, 78]

When carefully modelling a TJJ in a small, out-of-plane magnetic field with the aim of investigation its SQUID-like features and the influence of the particular subgap Andreev bound states, a previously overlooked 'Doppler shift-like' effect was found. [77] The effect originates from the shielding current that expulses the magnetic field from the superconducting leads, something which is generally not taken into account. It affects the Andreev bound states' energy levels and interference patterns.

Fig. 2.3 sketches a TJJ in an out-of-plane magnetic field $\vec{B} = (0, 0, B)$. The junction has a width W along the y axis and length L along the x axis. The width of the superconducting leads is taken to be the same as that of the junction. A type-I superconductor will always try to fully expel a magnetic field from its interior. For this purpose, a supercurrent that generates a magnetic field opposite to the external one will be induced at the superconductor surface, which is accompanied by a gradient in the superconducting phase. The supercurrent along the edges of the leads

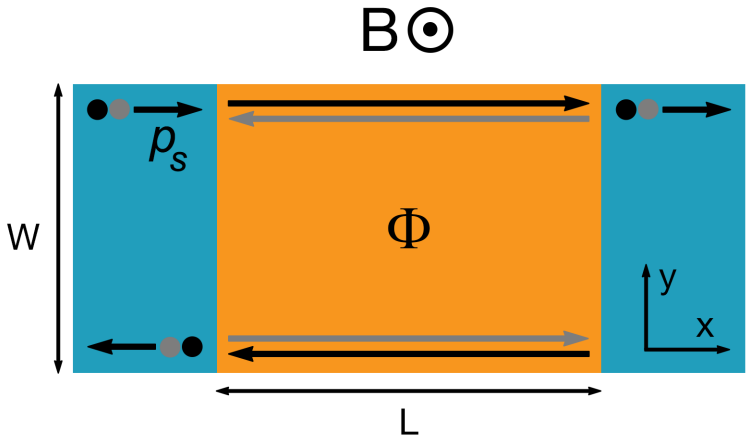

Figure 2.3: A schematic illustration of a topological Josephson junction. Two superconducting leads (blue) contact a 2D Ti (orange). An out-of-plane magnetic field B, induces a screening response in the superconducting leads that leads to a Cooper pair momentum p_S along the edges of the leads. A magnetic flux Φ penetrates the central region of the TI.

correspond to a Cooper pair momentum p_s

$$p_s = -\frac{2e}{c} A_x(\pm\frac{W}{2}) = \pm\pi\hbar\frac{BW}{\Phi_0}, \tag{2.1}$$

where e is the electron charge, c is the speed of light, A_x is the x component of the magnetic vector potential $\vec{A} = (-yB, 0, 0)$. The + and - sign refer to the upper and lower edge respectively. p_s can be rewritten in terms of the flux through the junction Φ, which depends on the distance over which the magnetic field is screened in the leads. For simplicity, it is assumed that the spatial variation of the screening can be neglected, which is a reasonable assumption for a narrow, thin film junction. For more details see Ref. [77] and chapter 3.

The Cooper pair momentum modifies the Andreev reflection amplitudes, and by extension the energy level of the Andreev Bound states in the junction. These can therefore be controlled by a small magnetic field. Moreover, left and right moving electrons acquire a different momentum shift under Andreev reflection due to the relative opposite sign of the Cooper pair momentum shift, an effect similar to the classical Doppler shift.

While the screening response in the superconducting leads is completely general, it is interesting mainly in combination with the 2D TI. The latter's particular transport characteristics, i.e., the strongly localized and helical edge states, mean that there is no destructive interference, and the two channels are effected oppositely. By comparison, if a wide S-N-S junction is exposed to a magnetic field, the supercurrent through the junction quickly

cancels out due to quantum interference, yielding the well known Fraunhofer pattern.

Remarkably, the Doppler effect allows one to shift the Andreev bound states, effectively closing the induced superconducting gap, via small magnetic fields of only a few mT that do not suppress the helical edge conductance [79]. This effect can be exploited, for instance, to manipulate the thermal conductance of the junction. While the thermal conductance is exponentially suppressed in the presence of a superconducting gap, it is twice the thermal conductance quantum when the gap is closed and both edge channels contribute to energy transport. A TJJ can thus be employed as a thermal switch [80, 81].

2.7 Summary and conclusions

Several physical phenomena, such as 2D topological insulators, the superconducting proximity effect, and the interaction between the two have been introduced. The combination of superconductors and 2D TIs leads to a surprising magnetic field response; the 'Doppler effect'. It arises from the interplay between the screening currents induced in a supercurrent by magnetic fields, and the strongly localized edge channels of the TI. The end result is that the Andreev bound states in the edge channels are modified in the presence of small magnetic fields.

In the following chapters, a device based on these phenomena, the Topological Superconducting QUantum Interference Proximity Transistor or TSQUIPT, will be discussed in detail, and its electrical and thermal properties will be presented.

Chapter 3

Electrical Transport in the TSQUIPT

The contents of this chapter are based on the article *Topological SQUIPT Based on Helical Edge States in Proximity to Superconductors.*

3.1 Introduction

In this chapter the impact of the Doppler shift on the proximized density of states (DoS) of the 2D TI edge-states is investigated, and a device based on this effect theoretically examined and discussed. The quantum interference of supercurrents carried by the two edges of the topological Josephson junction has been studied by analysing their dependence on the flux that penetrates the TI [77, 82]. Here we aim to probe the density of states of a single proximized edge via a normal tunnel probe, see Fig. 3.1. In essence the proposed device realizes a Topological variant of the Superconducting Quantum Interference Proximity Transistor [2–4, 57, 83–93] or TSQUIPT. These devices are known for their extremely low flux noise, which means they can be used as incredibly sensitive magnetic field detectors.

In the case of the TSQUIPT, not a normal metal, but the 2D TI edge channels are proximized, and their DoS depends on both the induced superconducting corrolations and the underlying properties of the edge states. As the two TI edges, together with the superconducting leads, naturally form a ring, the superconducting phase is dependent on the flux through the surface of the TI. We characterize the TSQUIPT and its performance, and present calculations of the expected device behaviour in transport experiments.

In the following section, we will describe the model and sketch the basic equations for helical edge states in proximity to two superconductors. These are then used to derive the expression for the DoS which will be investigated in detail in Sec. 3.3 by inspecting the transport properties of a tunnel-coupled metallic probe. The electrical response of the TSQUIPT will be presented,

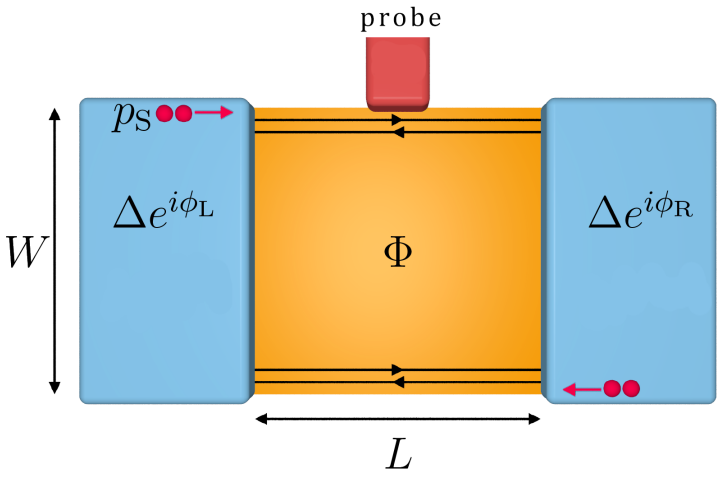

Figure 3.1: A schematic illustration of the proposed device. A topological Josephson junction is formed by two superconducting leads (blue) coupled via a 2D topological insulator (orange) of width W and length L. Transport through the topological insulator occurs via two helical edge states at the boundary of the insulator. A normal probe terminal (red) is tunnel coupled to the edge states via a tunnel barrier. A magnetic flux Φ through the junction gives rise to a finite Cooper pair momentum p_S in the superconducting leads.

together with the implementation of an absolute magnetometer, that has an optimum sensitivity comparable to state of the art commercial SQUIDs. Future prospects are discussed and results are summarized in Sec. 3.4.

3.2 Model

We consider a topological Josephson junction consisting of two superconducting electrodes deposited on top of a 2D TI of length L and width W as depicted in Fig. 7.1. We assume that the width of the 2D TI is so large that an overlap or coherent coupling [82] between edge channels from different edges can be neglected. The width of the edge channels is generally taken to be ~ 100 nm. [23, 26, 94, 95] Increasing the width of the device does not negatively influence the behaviour or performance of the proposed device. Furthermore, we also neglect any coherent coupling of the edge states via the superconductor which is a valid assumption if the junction is sufficiently wide. A normal metal probe is weakly tunnel-coupled to the upper edge of the junction. Assuming that both superconductors are kept at the same electrochemical potential, $\mu_{\mathrm{S}} = 0$ one can inject a charge current from the probe into the Josephson junction by applying a bias voltage $V = \mu_{\mathrm{N}}/e$ to the probe terminal.

The left (L) and right (R) superconducting leads are characterized by a superconducting order parameter $\Delta e^{i\phi_{\mathrm{L,R}}}$, and induce superconducting correlations in the edge channels via the proximity effect [96]. It is assumed that the order parameter changes at the superconductor-topological insulator interface on a length scale shorter than the superconducting coherence length $\xi_0 = \hbar v_{\mathrm{F}}/\Delta$, where v_F is the Fermi velocity, so that the spatial variation of the order parameter can be modelled as $\Delta(x) = \Delta[\Theta(-x - L/2)e^{i\phi_{\mathrm{L}}} + \Theta(x - L/2)e^{-i\phi_{\mathrm{R}}}]$, where $\Theta(x)$ is the Heaviside step function. Proximity effects inside the junction, that would require a self-consistent evaluation of the order parameter, are neglected. This is a reasonable approximation since transport through the junction proceeds via the two edge channels only [97]. The proximized non-interacting helical edge states[1] at the upper edge are described by the Bogoliubov-de Gennes Hamiltonian

$$H_{\mathrm{BdG}} = \begin{pmatrix} h(x) & i\sigma_y\Delta(x) \\ -i\sigma_y\Delta(x)^* & -h^*(x) \end{pmatrix}. \tag{3.1}$$

The diagonal terms describe the single-particle hamiltonian of the two edge channels and read

$$h(x) = v_{\mathrm{F}}\sigma_x\left(-i\hbar\partial_x + \frac{p_{\mathrm{S}}}{2}\right) + \sigma_0\mu, \tag{3.2}$$

[1] Here for sake of simplicity the discussion is limited to the non-interacting case, neglecting possible e-e interactions within edge channels.

with v_{F} the Fermi velocity, σ_0 the (2 by 2) identity matrix and σ_j the Pauli matrices acting on spin space, and the chemical potential μ. We have introduced

$$p_S = \frac{\pi\hbar}{L}\frac{\Phi}{\Phi_0} = \frac{\pi\xi_0\Delta}{v_F L}\frac{\Phi}{\Phi_0} \tag{3.3}$$

which denotes a finite Cooper-pair (condensate) momentum along the transport direction, which arises in the presence of a finite magnetic flux Φ through the junction. While the momentum can be formulated in terms of the magnetic field B and the width W of the junction only, we will always express it and other quantities in terms of the flux Φ through the junction, and the length L of the junction, assuming the width W is a constant.

When Andreev reflection occurs in the presence of a magnetic flux Φ, it is modified by the finite condensate momentum induced in the leads. The left and right moving particles in the edge channels each pick up a shift in momentum $p_S/2$ (with opposite sign respectively) upon reflection, an effect which is reminiscent of the Doppler shift. The Cooper pair momentum relevant for transport properties along the edge channels is determined by the width of the 2D TI weak link (W) as long as the superconductor width exceeds that of the TI. Moreover, as we take W to be much larger than the spatial extension of the edge states, the Cooper pair momentum is taken at the boundary, i.e. $y = W/2$.

In addition to inducing a finite Cooper pair momentum, the magnetic field also affects the Josephson phase difference $\phi_{\mathrm{R}} - \phi_{\mathrm{L}}$. The phase difference depends on the effective area of the junction which depends on the magnetic field screening in the leads. For simplicity it is assumed that this screening can be neglected, i.e., that the flux through the junction is defined by the TI geometry $\Phi = WLB$. This is a reasonable assumption if the width of the leads is small compared to the Pearl penetration depth [98], which is the relevant screening length for thin films where $d \ll \lambda_L$. In other words, it is assumed that $W/(2\lambda_P) \ll 1$, with $\lambda_P = 2\lambda_L^2/d$. Here λ_L is the London penetration depth and and d is the film thickness. The gauge invariant phase difference can then be derived to be $\phi_u = \phi_0 + \pi\frac{\Phi}{\Phi_0}$ across the upper edge, and $\phi_l = \phi_0 - \pi\frac{\Phi}{\Phi_0}$ across the lower edge. ϕ_0 denotes a possible extra phase difference that is not a consequence of the magnetic flux through the junction. For the complete derivation see the appendix of Ref. [77].

The eigenfunctions of the Bogoliubov-de Gennes Hamiltonian in an infinite superconductor with phase ϕ_i in Nambu notation are given by

$$\psi_1(x) = (u_-, u_-, -e^{-i\phi_i}v_-, e^{-i\phi_i}v_-)^T e^{ik_e x}, \tag{3.4}$$

$$\psi_2(x) = (v_-, v_-, -e^{-i\phi_i}u_-, e^{-i\phi_i}u_-)^T e^{ik_h x}, \tag{3.5}$$

$$\psi_3(x) = (u_+, -u_+, e^{-i\phi_i}v_+, e^{-i\phi_i}v_+)^T e^{-ik_e x}, \tag{3.6}$$

$$\psi_4(x) = (v_+, -v_+, e^{-i\phi_i}u_+, e^{-i\phi_i}u_+)^T e^{-ik_h x}, \tag{3.7}$$

describing right- moving electron-like, left-moving hole-like, left-moving electron-like and right-moving hole-like quasiparticles, respectively. In the above equations we have introduced

$$u_{\pm} = \frac{1}{2}\left(1 + \frac{\sqrt{E_{\pm}^2 - |\Delta|^2}}{E_{\pm}}\right), \tag{3.8}$$

$$v_{\pm} = \frac{1}{2}\left(1 - \frac{\sqrt{E_{\pm}^2 - |\Delta|^2}}{E_{\pm}}\right), \tag{3.9}$$

with $E_{\pm} = E \pm \frac{v_{\mathrm{F}} p_S}{2}$ and $k_{e,h}$ the wavevector associated to electron and hole-like quasiparticle, respectively. To find the wavefunction in all three regions (right lead, TI and left lead) we take the wave-matching approach at the S-2D TI interfaces assuming for simplicity, ideally transparent interfaces. Let us consider the case of an electron-like quasiparticle impinging on the junction from the left. The wave functions in the three different regions, i.e., left superconductor (S,l), the central (2DTI), and right superconductor (S,r) of the junction can be written as

$$\psi_{\mathrm{S,l}}(x) = \psi_1(x) + r_e\psi_3(x) + r_h\psi_2(x), \tag{3.10}$$

$$\psi_{\mathrm{2DTI}}(x) = \sum_i a_i\psi_i(x), \tag{3.11}$$

$$\psi_{\mathrm{S,r}}(x) = t_e\psi_1(x) + t_h\psi_4(x). \tag{3.12}$$

Here r_e, r_h, t_e and t_h represent the reflection and transmission coefficients for electron-like and hole-like quasiparticles. Taking into account the continuity of the wave function at the interfaces, we obtain the wave function in the central region, which provides direct access to the transmission probability of quasiparticles through the junction. We remark that while the normal state transmission of a 2D TI equals unity due to Klein tunnelling preventing backscattering in the presence of time-reversal symmetry, the transmission in the superconducting state depends on energy, phase difference and magnetic flux in a non-trivial way, due to interference effects [80]. These quantum interferences also manifest themselves in the density of states of the junction.

Writing the wave function of the central region as $\psi_{\mathrm{2D\ TI}} = (u_\uparrow, u_\downarrow, v_\uparrow, v_\downarrow)$, the corresponding density of states of the upper edge channel inside the junction is given by

$$\rho(E) = \sum_{k,\sigma,\eta=\pm} \left[|u_\sigma|^2\delta(E - E_{k\eta}) + |v_\sigma|^2\delta(E + E_{k\eta})\right], \tag{3.13}$$

where $E_{k\pm} = \sqrt{(v_{\mathrm{F}}k \pm \mu)^2 + \Delta^2} \pm \frac{v_{\mathrm{F}} p_{\mathrm{S}}}{2}$. The + and − refer to left- and right-moving quasiparticles, respectively. Due to the counter-propagating

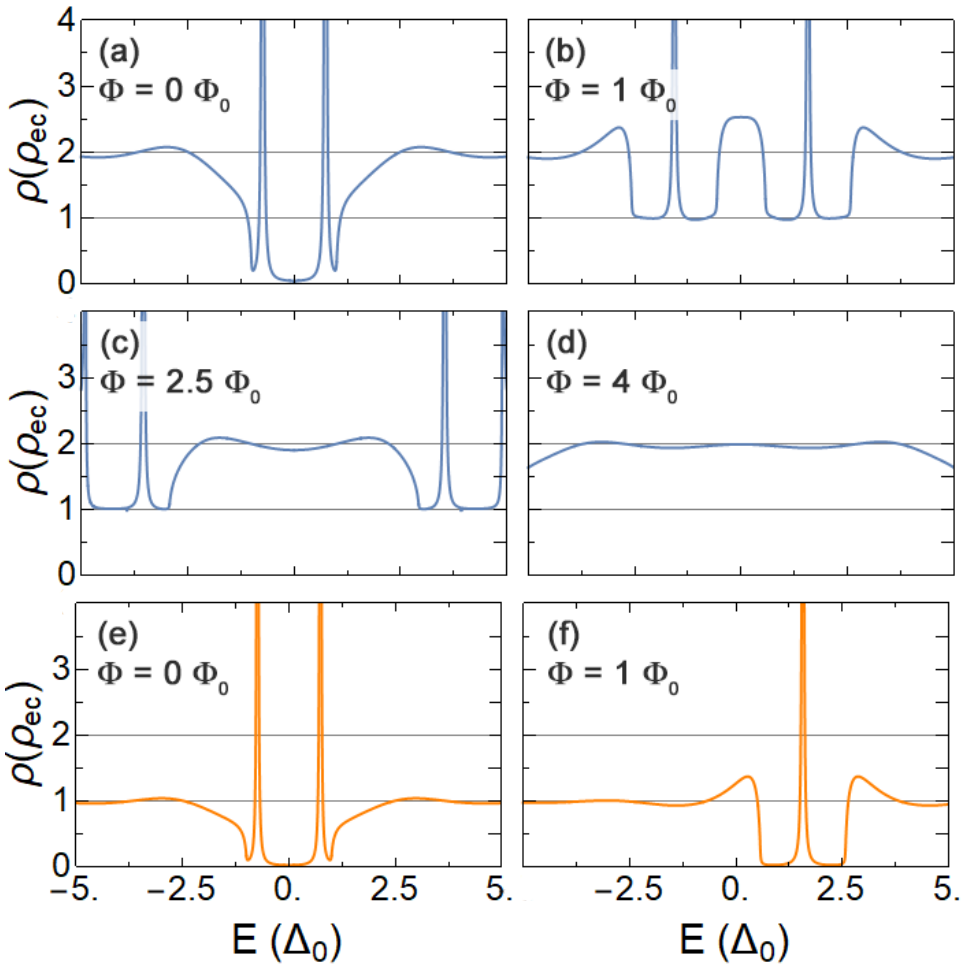

Figure 3.2: (a) - (d) the density of states of the topological Josephson junction as a function of energy, for a junction with $L = \xi_0$ and $\phi_0 = 0$, for various values of the flux Φ through the junction. For zero flux, the DoS is gapped. Andreev bound states create sharp peaks in the DoS. When a flux is applied, the DoS of left and right movers shift in opposite directions, effectively closing the gap. The interference effects are centred around the superconducting gap, and as the DoS are shifted further in energy, they fade away. The arrows in Fig. 3.3 (b) indicate the position of these cuts in the density plot. (e), (f) The density of states of only one of the two channels, i.e. only the left movers. The position of the cuts is indicated by the arrows in Fig. 3.3 (d).

nature of helical edge states, the left and right movers are shifted opposite in energy by $\pm\frac{v_F p_S}{2}$.

Including the contributions for quasiparticles of both types impinging from the right-hand side and performing the sum over momenta, we obtain the density of states $\rho(E)$ of the 2D topological Josephson junction in units of $\rho_{ES} = (\pi\hbar v_F)^{-1}$, the density of states per unit volume of a single edge channel. For energies above the superconducting gap, we find

$$\rho(E) = \sum_{\sigma=\pm} \rho_{BCS}(E_\sigma) F_\sigma(E_\sigma) \tag{3.14}$$

where

$$\rho_{BCS}(E) = \frac{|E|}{\sqrt{|E|^2 - \Delta^2}} \Theta(|E| - \Delta), \tag{3.15}$$

is the BCS density of states. The function

$$F_\pm(E) = \frac{E^2 - \Delta^2}{E^2 - \Delta^2 \cos^2(\frac{\phi_u}{2} \pm \frac{EL}{\Delta\xi_0})} \tag{3.16}$$

is a modulating function which originates from quantum interference via Andreev reflections with the TI edge. We underline that the energy-dependent term inside the cosine arises from the energy dependence of the electron-like and hole-like wave vectors and, from a physical point of view, reflects an additional phase picked up by an electron-hole pair making a round-trip through the junction. Note that the density of states inside the gap is obtained from Eq. 3.14 in a standard way via analytic continuation $E \to E + i0^+$, and can be expressed in an analogous form.

The proximity induced density of states, shown in Fig. 3.3 for junctions of various lengths, shows features that are worth discussing in detail. For clarity, Fig. 3.2 shows several cuts of the DoS, and their position is indicated by the black arrows in Fig. 3.3a and d. As one can see from the above expression, the full density of states is given by a sum of two BCS-like contributions, each corresponding to one of the edge channels. In response to a flux, the two are shifted in energy in opposite directions. There is also a modulating factor due to quantum interference effects, which can be seen as the continuation of the Andreev bound states into the continuum above the superconducting gap. Fig. 3.3d shows the DoS of one of the edge states.

Looking at Fig. 3.3 one can see that in the central diamond energies are smaller than the superconducting gap and both channels are closed. Inside this region sharp discrete peaks appear in the density of states due to the formation of Andreev bound states inside the junction. In the dark blue, diagonal regions, one of the two channels is opened due to an interplay between the particle energy and the Doppler shift. The slope α of the regions is inversely proportional on the device length, $\alpha = \pm\frac{1}{L}\frac{\pi\xi_0\Delta}{v_F\Phi_0}$.

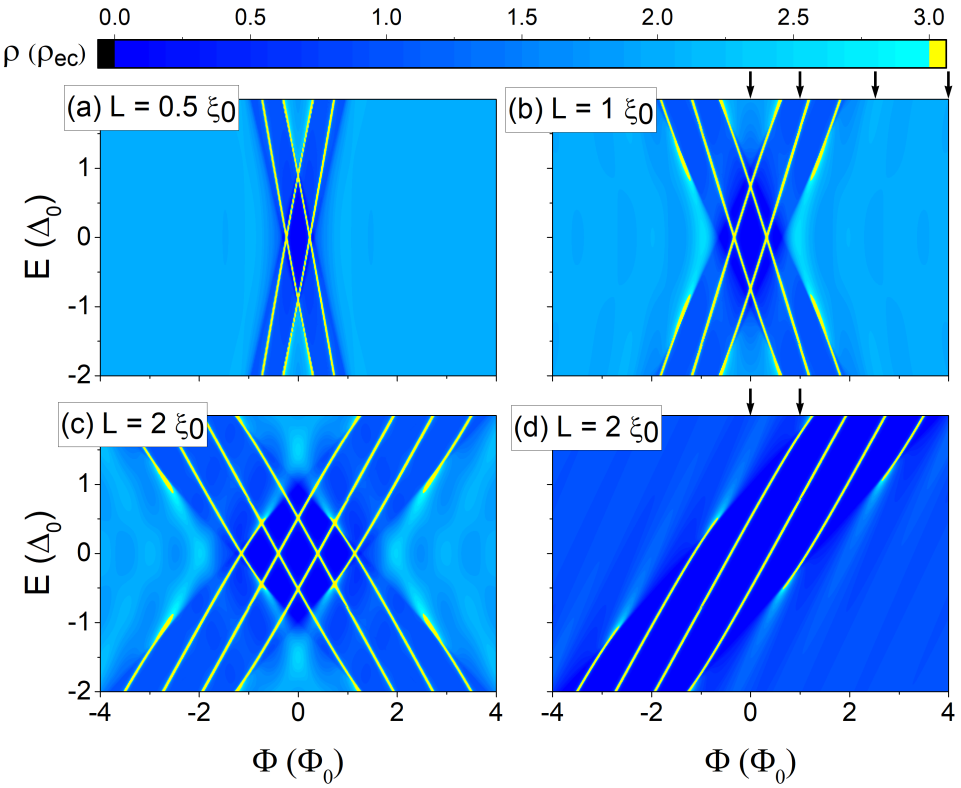

Figure 3.3: Density of states of the topological Josephson junction as a function of energy, in units of the density of states of a single edge channel in its normal state, and magnetic flux, in units of the flux quantum. Andreev bound states appear as sharp lines inside the gapped regions and transform into broad, decaying resonances outside the gap. The superconducting phase difference without flux is $\phi_0 = 0$ for all plots. The complete density of states is shown for a junction length of (a) $L = 0.5\,\xi_0$, (b) $L = \xi_0$ and (c) $L = 2\,\xi_0$. In (d) the contribution to the density of states of left movers alone is shown. The arrows above (b) and (d) indicate the position of the cuts shown in Fig. 3.2

For large magnetic fluxes, both channels are opened as the Doppler shift becomes larger than the gap. This state corresponds to the light blue regions. In addition, for large energies both channels are also open since the electron-like (hole-like) energy exceeds the induced superconducting gap. An additional modulation appears in the density of states (more noticeable for long junctions) which stems from the energy dependence of the electron-like and hole-like wave vectors. The slope of these oscillations is twice the one of the arms themselves.

The density of states depends on the various system parameters in a non-trivial way. Increasing the junction length L while keeping its width W and the magnetic field B fixed leads to a linear increase of Φ. Furthermore, both the frequency and the strength of the oscillations arising from the energy-dependence of wave vectors increase. Similarly, increasing the junction width W at constant L and B gives rise to an increased flux as well as to a growing Cooper pair momentum p_S. Finally, changing B at fixed L and W yields a change of both the magnetic flux and the Cooper pair momentum.

Further control over the density of states can be obtained by tuning the phase difference ϕ_0. It can be exploited to move the BCS singularities in the density of states as shown in Fig. 3.4. Experimentally, ϕ_0 can be controlled by imposing a supercurrent between the superconducting leads, or alternatively by closing the two leads in a loop. In the latter case the magnetic field also determines ϕ_0 through flux quantization. In the following discussion, for sake of clarity, we restrict the discussion to $\phi_0 = 0$, the extension to finite ϕ_0 being straightforward.

3.3 Device characteristics

Besides hosting physics that are interesting from the fundamental point of view, the TSQUIPT can also be used as an *absolute* magnetometer due to its non periodic flux dependence. By tracing the device response to an applied flux, one can determine the absolute flux, and by extension the magnetic field to which the device is exposed. This is unlike the behaviour of Superconducting Quantum Interference Devices (SQUIDs) and SQUIPTs, though a similar behaviour can be achieved by designing an array of SQUIDs. [99, 100] Contrary to typical flux sensitive devices, no ring structure has to be fabricated, as the edge channel transport of the 2D TI naturally provides a robust 'ring' for the current. Moreover, the device sensitivity can be tuned via a bias current.

In order to probe the density of states in the topological edge channels, we consider a normal metal probe weakly tunnel-coupled to the side of the TI, with a constant density of states equal to unity, see Fig. 3.1. In this section, the proposed TSQUIPT and its theoretical performance are characterized by analysing the charge current through the probe terminal for different device

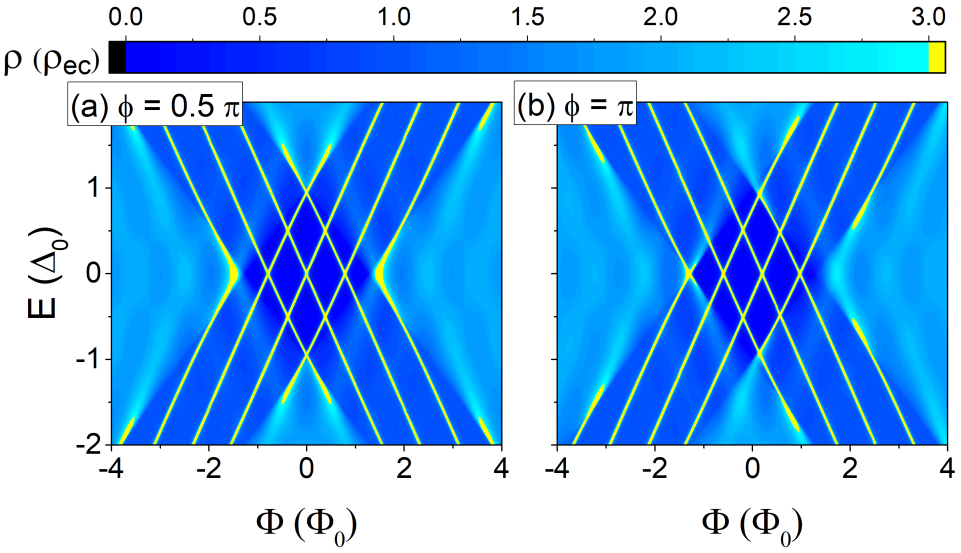

Figure 3.4: Density of states of the topological Josephson junction for a junction length of $L = 2\,\xi_0$ with (a) the superconducting phase difference $\phi_0 = \pi/2$ and (b) $\phi_0 = \pi$. The ϕ_0 dependence is $2\,\pi$-periodic and shifts the position of the Andreev bound states.

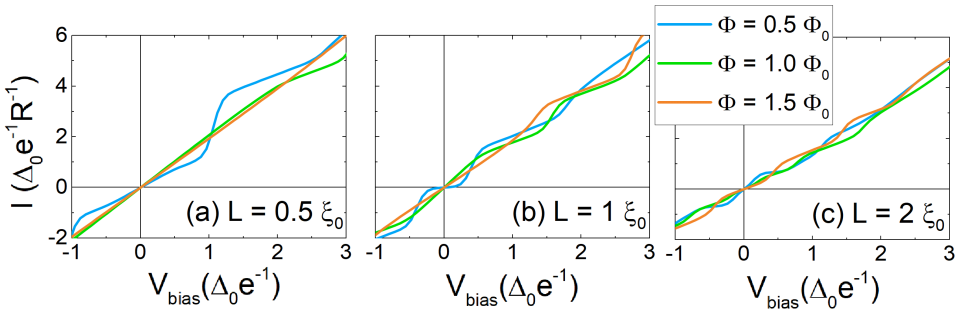

Figure 3.5: I-V characteristics at various fluxes. Different panels correspond to different junction lengths: (a) $L = 0.5\,\xi_0$, (b) $L = \xi_0$ and (c) $L = 2\xi_0$. All curves are calculated for a temperature $T/T_C = 0.1$ where T_C denotes the critical temperature of the superconductors. The current and bias voltage are normalized in units of the superconducting gap at zero temperature Δ_0, the electron charge e and the tunnel junction resistance R.

lengths, temperatures, fluxes and biasing conditions.

The general expression for the charge current injected from the tunnel probe is given by [101]

$$I(V) = \frac{1}{eR} \int dE\, \rho(E)\, [f_{\mathrm{N}}(E) - f_{\mathrm{S}}(E)] \tag{3.17}$$

where $f_i(E) = \{\exp[(E - \mu_i)/(k_{\mathrm{B}}T)] + 1\}^{-1}$ denotes the Fermi functions of the normal probe ($i = \mathrm{N}$) and the superconductors ($i = \mathrm{S}$), respectively, and R is the resistance of the tunnel barrier. The resulting charge current is plotted in Fig. 3.5 for various junction lengths and fluxes. It is shown that a smaller flux is required to open both channels in the case of short junctions. This is a result of comparing junctions of different length, but of the same width. Thus, the same flux through a shorter junction translates to a higher magnetic field and a higher Cooper pair momentum p_s. In the regions where only one channel contributes to transport, the slope dI/dV is halved.

If we estimate a realistic device to have a typical junction with $W = 2$ μm, and $L = \xi_0 = \hbar v_F/\Delta_0 \approx 600$ nm [25,102], the magnetic field required to reach Φ_0 is ≈ 1 mT. This field is sufficiently small such that superconductivity is not suppressed and no backscattering is induced or gap is opened in the helical edge channels, thus preserving topological properties of edge channels. [79, 103]

As has been shown, the electrical transport through the TSQUIPT is depends strongly on the flux through the junction. The device can thus be used as a magnetic field sensor. In the following, the device is assumed to be operated via a current bias, to identify the optimum performances. Figure 3.6 shows the potential difference between the probe and the superconductors as a function of flux for several bias currents, as well as the voltage to flux transfer function

$$\mathcal{F} = \frac{\partial V}{\partial \Phi}\ , \tag{3.18}$$

for junctions of different length. The calculated transfer function compares favourably to a state of the art SQUIPT [4], which can reach up to 0.4 mV/Φ_0 or $2\frac{\Delta_0}{e\Phi_0}$, where $\Delta_0 \approx 200$ μeV, is the superconducting gap of aluminium that has been taken as a reference. The transfer functions change sign multiple times, and are damped at higher fluxes, as the current becomes independent from B.

As shown in Fig. 3.6, the voltage drop across the device depends strongly on the magnetic flux for low flux, and tends to a finite value at high flux. As the flux dependence of the TSQUIPT is not periodic, the proposed 2D topological Josephson junction device, can be utilized as a new type of *absolute* magnetometer. That is, by tracing $V(\Phi)$ function, one can determine the absolute flux, and by extension the magnetic field to which the device is exposed. This is in stark contrast with conventional SQUID-based

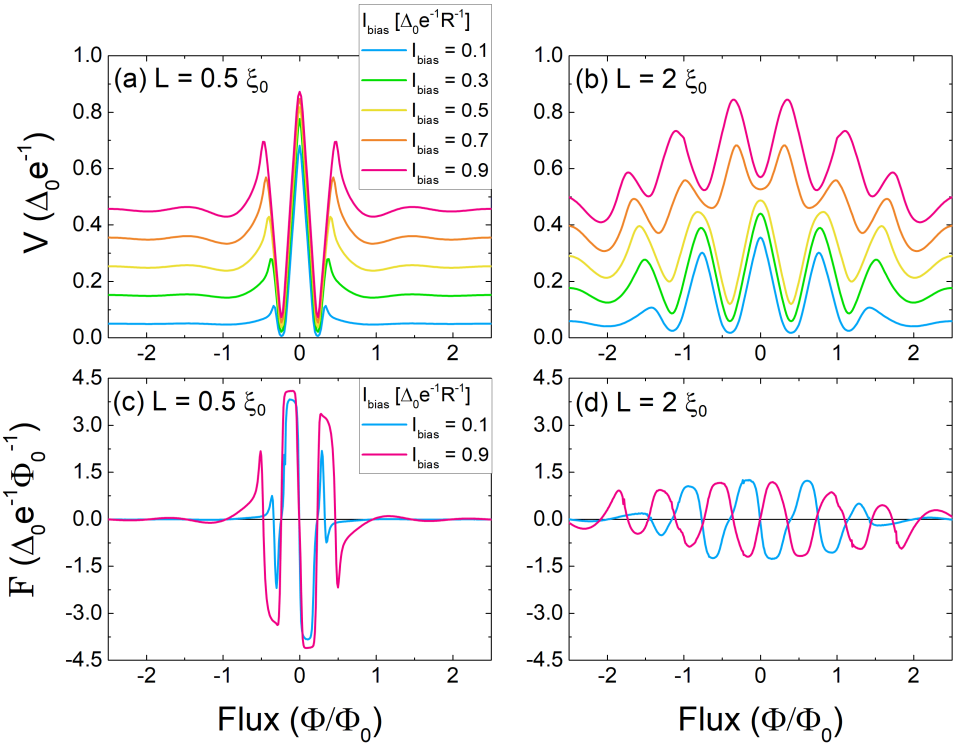

Figure 3.6: (a) and (b) show the voltage drop across the device as a function of the flux for several values of the bias current, for junctions of length $L = 0.5\,\xi_0$ and $L = 2\,\xi_0$ respectively. Figures (c) and (d) show the corresponding transfer function $dV/d\Phi$ for high and low bias currents, for junctions of length $L = 0.5\,\xi_0$ and $L = 2\,\xi_0$ respectively. All curves are calculated for a temperature $T/T_C = 0.1$.

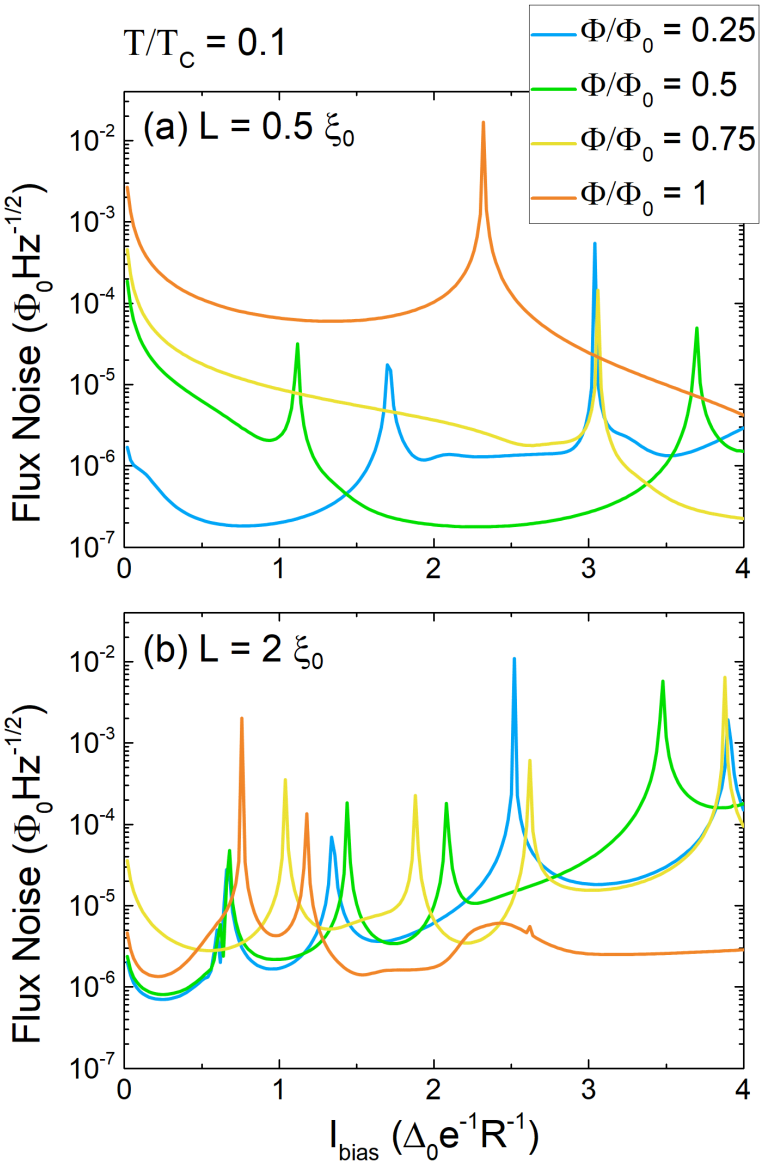

Figure 3.7: The figure shows the flux noise for various fluxes at a temperature of $T/T_C = 0.1$ and as a function of the bias current. (a) For a junction of length $L = 0.5\,\xi_0$ and (b) $L = 2\,\xi_0$.

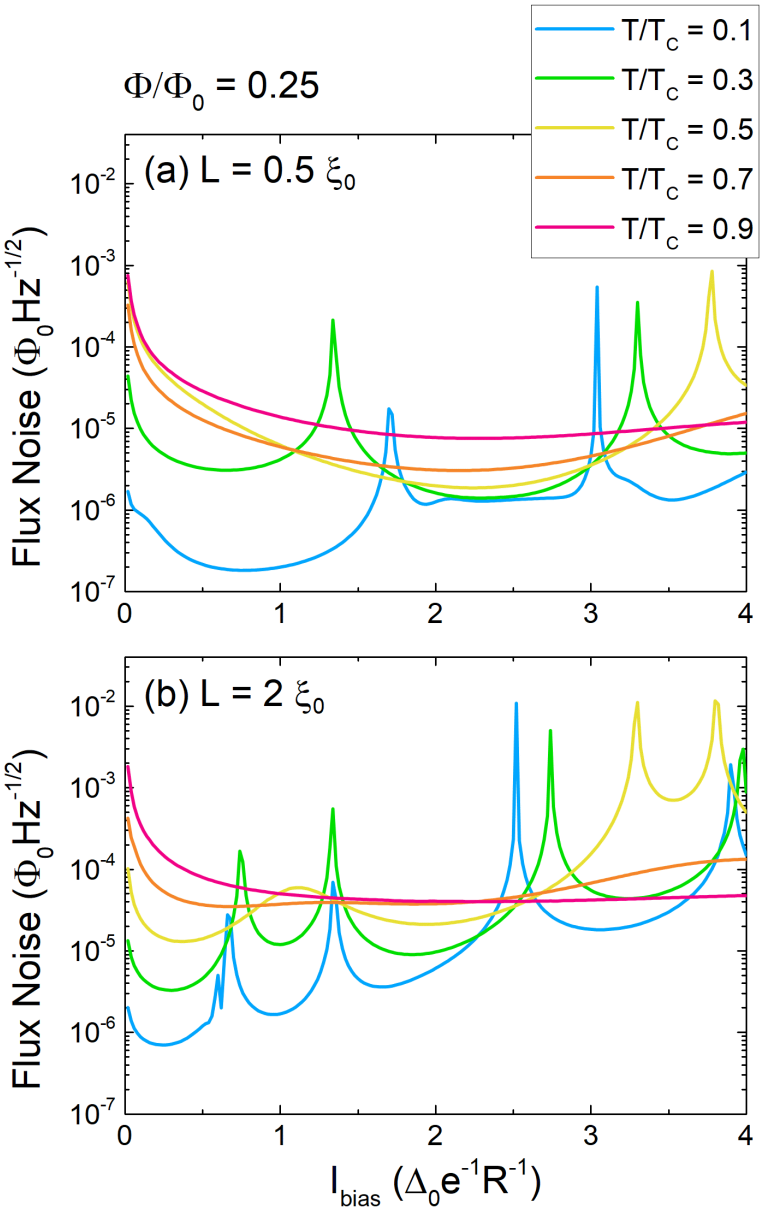

Figure 3.8: The temperature dependence of the flux noise is shown for a flux of $\Phi/\Phi_0 = 0.25$ as a function of the bias current for (a) a junction of length $L = 0.5\,\xi_0$ and (b) $L = 2\,\xi_0$.

magnetometers, which have a $2\,\pi$ periodic flux dependence. To quantify the device's flux sensitivity, we calculate the flux noise given by

$$\phi_{ns} = \frac{\sqrt{S_v}}{|\mathcal{F}(\Phi)]}, \tag{3.19}$$

where $S_v = \frac{\partial V}{\partial I} S_I$ and $S_I = 2eI \coth(\frac{eV}{2k_B T})$ is the tunnelling current noise, and $\mathcal{F}(\Phi)$ is the voltage to flux transfer function. The flux noise is shown in Fig. 3.7 for two junctions of different lengths and for several values of the flux, as a function of the applied bias current. Figure 3.8 shows the temperature dependence of the flux noise. The minimum value of the flux noise is of the order of 10^{-6} $\Phi_0/\mathrm{Hz}^{1/2}$. The curves exhibit large peaks, which are a consequence of the transfer function $\mathcal{F}(\Phi)$ regularly crossing zero. Note that the flux noise $\phi_{ns} \propto \sqrt{R}$, the tunnel junction resistance, which we have taken to be 10 kΩ.

Due to the chaotic nature of the flux noise curves, it is not straightforward to point out an optimum working point, where the sensitivity is high yet the noise is low. On the other hand, the transfer function is not strongly dependent on the bias current, which means that one is more or less free to select a convenient bias. However, as the flux varies, the flux noise can vary greatly. Since the peaks in the flux noise correspond to the transfer function crossing zero, the noise can be limited by working in a range between two crossings. The device with length $l = 2\ \xi_0$ has higher levels of noise, and is more chaotic in general, owning to the increased interference, which in turn leads to more oscillations in the voltage to flux dependence. As the temperature increases, the noise increases, but is smoothed out as well.

3.4 Summary and conclusions

We have proposed a Topological SQUIPT, based on a 2D TI in close proximity to two superconductors, designed to investigate the subtle interplay between superconducting currents that arise in presence of a small magnetic field, and the helical edge states of a 2D TI. A weakly tunnel coupled normal probe allows us to inspect the edge channel density of states which has a non-trivial energy and flux dependence. We conclude that the proposed device can be operated as a type of sensitive, absolute magnetometer, that features several advantages over conventional SQUID and SQUIPT designs.

One advantage of the considered device is that, contrary to conventional SQUID and SQUIPT designs, no ring structure is needed for its implementation, as it arises naturally from the 2D TI. The noise depends strongly on the zeroes in the transfer function, which can be controlled through ϕ_0 via an imposed supercurrent, allowing for an easily optimized performance of the proposed device. The possibility to control the superconducting phase difference via a current bias is another advantage over conventional SQUID

designs. While the behaviour of the flux noise depends on the junction length, width, the applied flux and the temperature in a complicated way, the general rule is that the shorter junction perform better. The performance is ultimately limited by the technical ability to fabricate the junctions, and using state-of-the-art techniques the device has the potential to be extremely small, as the fundamental size limit is determined by the topological edge channel width.

Understanding and verifying the electrical characteristics of this device will reinforce our knowledge of structures based on S-TI interfaces, and pave the way for more complex experiments that aim to exploit quantum interference phenomena present in these hybrid structures.

Chapter 4

Thermal Transport in the TSQUIPT

The contents of this chapter are based on the publication *Phase-Tunable Thermal Rectification in the Topological SQUIPT*.

In this chapter we will investigate thermal properties of the TSQUIPT, which was introduced in the preceding chapters. We find that the heat flow throught he device is strongly dependent on the external magnetic field, and that it can function as a thermal diode.

The chapter is structured as follows. After the introduction, we briefly revisit the model used to describe the density of states in the TSQUIPT and adapt it to describe the thermal conductivity of the device. We then review the thermal response of the TSQUIPT by discussing both the linear and non-linear regime (i.e. for a small and large temperature gradient respectively) and we characterize the device's thermal rectification properties. We show its dependence on various variables such as the length of the junction, the magnetic flux through the junction, the superconducting phase difference, and temperature, for both a probe with a flat density of states (normal metal) and a linear density of states (graphene). In the final section we summarize the results.

4.1 Introduction

As electronic circuits shrink down to the nanoscale, the management of heat becomes evermore important [104–106]. This is especially true for quantum technologies, where fragile quantum states can easily be corrupted through unwanted interactions with a 'hot' environment [107, 108]. Simultaneously, control over heat flows at the nanoscale prompts the attractive prospect of on-chip cooling [109–114] which could make the application of low temperature quantum technologies considerably cheaper, or could be used further improve operating efficiencies.

As a response to recent technological developments, the study of thermal transport in nanostructures has received considerable attention during the past decade. Despite the fact that the flow of heat is not easily controlled, many advances, both theoretical and experimental, have been made, laying the foundation of thermal logic [115–118] and coherent caloritronics [81, 114, 119–122]. Non-linear thermal elements, such as thermal diodes that conduct heat well in one direction but poorly in the reversed direction are particularly valuable for both thermal logic [117] and heat management [123]. Here, a thermal diode that is based on the electronic heat flow in a topological insulator (TI) based Josephson junction (Fig. 7.1), is presented.

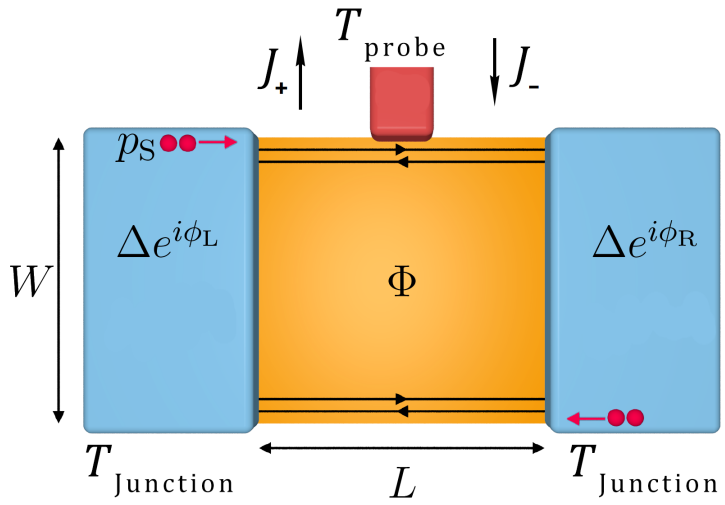

Figure 4.1: The Topological SQUIPT consists of two superconducting leads (blue) connected by a 2D topological insulator (orange) of width W and length L. Transport occurs through the topological edge channels, to which a probe (red) is tunnel coupled. A finite Cooper pair momentum p_S can be induced via a magnetic flux Φ through the junction. Under forward thermal bias, the junction is hot, while the probe is cold, and vice versa under reversed thermal bias, as is indicated by the J_+ and J_- respectively.

Several proposals and realizations of thermal diodes for electronic heat flow exist, based on quantum dots [124–128], superconducting elements [129–133], the quantum Hall effect [134–136], and TI elements [137–140]. TIs have recently received much interest, as they host interesting physics such as spin-momentum locking, helical edge states, and possibly Majorana fermions, which are candidates for quantum computing [5, 6, 8, 9] and have peculiar thermal transport properties [36, 141–143].

The TSQUIPT

Threading a flux through the centre of a TJJ leads to a finite Cooper pair momentum in the superconducting leads, which modifies the Andreev reflection amplitudes in the edge channels of the TI [77]. This momentum shift modifies the spectrum of left- and right-movers in such a way that one can lift the suppressed quasiparticle transport through the edge channels [I], drastically increasing the thermal conductivity of the junction. Exploiting this behaviour, a 2D TJJ can be used as an efficient thermal switch [80, 81]. Note that the effect requires only small magnetic fields, of the order of several mT, which leave the helical edge conductance intact [79].

We will discuss the thermal properties of the TSQUIPT, considering both a probe with a constant density of states (normal metal probe, as in the previous chapter) and a density of states that is linear in energy (e.g. a graphene probe), and find that the device can function as a thermal diode. The diode's rectification properties derive from the fact that the density of states of the topological junction is implicitly dependent on the temperature, via the induced superconducting gap. The properties of the probe, on the other hand, are temperature independent, which leads to an asymmetric response with respect to the temperature gradient.

Due to resonances that appear in the quasi-particle density of states of the junction, the rectification efficiency can be significantly enhanced compared to a conventional NIS junction [129, 130] when using a normal metal probe. As is the case with the electrical properties, the thermal properties of the TSQUIPT depend on the geometry of the junction, the magnetic flux through the junction, and the the superconducting phase difference between the two superconducting leads. As the device is based on a 2D topological insulator, the TSQUIPT could prove useful for heat management, or as part of a cooling scheme in topological insulator based quantum technologies.

4.2 Model

The most important difference with respect to the previous chapter is that now the sub-gap Andreev bound states are omitted as they do not contribute to stationary thermal transport, since these sub-gap particles can only enter the superconducting banks by condensing into a Cooper pair, which carries no heat [144]. As before, the density of states, ρ_{TI} depends on the junction length L, the magnetic flux Φ through the junction, and the superconducting phase difference ϕ_0 between the two superconducting contacts.

For the sake of readability, we briefly revisit the characteristics of the topological junction before moving to the thermal response of the device. In Fig. 4.2 we present the density of states in a density plot as the function of the flux Φ and energy E for the superconducting phase difference $\phi_0 = 0$. In the central, black diamond, the quasi-particle spectrum is gapped, and

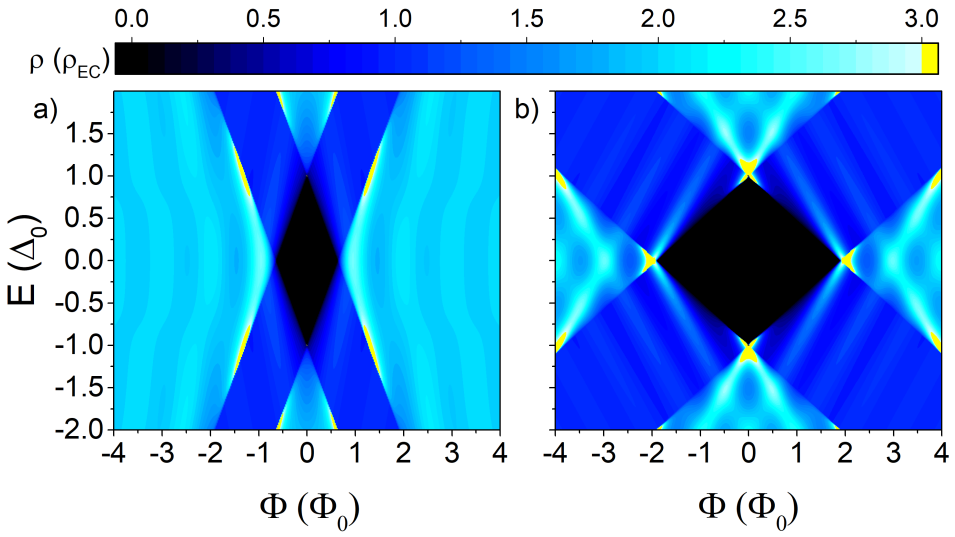

Figure 4.2: a) The density of states in a junction of $L = \xi_0$, in units of the density of states of the unperturbed density of states of the edge channels ρ_{EC}, as a function of energy (normalized by Δ_0) and flux (normalized by Φ_0). b) Density of states for a junction of length $L = 3\,\xi_0$. Note that the sub-gap Andreev bound states are now omitted in both plots, as they do not contribute to stationary thermal transport. In other words, only the quasi-particle excitations are shown.

while electrical transport is possible via Andreev bound states (not shown here), thermal transport is blocked completely. For energies above and below the induced gap Δ_0, quasi-particles can be transmitted through both edge channels (top and bottom regions). The same is true at low energies but at high flux, where heat transport becomes possible because the induced superconducting gap is closed by the Doppler shift (left and right regions). In the diagonal stripes, transport is possible through one mode (i.e. only right-moving, or only left-moving particles), while the other remains gapped, due to an interplay between the quasi-particle energy and the Doppler shift, which is opposite for the two counter-propagating channels. Note that, it is impossible to exploit these branches for unidirectional heat transport in the current scenario, as we do not consider a spin selective probe.

The density of states features modulations that increase in strength for longer junctions. These modulations arise from the merging of Andreev bound states with the continuum and are a consequence of the energy dependent transmission of the electron-like and hole-like states. For the derivation, and a more comprehensive analysis of this effect, see chapter 3.

It is important to note that the edge channel density of states ρ_{TI} is influenced by various parameters. Besides its aforementioned dependence on

energy and flux, it depends implicitly on temperature, via the temperature dependence of the superconducting gap $\Delta = \Delta(T)$ as obtained by the BCS theory, which has been omitted in the formulas to prevent clutter. As we will see, this dependence will be important for the thermal rectification. Furthermore, as can be seen in Eq. 3.16 and is shown in Fig. 4.2, the length of the junction impacts the flux dependence, as it modifies both the slope of the diagonals and the interference pattern. Finally, the superconducting phase difference ϕ_0 influences the position of the interference pattern, and when not equal to 0 or π, breaks the density of states' symmetry with respect to the flux, see again Eq. 3.16.

4.3 Thermal response

We now calculate the fully non-linear thermal tunnel current between the probe and the topological Josephson junction. This is necessary as the Onsager symmetry forbids thermal rectification within the linear response in the presence of time-reversal symmetry. The standard tunnelling expression [101] is used

$$J_{\text{N-TI}} = \frac{1}{e^2 R_T} \int_{-\infty}^{+\infty} E \rho_{\text{TI}}(E) \rho_{\text{P}}(E) [f_{\text{P}}(E) - f_{\text{TI}}(E)] dE. \tag{4.1}$$

For the density of states of the probe $\rho_{\text{P}}(E)$, we consider two different scenarios: a normal metal probe and a graphene probe. For the normal metal probe, the density of states is assumed to be energy independent, $\rho_{\text{P}} = \rho_0$, in which case R_T is the tunnel resistance between the probe and the junction.

For the graphene probe the density of states is energy dependent: $\rho_{\text{P}} = 2|E|/(\pi\hbar^2 v_F^2)$, and R_T represents a resistance factor associated with the transmission between the probe and the junction. The density of states in the junction, $\rho_{\text{TI}}(E)$, is given by Eq. 3.14. The Fermi functions $f_{\text{P}}(E)$ and $f_{\text{TI}}(E)$ are associated with the probe and the junction respectively, with $f_{\text{P,TI}}(E) = (1 + e^{E/k_B T_{\text{P,TI}}})^{-1}$.

We only consider a thermal bias, and thus take the chemical potential to be zero everywhere. To ascertain that the topological insulator remains in thermal equilibrium with the superconducting leads, and the tunnelling approximation is valid, it is necessary that $R_T \gg R_K$, with $R_K = h/e^2$ the von Klitzing resistance. Only when the thermal conductance between the probe and the junction is much smaller than the thermal conductance between the topological edge channels and the superconducting leads, one can safely assume thermal equilibrium in the topological junction.

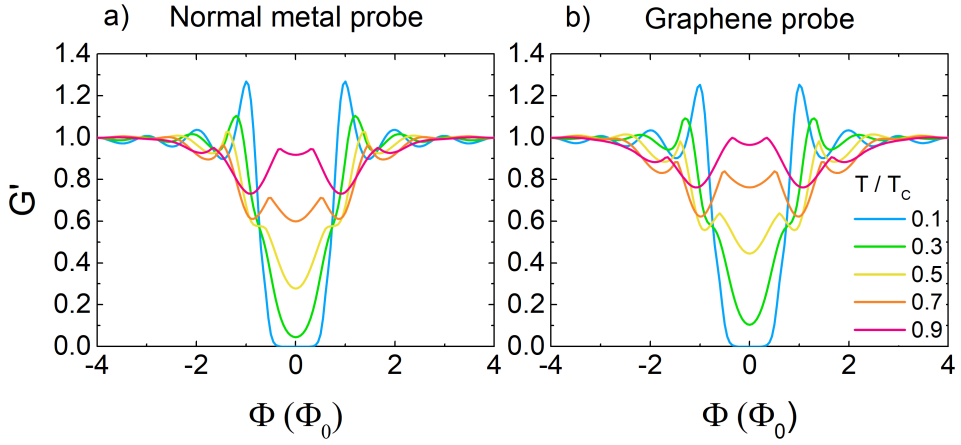

Figure 4.3: The normalized thermal conductance $G'(\Phi) = G(\Phi)/G_\infty$ where $G_\infty = G(\Phi \to \infty)$ as a function of the magnetic flux through the junction at various temperatures. a) Conductance for a probe with a flat density of states, i.e. a normal metal and b) conductance for a probe with a linear density of states, i.e. a graphene probe. In both cases the junction length is $L = \xi_0$ and superconducting phase difference is taken to be fixed at $\phi_0 = 0$.

Linear regime

Assuming the device is operated in the linear regime, i.e. the thermal gradient is small with respect to the base temperature T:

$$\delta T = |T_{\mathrm{TI}} - T_{\mathrm{P}}| \ll T = \frac{1}{2}(T_{\mathrm{TI}} + T_{\mathrm{P}}), \tag{4.2}$$

we can approximate the thermal current as:

$$J_T = G_T(\Phi)\delta T, \tag{4.3}$$

where

$$G_T(\Phi) = \frac{1}{4e^2 R_T}\int_{-\infty}^{+\infty} \frac{E^2}{k_B T^2}\frac{\rho_{\mathrm{TI}}(E)\rho_{\mathrm{P}}(E)}{\cosh^2\frac{E}{2k_{\mathrm{B}}T}}\, dE. \tag{4.4}$$

The thermal conductance G_T, like the thermal current, directly reflects the matching between the density of states of the probe and the topological junction. It depends on T, the length of the junction L, the flux through the junction Φ, and the superconducting phase bias ϕ_0, as follows from Eqs. 3.14, 3.15, and 3.16.

Fig. 4.3 shows the thermal conductance of the TSQUIPT as a function of the flux through the junction normalized by the conductance at high flux, $G'(\Phi) = G(\Phi)/G_\infty$ where $G_\infty = G(\Phi \to \infty)$, which is twice the quantum of thermal conductance $G_Q = \pi^2 k_B^2 T/(3h)$.

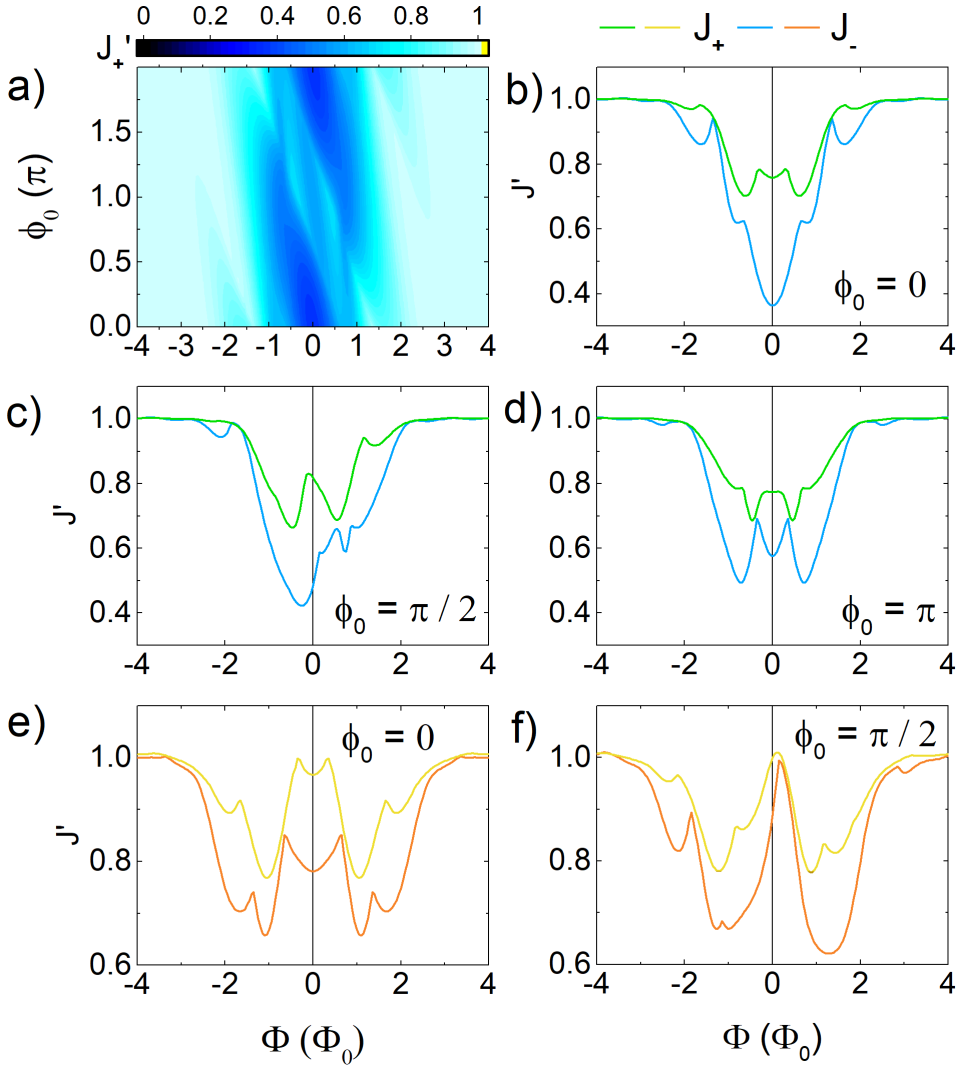

Figure 4.4: a) The normalized forward heat current $J'_+(\Phi) = J_+(\Phi)/J_\infty$ with $J_\infty = J(\Phi \to \infty)$, with $T_{\rm TI} = T_{\rm Hot} = 0.9\,T_{\rm C}$ and $T_{\rm P} = T_{\rm Cold} = 0.1\,T_{\rm C}$. Junction length $L = \xi_0$, the heat current is plotted as a function of the flux through the junction (normalized by Φ_0) and the superconducting phase difference ϕ_0 in the middle of the junction. b) The normalized forward heat current J'_+, and reversed heat current J'_- as a function of the normalized flux for a junction of $L = \xi_0$, with $T_{\rm Hot} = 0.9\ T_{\rm C}$ and $T_{\rm Cold} = 0.1\ T_{\rm C}$, and superconducting phase difference $\phi_0 = 0$ c) $\phi_0 = \pi/2$ and d) $\phi_0 = \pi$. e) and f) show the normalized heat current for a graphene probe, at $\phi_0 = 0$ and $\phi_0 = \pi/2$ respectively, for the same parameters as previously.

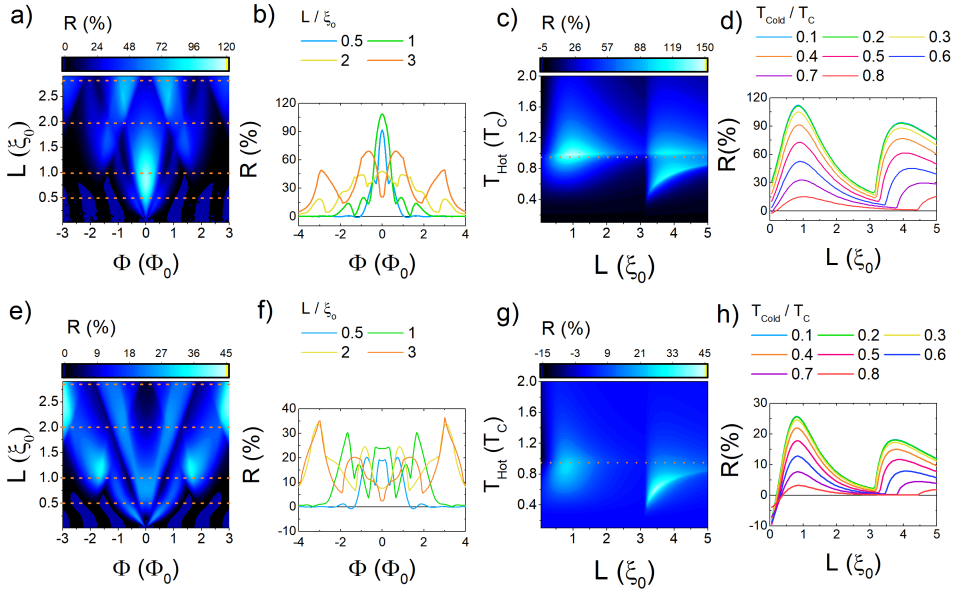

Figure 4.5: a) - d) correspond to a normal metal probe. a) A density plot of the rectification coefficient as defined in eq. 4.5, as a function of the normalized flux and the junction length, $T_{\mathrm{Hot}} = 0.9\,T_{\mathrm{C}}$ and $T_{\mathrm{Cold}} = 0.1\,T_{\mathrm{C}}$. b) $\mathcal{R}$ versus flux for junctions of four different lengths, other parameters like a). The position of the cuts is indicated by the orange dotted lines and arrows in a). c) A density plot of the rectification coefficient as a function of the length of the junction and the T_{Hot}. $T_{\mathrm{Cold}} = 0.1\,T_{\mathrm{C}}$, $\Phi = \phi_0 = 0$ d) $\mathcal{R}$ versus flux for various values of T_{Cold}, $T_{\mathrm{Hot}} = 0.9\,T_{\mathrm{C}}$, and $\Phi = \phi_0 = 0$. The position of the light blue line ($T_{\mathrm{Cold}} = 0.1\,T_{\mathrm{C}}$) is indicated by the dotted orange line in c). e) - h) Like a) - d), but with a graphene probe.

At low temperatures, the heat flow through the device is completely suppressed by the presence of the superconducting gap. However, by applying a flux one can close the quasi-particle gap, allowing heat transport to occur. For temperatures closer to T_C, the size of the gap, and thus the suppression of the conductance decreases, however a modulation is clearly visible up to 0.9 T_C. For magnetic fluxes larger than a few flux quanta, the conductance reaches a constant value and the modulation decays to zero. While the thermal conductance for both probes looks very similar, it is worthwhile to note that the thermal conductance increases linearly with temperature for a normal probe, but super-linear for a graphene probe (not shown here).

Non-linear regime

To obtain the rectifying properties of the device, it is necessary to calculate the heat currents for an arbitrary temperature gradient, using Eq 4.1. To

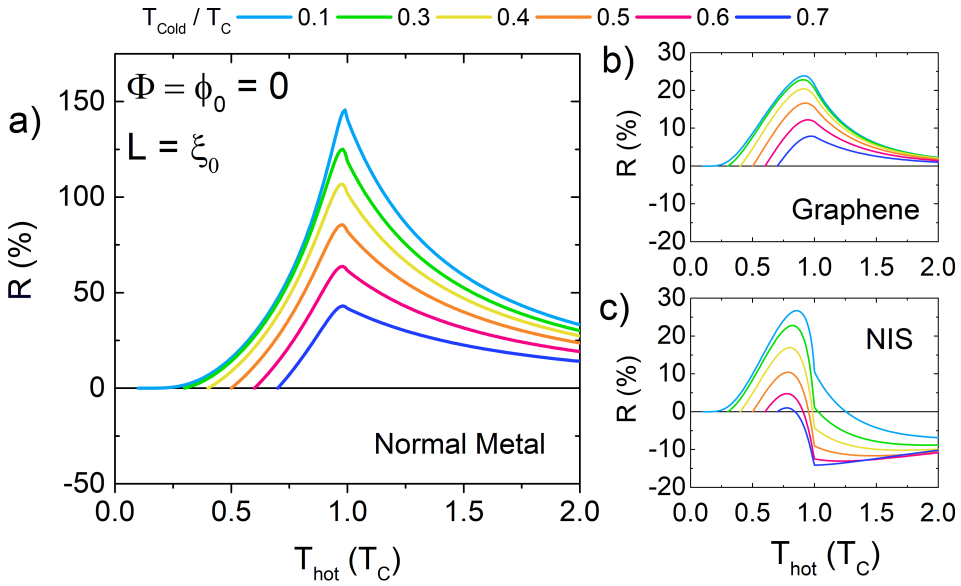

Figure 4.6: a) The rectification coefficient $\mathcal{R}$, as defined in Eq. 4.5, for a normal metal probe, as a function of $T_{\rm Hot}$, for various values of $T_{\rm Cold}$. Junction parameters: $L = \xi_0$, and $\Phi = \phi_0 = 0$. b) The rectification coefficient for a graphene probe. c) The thermal rectification of a NIS junction is shown for comparison.

quantify the temperature gradient, we introduce T_{Hot} and T_{Cold}. Furthermore, we denote the heat current in the forward direction $J_+ = J(T_{\mathrm{TI}} = T_{\mathrm{Hot}}, T_{\mathrm{P}} = T_{\mathrm{Cold}})$, and the reversed configuration, where the temperatures are opposite, as $J_- = J(T_{\mathrm{TI}} = T_{\mathrm{Cold}}, T_{\mathrm{P}} = T_{\mathrm{Hot}})$. This notation will be convenient when we discuss thermal rectification.

In Fig. 4.4 a) we show the normalized thermal currents $J'(\Phi) = J(\Phi)/J_\infty$ with $J_\infty = J(\Phi \to \infty) = 2\pi^2 k_B^2 T^2/(3h)$ in the forward configuration (hot junction, cold probe) as a function of the flux Φ and superconducting phase bias ϕ_0, for a normal metal probe. When $\phi_0 \neq 0, \pi$, an asymmetry in the flux dependence of the heat current is present. In Fig. 4.4 b) - d), we present the normalized forward (green line) and reversed (blue line) heat currents, for various values of the superconducting phase difference ϕ_0 and a normal metal probe, as a function of the flux. When a large magnetic flux is applied, heat transport is fully enabled by the Doppler effect. As the impact of the gap diminishes, so does the difference between the forward and reversed heat currents. Fig. 4.4 e) and f) show J'_+ and J'_- for the case of a graphene probe. The qualitative behaviour of the graphene probe device is similar to the normal probe device, as the dependence on flux and phase mainly originates from the junction, and not from the nature of the probe.

The difference between the forward and reversed heat current, and thus the diode's rectification properties, stem from the fact that the density of states in the probe is temperature independent, while that of the junction is modulated by temperature via the dependence of the induced superconducting gap. This results in an asymmetry in forward and reversed heat flow, which can be understood from Eq. 4.1. In the absence of the temperature dependence in $\rho_{\mathrm{TI}}(E)$, the interchange of temperatures affects only the Fermi functions, leading solely to a change of sign of the thermal current. The temperature dependence of the gap is thus fundamental for the asymmetric thermal response which will be discussed in detail later.

If the junction heats up to temperatures approaching the critical temperature T_C, the magnitude of the induced gap decreases rapidly. This allows for an increased heat flow from the junction to the probe. Conversely, if the probe is hot, but the junction is cold, the presence of the gap prevents heat flow for temperatures up to $T \approx T_C$. As the density of states of the graphene probe is linear in energy, it gives a greater weight to states that are higher in energy when calculating the tunnel current, and the discrepancy between the forward and reversed heat current is reduced.

Thermal rectification

To quantify the effectiveness of the thermal rectification, we define the relative rectification coefficient

$$\mathcal{R}(T_{\mathrm{Hot}}, T_{\mathrm{Cold}}) = 100 \cdot \frac{|J_+| - |J_-|}{|J_-|}, \tag{4.5}$$

where J_+ denotes the forward heat current, corresponding to a hot junction and a cold probe, and J_- is the reversed current, where the temperatures are transposed.

As the resonances in the junction influence the density of states above the gap and by extension the heat transport, the length of the junction and the flux through the junction have a strong effect on the thermal properties. In Fig. 4.5 a we show the dependence of the rectification coefficient on the length of the junction and the flux through the junction for the normal probe. Panel b shows the rectification coefficient for four different lengths, corresponding to cuts of panel a. For the shorter junctions, the rectification has a sharp peak around zero flux, while for the longer junctions, the rectification at zero flux becomes a local minimum, although it partly recovers at finite values of the flux.

Fig. 4.5 c is a density plot of the rectification as a function of the junction length and T_{Hot}, while $T_{\mathrm{Cold}} = 0.1\,T_{\mathrm{C}}$ is kept constant. There are two notable features: firstly, it is clear that for maximum rectification, T_{Hot} should be close to T_{C}, independent of the length. Secondly, as can also be seen in panel d, the rectification peaks at $L = \xi_0$, and then diminishes until $L \approx 3\,\xi_0$, after which it largely recovers before decaying again. This oscillation of the rectification with respect to the junction length is a consequence of the position of the maxima in the density of states of the junction, that arise from quantum-mechanical interference.

Fig. 4.5 e - h show the behaviour of the rectification with a graphene probe. Contrary to before, the maximum of $\mathcal{R}$ now moves outwards to higher values of the Φ as the length of the junction increases. However, the value of the maximum stays between $\approx 25\%$ and ≈ 40 %, depending on the various parameters. Furthermore, for a graphene probe connected to very short junctions, the rectification coefficient will be negative, especially when T_{Cold} is low, which indicates a reversal of the device's expected response. This behaviour is similar to that of a NIS junction (cf. Fig. 4.6 c), however the effect is enhanced as the graphene density of states gives a greater weight to high energy states.

The maximum rectification coefficient is obtained using a normal metal probe. Following the discussion of Fig. 4.5, we find that maximum value of the rectification coefficient $\mathcal{R} \approx 145\%$ is found for a junction of length ξ_0, with $T_{\mathrm{Cold}} \to 0$ and $T_{\mathrm{Hot}} \to T_{\mathrm{C}}$, $\Phi = 0$ and $\phi_0 = 0$. At a length of $3\,\xi_0$ and $\Phi = 0$, the efficiency has only a value of $\mathcal{R} \approx 45\%$, although it recovers to $\mathcal{R} \approx 70\%$ at $|\Phi| \approx 0.7\,\Phi_0$. When considering a graphene probe, the optimum quantity of flux increases with the device length, although the maximum value never exceeds $\mathcal{R} \approx 40\%$.

Fig. 4.6 shows the rectification coefficient as a function of T_{Hot}, for various values of T_{Cold}, for a junction of $L = \xi_0$. At this length, the rectification is maximum for $\Phi = \phi_0 = 0$, but this is not necessarily true for junctions of a different length. The rectification peaks just below T_C, and decreases in a

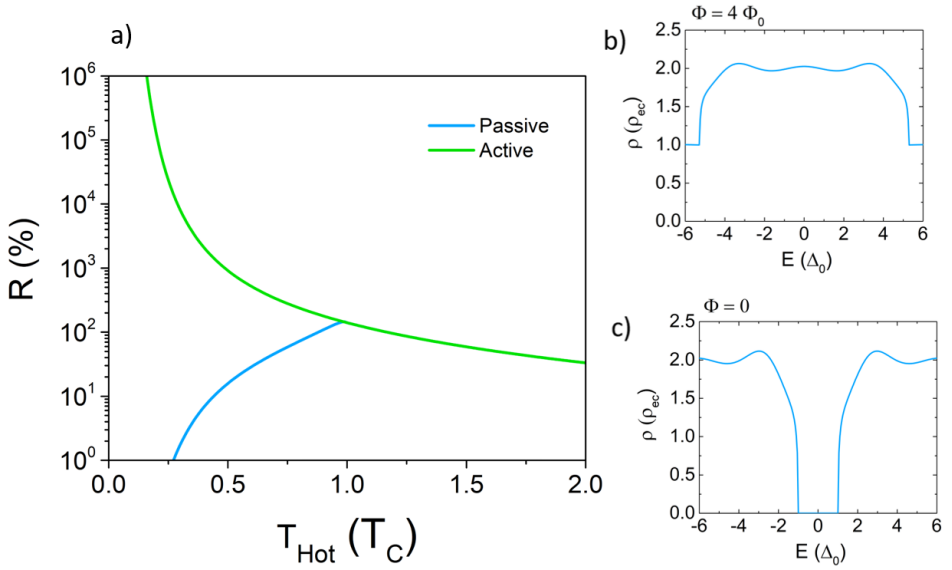

Figure 4.7: a) The rectification coefficient of the diode for $T_{\mathrm{Cold}} = 0.1\,T_{\mathrm{C}}$, a junction of length $L = \xi_0$, and $\Phi = \phi_0 = 0$ (passive mode, identical to the blue line in fig. 4.6) versus the rectification coefficient when the diode is open in the forward configuration at $\Phi = 4\,\Phi_0$, but closed in reversed configuration with $\Phi = 0$ (active mode). b) The density of states of the junction at $T = 0.1\,T_{\mathrm{C}}$, $L = \xi_0$ and $\Phi = 4\Phi_0$. In this case the quasiparticles can flow freely from the junction into the normal metal probe. c) The same as b) except now $\Phi = 0$. The induced gap suppresses the heat flow from the probe to the junction.

constant fashion as T_{Cold} increases, which demonstrates that the maximum rectification factor is obtained with T_{Cold} at the lowest possible temperature. When using a graphene probe (Fig. 4.6 b), the rectification coefficient is reduced, with a maximum value and shape that is reminiscent of the NIS diode. However, the temperature range of positive rectification is increased with respect to that of the NIS junction, especially for temperatures above the critical temperature. The graphene probe, which reduces the effect of the junction density of states, can thus be seen as an intermediate between the NIS junction and the TSQUIPT with normal metal probe in terms of thermal rectification performance.

To further increase the rectification coefficient, one could consider replacing the normal metal tunnel coupled probe with a superconducting probe, in this case, an enhancement similar to the one present in [130] can be expected, although the extra Josephson coupling should also be taken into account.

Alternatively, one could think to exploit the switching effect of the junction where the quasi–particle gap can be closed by applying a magnetic

flux [80]. Closing the quasi-particle gap enhances the thermal response of the junction. Hence, when closing the gap by applying a large flux in the forward configuration (hot junction, cold probe), the quasi-particle current and thus the heat flow through the device is increased, see the density of states presented in Fig. 4.7 b). On the other hand, keeping the gap open i.e. not applying a magnetic flux, in the reversed configuration (cold junction, hot probe) ensures a minimal back flow, see the density of states shown in Fig. 4.7 c. Thus, by using the device dependence on the magnetic flux, one can implement an active rectification scheme. Since the heat flow is exponentially suppressed with the channels closed and $k_B T \ll \Delta_0$, rectification is strongly enhanced below T_{C}, as shown in Fig. 4.7 a.

4.4 Summary and conclusion

We have shown that the Topological SQUIPT can be utilized as a thermal diode, and how the rectification efficiency depends on various device parameters such as the length L, the magnetic flux through the topological Josephson junction Φ and the phase difference between the superconducting leads ϕ_0, for a probe with a flat and a density of states or one that is linear in energy. A passive rectification coefficient of up to $\approx 145\%$ is reached under optimal conditions, when using a normal metal probe, which is high with respect to comparable designs such as NIS or SIS' junctions. An interesting property of the TSQUIPT is that it offers control over the superconducting gap via a small external magnetic field, which can be used to open the junction to heat flow when needed. Exploiting this effect in an active rectification scheme, the rectification can be strongly enhanced for temperatures below T_C. The proposed device is a might be used to manage heat flows in temperature sensitive 2D topological insulator based quantum technologies.

Chapter 5

Gate-controlled Superconductivity

In the first part of this chapter, a historic overview of the study and understanding of the effect of an electric field on metallic superconductors is given. In the section thereafter, a comprehensive overview of the recently discovered ability to gate superconducting nano devices and its features, is presented. Possible explanations of the effect will discussed at the end of this chapter, as well as in the following chapters.

5.1 Historical overview

In 2018, De Simoni *et al.* published an article showing the suppression of the supercurrent flowing through superconducting titanium, and aluminium nanowires in response to electrostatic gating. [145] Their results were surprising, as it was generally believed that electrostatic fields decay rapidly inside superconductors, similarly to how electrostatic fields are screened over short distances in normal metals.

In 1935, the London brothers employed Maxwell's equations to derive that static electric and magnetic fields are screened over the London penetration length λ_L. [146]. After an unsuccessful attempt to measure a change in capacitance during the superconducting to normal transition [147], and further theoretical considerations [148], they abandoned this idea, concluding instead that electric fields are screened in superconductors over distances similar to those in normal metals. [149]

Also when considering the equation of motion of the superconducting condensate, the case seems hopeless. From the London equation, Maxwell's equations and the the superconducting current, the equation of motion of the superconducting condensate can be derived

$$\frac{\partial \mathbf{p}_s}{\partial t} = eE + \nabla\mu, \tag{5.1}$$

where $\mathbf{p}_s = \nabla/2\phi - e/c\mathbf{A}$ is the condensate momentum and the gauge invariant potential can be expressed as $\mu = (1/2)(\partial\phi/\partial t) + e\Phi$, where ϕ is the the phase of the order parameter and Φ is the electric potential. Equation 5.1 defines the electric field E in terms of the gauge invariant quantities μ and $\mathbf{p}_s$. Substituting μ and ϕ into 5.1, we are left with a definition of E in terms of the potentials $\mathbf{A}$ and Φ.

If the second term on the right hand side of 5.1 is neglected, the presence of an electric field appears to result in a continues acceleration of the condensate. This unrealistic result leads to the conclusion that an electric field can only exist close to the boundary of the superconductor.

After the experiment by the London brothers, work on this topic is sparse. While the arrival of the BCS theory of superconductivity [150] in 1957 was a great leap forward in the microscopic understanding of the phenomenon, it made no statement on the matter of electric field penetration. In 1970 and 1971, Landau [151] and Pippard [152] touch upon the electric field penetration indirectly [153], by studying the resistance of Superconducting - Normal interfaces in superconductors driven into the intermediate state by a magnetic field. They find that in the intermediate state, the resistance is larger than the summed resistance of the normal parts. Interestingly, the excess resistivity tends to zero at low temperatures and increases at higher temperatures. From their results it is later concluded that the electric field penetration length l_E is proportional to the charge imbalance relaxation time. [153] Importantly, this length can be much larger than the typical length scales i.e. the London penetration depth λ_L and the superconducting coherence length $\xi(T)$, although only the longitudinal part of E, that does not give rise to a magnetic field, penetrates the superconductor.

The penetration of electric fields into a superconductor has also been analysed in the framework of the time dependent Ginzburg-Landau equations [153–155][1], which generalize Ginzburg-Landau theory to include relaxation processes. Unfortunately, the application of this theory is very limited, as it is valid only close to the critical temperature, and when deviations from equilibrium are small. These conditions are generally only fulfilled by so-called gapless superconductivity, where the gap in the energy spectrum disappears, but the order parameter retains phase coherence and can support a finite supercurrent. In this case, the electric field decays over a length in which the magnitude of the order parameter varies from its bulk value.

For an ordinary gapped superconductor, the penetration length of the electric field can be derived starting from the kinetic equation of the quasiparticle distribution function, assuming that the spatial variation of this distribution is smooth compared to $\xi(T)$, the characteristic quasiparticle

[1]Note that some of the cited works concern high temperature superconductors, which are quite distinct from the elementary BCS superconductors that are the focus of this thesis.

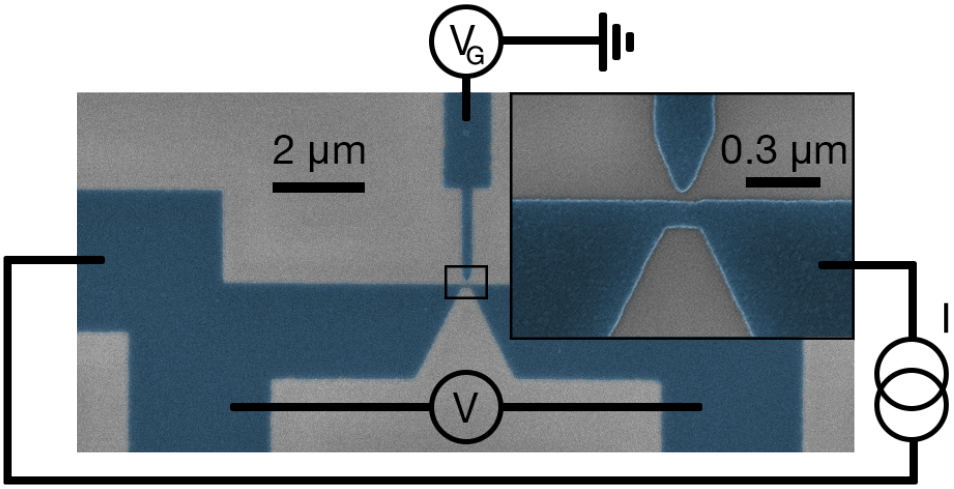

Figure 5.1: False colour SEM image of a typical Dayem bridge device with a side gate. Inset: close up of the region indicated by the black square showing the Dayem bridge and gate electrode. The bridge is approximately 120 nm wide, 100 nm long and the gate-bridge separation is around 30 nm. The leads on either side of the bridge are 2 µm wide.

energy is not large compared to the gap and temperature and the impurity concentration is fairly small. [153] The penetration is intimately linked to quasiparticle branch imbalance [155], and one finds $l_E = \sqrt{D\tau_Q}$, where D is the diffusion coefficient and τ_Q is the branch imbalance relaxation time. This length exceeds the energy relaxation length, which in turn may be significantly larger than $\xi(T)$ and λ_L. This result explains the continues change in resistivity of a superconductor in the intermediate state. [153]

Examinations into phenomena related to the behaviour of electric fields in superconductors remained few and far between, also hereafter. Although recently, some interesting hints regarding such effects as ferro-electricity in superconducting clusters in a molecular beam [156], and electric field induced clumping of elementary superconductors [157] have been found. The last experiment was notably inspired by similar works on high temperature superconductors, which feature a much lower carrier concentration than metals, and can therefore be modulated via gating. [158–160]

As an electric field is generally not expected to significantly influence superconductivity, the recent demonstration of an electrostatic field suppressing the supercurrent in thin film wires made of titanium [145], came as a great surprise. In 900 nm to 3 µm long, 200 nm wide and 30 nm thick titanium wires, the supercurrent was suppressed via side gates, up to a complete suppression around $V_{\mathrm{Gate}} \approx 45$ V. A similar effect was demonstrated in aluminium [145] and later also in Dayem bridges [161] (see Fig. 5.1) made of titanium [162, 163], aluminium [III], niobium [164], vanadium [165], and in

aluminium–copper–aluminium Josephson junctions [166]. Moreover, recent experiments have probed the effect of electrostatic gating on the SC-phase in a SQUID [167], on the nature of the switching current distributions in gated titanium Dayem bridges [168], and on suspended Ti nanowires. [169]

In reaction to the result above, similar experiments have been undertaken other groups. Ritter *et al.* proposed a fast cryogenic switch based on gated titanium nitrate nanowires [170]. Alegria *et al.* performed tunnel spectroscopy measurements of the density of states of while gating a titanium nanowire [171], while Golokolenov *et al.* performed radiofrequency measurements on a vanadium device. Notably, all three papers ascribe the effects to quasi-particle injection caused heating as a result of Fowler-Nordheim electron emission [172] from the gate, see also Sec. 5.4 where this interpretation will be discussed in more detail.

Gates suppressing a supercurrent is thus quite general, as it has been demonstrated in multiple BCS superconductors, as well as in weak links such as constriction or Superconductor-Normal-Superconductor junctions. Furthermore it has been found in devices fabricated on SiO_2 and sapphire substrates, as well as in suspended wires, and using both planar side gates and backgates. However, the exact mechanism behind the effect is yet controversial. A careful re-evaluation of the screening effect in BCS superconductors has again found that the screening length is roughly unchanged from that in the normal metal. [173] A microscopic model that has been recently proposed, and other interpretations, will be discussed later. First, an overview of the field effect phenomenology is presented.

5.2 Gate-controlled Superconductivity Characteristics

The effect is typically measured in a four wire configuration, see Fig. 5.1 and Sec. A.4. A thin superconducting film is deposited to create a device that features a narrow wire or constriction. The device is then current biased, and the voltage drop across the device is measured while sweeping the current at various gate voltage values. It is found that the gate voltage V_{Gate}, reduces the critical current I_C, at which the device switches from the normal to the superconducting state. A typical device employs sidegates. Although backgates have also been used, they tend to be less effective. [163] The first experiments utilized narrow wires, with a width of ≈ 200 nm, but it seems that the side-gate supercurrent suppression is stronger in nanoconstrictions [162, 163], often referred to as Dayem bridges [161].

The gate-superconductor separation is very small, typically ranging between 50 and 150 nm, see again Fig. 5.1 for a typical device. Depending on the device dimensions and the material, the critical voltage needed to suppress the supercurrent typically varies between 5 and 80 V. Dividing 50

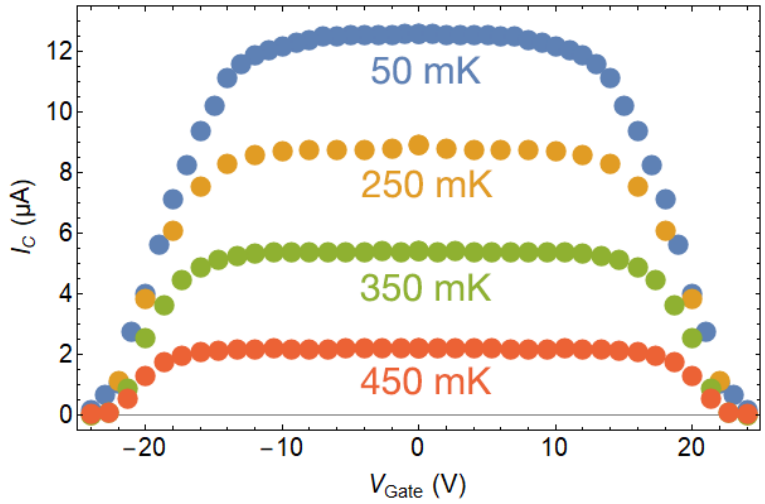

Figure 5.2: Typical dependence of I_C on the gate voltage V_{Gate} at four different temperatures.

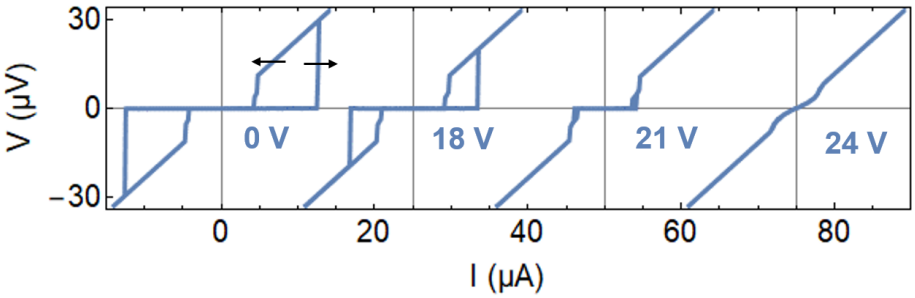

Figure 5.3: The voltage drop across the bridge versus bias current, for four values of V_{Gate} at 50 mK. Arrows indicate sweep direction, and the curves are horizontally offset for clarity. At first only I_C is reduced, while I_R remains unchanged. As the value of I_C approaches that of I_R, also the latter becomes reduced. Finally, when $I_C = 0$, some non-linearity lingers, before the resistance becomes fully ohmic.

V by 50 nm we can estimate the electric field reaches intensities of the order of $E \approx 10^9$ V/m. The electric field does not affect the metal's normal state resistance, which is expected given their very high electron density.

The typical electric field response is shown in Fig. 5.2. Up to a certain value of V_{Gate} there is little to no effect on I_C. Above this value however, I_C rapidly diminishes, until it is zero. At higher temperatures, the region where the gate has negligible effect widens, yet the critical gate value V_{Gate}^C, where $I_C = 0$ remains the same. In some cases, shoulder like features are present. [145, 163, 168, 169] Notably, the effect is symmetric in V_{Gate}, which excludes carrier density manipulation or surface charge as a direct cause, as this would manifest as asymmetric in V_{Gate}. Even when I_C is affected, the retrapping current I_R remains unchanged until I_C and I_R coincide, see also Fig. 5.3.

Gate-controlled superconductivity experiments have been performed on standard, undoped 300 nm SiO_2 and on sapphire substrates, as well as on suspended wires. Qualitatively, the behaviour is the same on all substrates, and variations can be attributed to differences between devices such as the material, device dimensions and gate distance. For the devices described in this thesis, the leakage current between the gate and device typically reaches up to $\sim 10^{-11}$ A at full suppression, which typically occurs between 20 and 50 V, on both substrates. A significant part of this current can be attributed to leakage in the cabling of the cryostat. Furthermore, values as low as $\sim 5 * 10^{-14}$ A have been reported for full suppression at ~ 60 V for titanium devices on sapphire substrate [145, 163].

Spatial extension

Two important length scales in BCS superconductors are the London penetration depth λ_L, indicating the length over which a magnetic field can penetrate the material, and the superconducting coherence length at zero temperature ξ_0. For the titanium wires, it was estimated that $\lambda_L \approx 900$ nm, and $\xi_0 \approx 100$ nm. Measurements on a device with multiple connections at various distances from a side gate, seems to indicate that the strength of the suppression decays exponentially with an attenuation length of ≈ 770 nm. [145, 174] Notably, this value is several times larger than the coherence length, and of the same order of magnitude as λ_L. The spatial extension seems to be largely unaffected by the temperature, until close to T_C, where it decreases.

The effect has also been investigated in superconducting regions with lateral dimensions larger than λ_L i.e. in a titanium 30 nm thick, 4 μm wide and 4 μm long region. [174] By employing a backgate, the supercurrent through this region was successfully diminished in the usual fashion. The effect was weaker however (i.e. high gate voltages were required), possibly due to the relatively large backgate - superconductor spacing of 300 nm.

This result suggests that mainly the dimension of the superconductor in the direction parallel to the electric field is important.

Another clue about the spatial extension of the effect is given by measurements on a titanium nano-constriction with two gates, one on either side. [163,174] A 30 nm thick and 4 μm wide titanium film is interrupted by a constriction that is ≈ 125 nm long and ≈ 300 nm wide. Side gates are placed next to this constriction at a distance of 80 - 120 nm. The supercurrent can be completely suppressed in the usual fashion, by using either of the gates alone. Interestingly, it is found that the effect of the two gates is independent of each other, i.e. applying any voltage smaller than the critical gate voltage, where the supercurrent is completely suppressed, with one gate, does not enhance or otherwise affect the effect of the other gate.

In another work, the switching of a long wire divided into multiple segments has also been reported. [170] The non-local measurements showed two regimes, depending on whether or not the source drain current exceeded the retrapping current. In this case, the entire wire switched to normal at once. Otherwise, a sequential switches was observed. These dynamics can likely be attributed to Joule heating.

Josephson effect

The behaviour of the Josephson effect as a function of gating also provides useful information. Using equations that describes the critical current of a Josephson constriction in the short junction limit, experimental data has been fitted. [163,174] The authors show that the temperature dependence of I_C was well described by the typical Kulik-Omelyanchuck relation for clean ballistic constrictions. While gating however, the critical current behaviour is better described by the Ambegaokar-Baratoff model, which is applicable when the transmission probability becomes low.

From this observation, the authors conclude that the effective transmission probability of the constriction drops rapidly when approaching the critical gate voltage. While there is good agreement between the model and the experimental results, the model is empirical and thus it offers no further insight with respect to how the electric fields effects the transmission probability of the junction.

SQUID

Experiments have also been performed on a SQUID constructed by creating two 150 nm long and wide constrictions, each with a side gate, in a ring made of thin film titanium. The two constrictions are placed 8 μm apart, enabling the independent control of the critical current of the constrictions. [167,174] Like before, the effect is not dependent on the sign of the gate voltage. Notably, the electric field applied to either constriction affects the whole

interference pattern, suggesting that the electric field somehow couples to the superconducting phase. Gating the constrictions has a clear effect, both reducing the critical current of the device, as well as shifting the interference pattern along the magnetic flux axis. These effects can be described by the standard RCSJ (Resistively and Capacitively Shunted Junction) model.

Interestingly, the distribution of the switching current was found to be significantly more spread in one branch than in the other. [167] Something that cannot be explained by conventional SQUID models. Furthermore, it seems that these fluctuations are induced even at low gate voltages, before the critical current is reduced. Another interesting observation, is that phase coherence is seemingly maintained, even when the critical current of one of the junctions is completely suppressed. These observations suggest again that the electric field effect somehow influences, or acts through, the phase of the superconducting condensate.

Switching distributions

To investigate possible phase fluctuations induced in the superconductor by the electric field, switching current distributions were measured in 30 nm thick, 150 nm long and 120 nm wide titanium constrictions. [168] The current voltage characteristics were measured by the usual four wire technique, and the device was described using the RCSJ model. In the RCSJ model, the transition from the superconducting to the normal state is described as a 'phase particle' escaping form a potential minimum, which corresponds to a 2π rotation in the superconducting phase ϕ.

It was found that, when comparing the suppression of the critical current by temperature and by gate voltage, the switching current distributions were much wider in the latter case. The authors speculate that the electric field increases the probability of switching by affecting the superconducting phase in such a manner that phase fluctuations are enhanced. Also noteworthy is that the gating induced broadening tends towards the thermally induced broadening at higher temperatures i.e. they become narrower. This is perhaps related to the reduced effectiveness of the gating at higher temperatures, although the supercurrent can still be reduced to zero also at these temperatures. A narrower distribution might also be more appealing when considering the effect for practical applications.

Density of states

To date, only one experiment on the density of states of a superconducting nano-wire exposed to a strong electric field has been published. [171] Using a two step shadow evaporation process, an aluminium / aluminium oxide tunnel probe was connected to a titanium wire. The device features two side gates, that run parallel to the wire for ≈ 500 nm, close to the tunnel probe.

When reducing the supercurrent via a gate voltage, a strong broadening of the superconducting energy gap in the density of states is observed. Using the Abrikosov-Gorkov model, the authors extract the quasi-particle (QP) population of the aluminium probe, and the energy gap and quasi-particle population of the titanium wire from the tunnel current. Citing a smooth increase in QP population, the authors exclude abrupt changes to the underlying crystal or electronic structure and instead propose QP injection as an explanation for the observed effects.

The authors speculate that electron field emission from the gate is the mechanism by which the QP are created. Assuming Fowler-Nordheim emission, reasonable agreement between the expected and measured QP count is found, which leads to the conclusion that field emission is the mechanism behind the electric field effect. Two key differences with respect to classical QP injection [175–178] are noted. The first is that the energy of the injected QP should be of the order of eV_{Gate}, which is much larger than the energies accessible to the tunnel spectroscopy. The second is that the injection current is so small it is difficult to measure.

Radio frequency response

Golokolenov *et al.* have studied the radio frequency response of a vanadium Dayem bridge device. [179] They observe a bipolar shift in the resonance frequency of the device as well as a bipolar reduction of the quality factor when the supercurrent is suppressed via gating. Furthermore, it is noted that the resonance curves become more noisy at higher gate voltages. The authors find that these observations are best explained by higher losses i.e., dissipation, which is induced in the resonator via the gate. The gate induced noise is investigated and is found to increase faster at low frequencies.

Critical current enhancement and hysteresis

In one experiment –in contrast to all the others– an *enhancement* of the critical current was found, when measuring 7 and 10 nm thick Niobium-Nitrate devices, deposited on a Si/SiO_2 substrate. [180] The enhancement is bipolar in V_{Gate}, if not perfectly symmetric, and I_C is increased up to 30% at $V_{Gate} = 80$ V. The voltage was applied using the p-doped Si as a backgate, and the sample was cooled in a liquid He^4 bath. Besides the surprising increase of I_C, also a hysteresis in the sample resistance was found when sweeping V_{Gate} at fixed biasing currents. The hysteresis is more prominent at higher biasing currents.

The authors suggest that the I_C enhancement might be due to surface nucleation and pinning of Abrikosov vortices. In this scenario, I_C is limited by the Bean-Livingston barrier that determines vortex nucleation, and movement across the film, which induces dissipation and the loss of superconductivity.

A gate voltage induced enhancement of this barrier can thus explain the observed increase of I_C.

With regards to the hysteresis, the authors propose that it could arise as a result of charge pinning at surface inhomogeneities. The increase of the hysteresis at larger bias currents can be connected to the increased range of the quasi-normal states, or intrinsic thermal fluctuations, at higher currents. The hysteresis is therefore not attributed to the phase dynamics of the superconductor.

A hysteresis was also independently reported in Ti micro bridges on a Si/SiO_2 substrate, which was attributed to ionic transport in the substrate. [171] Interestingly, the same device also shows a brief enhancement of I_C, when sweeping V_{Gate} down from a point where I_C is completely suppressed. Though it should be noted that this enhancement has very different characteristics and might stem from a different origin.

5.3 Phenomenological theory

In response to the discovery of gate-controlled superconductivity, there has been some effort to find ways by which an electric field could effect metallic superconductors. Already in the first work [145] a phenomenological theory was formulated to describe the field induced suppression of I_C, assuming the electric field is directly responsible for the effect.

Starting from the free energy density and using Ginzburg-Landau theory, an energy associated with the penetration of the electric field is incorporated. The observation that, while the critical current is affected by the electric field, the critical temperature is not, imposes strong limitations on the possible relations between the electric field energy term and the superconducting order parameter ψ. It turns out that the only way the field can affect the condensate is in the form $\nabla\psi$, which describes a spatial deformation of the order parameter. The main result is the expression for the critical current

$$I_C(T, V_{\text{Gate}}) = I_C^0 \left(1 - \frac{T}{T_C}\right)^{3/2} \left[1 - \left(\frac{V_{\text{Gate}}}{V_{\text{Gate}}^C}\right)^4\right]^{3/2}, \tag{5.2}$$

where I_C^0 is the critical current of the unperturbed device, T_C is the critical temperature and V_{Gate}^C is the critical gate voltage, for which $I_C = 0$. While this simple model is purely phenomenological and does not offer any microscopic explanation, it captures the main features of the observed physical phenomena.

5.4 Gate-controlled superconductivity as quasi-particle injection

There has been an ongoing discussion regarding the underlying mechanism behind gate-controlled superconductivity. While the observed effects were initially interpreted as a result of the electric field acting on the superconductor, others have instead suggested that the effect can be explained as the result of heating via electron (or quasi-particle) injection. In this scenario, the temperature of the electron bath would be raised via the injection of high energy electrons via Fowler-Nordheim emission from the gate. This heating then suppresses the superconducting order parameter and by extension the supercurrent.

In the following sections, an overview of arguments for and against this interpretation is presented.

Arguments for heating by particle injection

A straightforward explanation for the observed effect would be quasi-particle overheating, by injecting electrons from the gate either via the substrate or via the vacuum. Injecting 'hot' electrons in a controlled manner has been used to control the supercurrent since the 1960s. [175–178] One difference with respect to these works is that in the devices considered now, the energy of the injected electrons is expected to be much higher ($\sim eV_{\mathrm{Gate}}$), while the injection current would accordingly be much lower, and thus also harder to observe. Three independent works[2] have arrived at the conclusions that electron emission from the gate is the driving mechanism behind the effect. We will briefly review their results and reasoning.

Quasi-particle population in RF measurements

When studying the radio frequency response of Dayem bridges, the authors found that the device response is best explained by higher losses i.e., dissipation, which is induced in the resonator via the gate. [179] According to the authors, the increase in noise is inconsistent with a scenario where the junction is not heated, as in this case the integrated supercurrent noise should decrease proportionally to I_C^2. Using noise histograms, it is shown that the device is in thermal equilibrium at 20 V (before I_C is reduced), but is out of equilibrium at 50 V (when I_C is close to zero). Moreover, it is shown that the non-equilibrium distribution of the quasi-particle population is less pronounced at higher temperature, as is to be expected due to a stronger electron-phonon coupling. All these observations point to either a direct heating of the constriction, or to an increased dissipation as a consequence

[2]These are the only articles published on the topic, in which my research group has not been involved, at the time of writing.

of the electric field. The authors fit the gate leakage current with the Fowler-Nordheim model [172], which describes electron emission from solids by an electric field, and find an excellent fit. Thus, it is concluded that electron emission is the origin of the heating.

Quasi-particle population observed via tunnel spectroscopy

In the work of Alegria *et al.* [171], the density of states of a Ti wire (continues or terminated on one side) is investigated via a nearby Al/AlO_x tunnel probe. A strong broadening of the density of states is observed and via modelling the authors find a smooth increase in quasi-particle population that accompanies an increasing gate voltage. It is argued that the smooth onset of the effect, rules out that "a change in the underlying electronic or crystal structure, is responsible for the suppression of superconductivity." Moreover, the work investigates whether or not the broadened density of states can be explained via a magnetic mechanism, and arrives at the conclusion that the broadening is simply thermal in nature. The authors note that energy of the injected quasi-particles ($\sim eV_{\mathrm{Gate}}$) is inaccessible to the spectroscopy, and that the leakage current is difficult to measure. Finally, the authors conclude that electron emission from the gate is the underlying mechanism, based on the fact that the quasi-particle density in the Aluminium probe "roughly follows $x \sim exp(-V_0/V_{\mathrm{Gate}})$ for $V_0 = 2$ kV". Furthermore, the quasi-particle population in the Ti wires is simulated via a simple kinetic model, that can largely explain the observed quasi-particles.

Leakage currents and supercurrent suppression

While investigating the possibility to exploit the effect to make fast, cryogenic superconducting switches Ritter *et al.* [170] report a correlation between the gate (leakage) current and the critical current suppression across many devices, made from titanium, titanium nitrate, and niobium on varying substrates. Notably, asymmetry in the dependence of I_C on V_{Gate} is found in several devices on Si and on a 25 nm thick SiO_2 layer of thermally grown on top of Si (see also the section "The bipolarity of the effect" below). Moreover, Alegria *et al.* also report a hysteresis (and an associated asymmetry) found when measuring devices with a backgate on a SiO_2 substrate, which they interpret as a sign of "ionic transport". [171]

The spatial extension of the effect is investigated also here, which is found to decay over several µm. The suppression of the supercurrent is markedly different depending on whether or not the current close to the gate is suppressed below the retrapping current I_R or not. This is likely related a situation in which some parts of the wire are normal, while other are still super, and where Joule heating dynamics determine the spread of the normal regions.

Arguments against heating by particle injection

While the heating by quasi-particle injection is a straightforward interpretation, there are features of the effect that suggest a different mechanism, and a consensus has not yet been reached.

Temperature dependence

One observation that might suggest the effect is not a *simple* heating, is that gating becomes less effective as the temperature increases. Given the strong reduction of the superconducting gap $\Delta(T)$ for $T \gtrsim 0.4\ T_C$, any extra heat originating from the gate should markedly reduce the pairing strength and by extension I_C, but the opposite is observed. However, a careful consideration should take the enhancement of electron-phonon coupling at higher temperatures into account, since it is possible that at higher temperatures, high energy quasi-particles dissipate more heat directly to the phonon bath, instead of dissipating it to other quasi-particles first. Thus, further research is needed, but at first glance the observed temperature dependence seems incompatible with the heating interpretation.

The independent action of two gates

When gating a titanium constriction from two sides, the effects of the gates on either side do not add up. [163] If the gates were heating such a narrow constriction, one would expect that their contributions sum, at the very least partially, although here again one should carefully analyse the dynamics of joule heating in these devices to be sure.

The bipolar nature of the effect

Electron emission is strongly dependent on the magnitude of the electric field, which is dependent on the geometry of the gate and wire or constriction. The typical design, that features a pointed gate perpendicular to a wire or constriction, is strongly asymmetric.[3] In this case, it is reasonable to expect that significantly different voltages are required in order to reach the field magnitude necessary to extract electrons from the gate and from the wire or constriction (i.e. positive and negative V_{Gate}). This has been confirmed via finite element calculations. [169] Such an asymmetry is thus important as it is a telltale sign of electron emission. Moreover, while electrons pulled from the gate would have a high energy upon hitting the superconductor, and thus the ability to generate many quasi-particles therein, the reverse is not true. Electrons pulled from the superconductor by a reversed field,

[3] The devices presented by Ritter *et al.* that showed and asymmetric V_{Gate} effect feature such a perpendicular gate, although it is more rounded than pointed.

will have leave holes near the Fermi energy, and can not easily account for a large increase in quasi-particles in the superconductor.

In the vast majority[4] of reported measurements, such an asymmetry is not found, raising doubts regarding the electron emission scenario.

Phase slip dynamics

The observation that gating one constriction of a SQUID [167], affects the phase of the other junction ~ 8 μm far away, can not be easily explained in terms of heating. Perhaps even more tellingly, the SQUID current vs flux relation showed phase shifts even at low gate voltage that did not effect the critical current.

Likewise, the complex behaviour and shape of the supercurrent switching distributions [168] do not seem compatible with simple thermal effects. In this work, the switching current probability distributions (SCPD) were measured at various temperatures and gate voltages to investigate the phase slip [181, 182] dynamics of a Ti Dayem bridge under the effect of a strong electric field generated by the usual planar side gate.

The device was modelled with the resistively and capacitively shunted junction theory, and the inverse Kurkijrvi-Fulton-Dunkleberger transform was used to describe the probability distribution. Depending on the temperature, three regimes are found, where the phase slips are either quantum in nature (low temperature), thermally activated (medium temperature), or multiple and thermally activated (high temperature). When comparing the SCPD as a function of temperature and as a function of gate voltage, a starkly different behaviour is found. For the same value of the critical current, the distributions where I_C is suppressed by the gate are much wider than those were I_C is suppressed by temperature. In fact, the distribution shape under influence of the gate is broadened to such a degree that it can not be described by the aforementioned model, as it leads to unrealistically high temperatures. This indicates that the action of the gate does not lead to a state with thermal equilibrium.

The leakage current

It is hard to completely exclude any unwanted carrier injection when biasing the gate with a voltage source, due to the fact that a leakage current will always be present in any system, and because of the very small currents that would be needed to heat up the superconductor. During all the experiments presented here, the leakage current was carefully monitored by applying a gate voltage in the usual manner, while one lead of the device is connected to a sensitive room temperature differential current pre-amplifier that functions as the ground, with all other leads are left floating. The leakage currents

[4] Ritter *et al.* is the notable exception.

thus measured vary between different set-ups, but leakage resistances of the order of TΩ are typical. Depending on the measurement set up and the substrate used, the leakage current between the gate and device at full supercurrent suppression typically varies between $\sim 10^{-10}$ A and $\sim 10^{-15}$ A, which correspond to a differential resistance of $\sim 10^{11}$ Ω and $\sim 10^{15}$ Ω, respectively. [145, 163]

Furthermore, due to inconsequential leakage in e.g. the system wiring, the absolute value of the leakage current alone is unreliable. Instead, the exponential behaviour predicted by the Fowler-Nordheim model [172] would be a more useful indication of field emission from the gate. However, Paolucci *et al.* [174] reported that such a correlation between the leakage current and the gate effect was not found, in disagreement with Ritter *et al.* [170], which report the opposite.

It is unlikely that electrons are emitted from the gate into the superconducting wire or vice versa via the vacuum, as even a single electron thus accelerated would have enough energy to quench superconductivity. [52, 112, 165, 169] A gradual reduction of I_C would thus not be observed. This observation is corroborated by the fact that the effect is also observed when using a backgate. Hence, electron injection via the vacuum is incompatible with the reported observations.

Ruling out electron injection via the substrate is not so simple. In an attempt to minimise any possible leakage current through the substrate, many samples have been fabricated on sapphire substrates, which is a much stronger insulator than SiO_2. The behaviour and strength of the effect does not appear to be significantly influenced by the choice of substrate, which can be expected if high energy electrons have to move from the gate, through the substrate, to the device (or vice versa). However, due to the difficulty of determining how much of the measured leakage current flows between gate and device, and due to variations in device geometry, this is certainly not conclusive evidence.

More compelling is a set of measurements on a gated Ti wire that is suspended above the substrate. [169] These devices were specifically designed to rule out possible charge injection or phonon-mediated heating via a substrate. The observed field effect is fairly –though not completely– typical. As usual, the effect is symmetric in V_{Gate}. Atypically, three separate critical currents are identified, that have various magnitudes and are accompanied by three critical temperatures. These are attributed to three separate weak links in the wire caused by inhomogeneities in Ti film. Also noteworthy is the temperature behaviour of the I_C suppression. Typically, the plateau where V_{Gate} is ineffective, widens with increasing temperature, while the critical gate voltage V^C_{Gate} for which $I_C = 0$ is unchanged (see Fig. 5.2). In these samples however, the plateau shrinks at higher T, and V^C_{Gate} is reduced. This difference is likely due to the reduced thermal coupling between the wire and the substrate, compared to the standard devices.

Gating via an ionic liquid

Finally, another experiment, ongoing as of the writing of this thesis, that aims to exclude electron injection as the driving effect, is gating via an ionic liquid. The experiment, including preliminary results, is presented and discussed in detail in chapter 6.

The rational behind the experiment is that it is impossible to categorically exclude the presence of any quasi-particle injection while using solid state back-, or side gates. This problem can be circumvented by using a so-called ionic liquid for gating instead. Ionic liquids are a type of electrolyte, that do not permit electronic transport, but have a moderate to high ionic conduction. While the material is liquid (e.g. at room temperature), it can be polarized between two electrodes, such as a device and a large metal pad. This leads to the formation of a layer of negative ions on one, and positive ions on the other surface. The sample is then cooled down, and when the liquid freezes the ionic charges become fixed in place. Thus, a strong electric field is maintained without an external voltage source.

5.5 Summary and conclusions

A brief historical review of the study of the effect of electric fields on superconductors has been given, followed by a summary of the characteristics of gate-controlled superconductivity. Furthermore, the question of whether the effect can be understood to arise from the injection of high energy quasi-particles emitted from the gate has been thoroughly reviewed.

Chapter 6

Ionic Liquid-Gated Superconductivity

As we have seen in section 5.4, there is an ongoing discussion on the mechanism underlying gate suppressed superconductivity. Since it is very hard, if not impossible, to completely rule out a leakage current when using a back gate or side gate, a different approach is required. By instead using a polarized ionic liquid to provide the electric field, a leakage current can be categorically ruled out. In this chapter, preliminary results of an ongoing experiment, where Niobium Dayem bridges are gated via an ionic liquid, are reported.

6.1 Introduction

The term ionic liquid is generally used to describe materials that are purely ionic in nature, and are liquid at temperatures below 100 degrees Celsius. However, the melting point is often much lower. The liquid used in the experiment, DEME-TFSI, has no clear transition point but undergoes a glass transition 182 K. [183] They are typically not volatile, and most crucially,

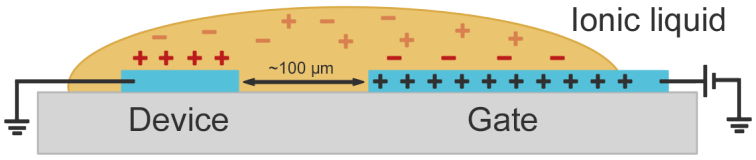

Figure 6.1: A schematic illustration of ionic liquid gating. By applying a voltage to the gate, the ions in the liquid move to screen the gate charges, and the liquid is polarized between the gate and the device. Below ≈ 200 K, the liquid freezes and the ions are held in place, even when the gate voltage source is disconnected.

have relatively high ionic conductivity but do not permit electronic transport.

When the compound is liquid, it can be polarized between two electrodes that are covered by the liquid, in our case the device on one side, and a large pad on the other. In response to applying a DC voltage between the electrodes, the ions in the liquid will move to screen the electric field, forming a charged layer on the electrode surfaces, the so-called electronic double layer [184]. The negative electrode is thus covered by a layer of positive ions, and the positive electrode is covered by a layer of negative ions, while the bulk of the liquid remains neutral. The density of the charge at the electrode surface depends on the voltage that is used to polarize the liquid, and the ratio between the surface areas of the electrodes, as the electrode with the smaller surface limits how much charge is moved.

Once the liquid is polarized, it can be cooled down while maintaining the polarizing voltage and thus the configuration of the ions. After the liquid is solidly frozen at low temperature, the ions are locked in place. When the polarization voltage is removed, the dense layer of ions remains on the electrode surfaces, providing a strong electric field, while the two electrodes are electrically isolated from each other.

As the charged ions are situated directly on the surface, fields as strong as 10^{10} V/m can be induced with a polarization voltage of a few V.[1] As such, large charge modulations can be induced at the surface of materials. [185–189] This technique has been widely applied to systems with a low intrinsic carrier concentrations. In the context of superconductors, it has used on high T_C, cuprate superconductors where T_C was increased due to the electrostatically induced doping. [190] Experiments have also been done on metallic superconductors. In thin-film superconductors reversible, $\sim 1\%$ variations of T_C have been observed, which are attributed to the modulation of the charge carrier density. [191–194]

6.2 Methods

Dayem bridges with a width $w \approx 120$ nm and length $l \approx 100$ nm have been fabricated via single step electron beam lithography. A $d_{\mathrm{Ti}} \approx 10$ nm thick layer of Ti is sputtered on a sapphire substrate as a sticking layer, followed by a $d_{\mathrm{Nb}} \approx 50$ nm thick layer of Nb. The fabrication procedure is completed by lift-off and gentle sonification in acetone, see also appendix A.3 for details. Devices produced with this procedure typically have a critical temperature T_C ranging between 5.5 and 8 K, depending on the details of the procedure and device geometry.

The measurements presented in this chapter have been performed in an *Optistat Dry BLV* cryostat, that has a base temperature of ≈ 2.3 K. For details on the measuring setup, see Appendix A.4 The ionic liquid utilized

[1] The ionic liquid used, DEME-TFSI, breaks down around 5 V.

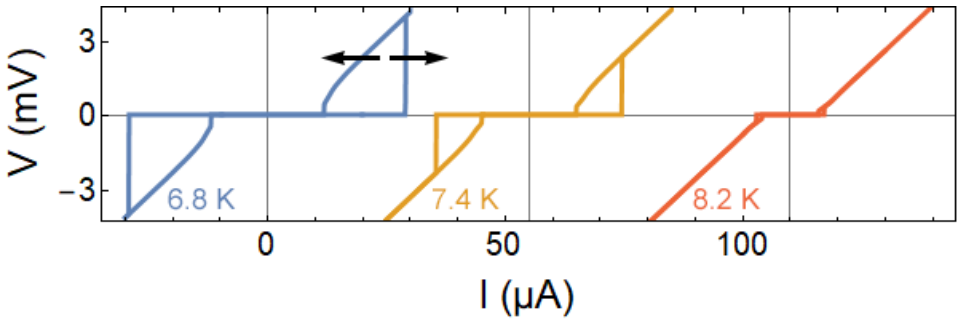

Figure 6.2: Three IVs taken at ≈ 6.8, 7.4 and 8.2 K, horizontally offset for clarity. I_C is ≈ 29, 20, and 7 μA, while I_R is ≈ 12, 10, and 6 μA respectively. Arrows indicate sweep direction.

is generally known as DEME-TFSI, which is widely used and commercially available. A droplet of the liquid is carefully placed in such a manner that it covers a large section of a large pad that is used as one electrode, and three devices that are used as the other electrode. To prevent the liquid from moving, the sample holder has been adapted so that the sample is in a horizontal position.

In order to polarize the liquid, a voltage is applied to the large metal pad designed for this purpose, always at room temperature, see Fig. 6.3. The set voltage is maintained throughout the cooldown and measurement.

6.3 Results

Device characteristics

Fig. 6.3 shows false colour SEM images of a representative device. At base temperature $T \approx 2.3$ K, the constriction has a normal state resistance of $R \approx 12\ \Omega$. Fig. 6.4 shows the critical and retrapping currents versus temperature, which have been measured up to 300 μA, after applying the liquid. The dependence of I_C on T is fitted with the empirical Bardeen's profile $I_C \cong I_C^0[1 - (\frac{T}{T_C})^2]^{3/2}$ [195–197].

The critical temperature measured $T_C = 9.1$ K, is very close to the bulk value of 9.2 K. However, due to problems with the temperature sensor, the temperature measurement was not properly calibrated, and the temperature measurement must not be taken to be precise. Comparing the measurement with those taken before the application of the ionic liquid, when the temperature controller was working properly, the real temperature is likely at least 1 K lower.

The IV characteristics show a hysteresis typical for such superconducting devices, see Fig. 6.2. The hysteresis is likely thermal in origin [198–200], and is weaker at higher temperatures, due to an enhanced electron-phonon

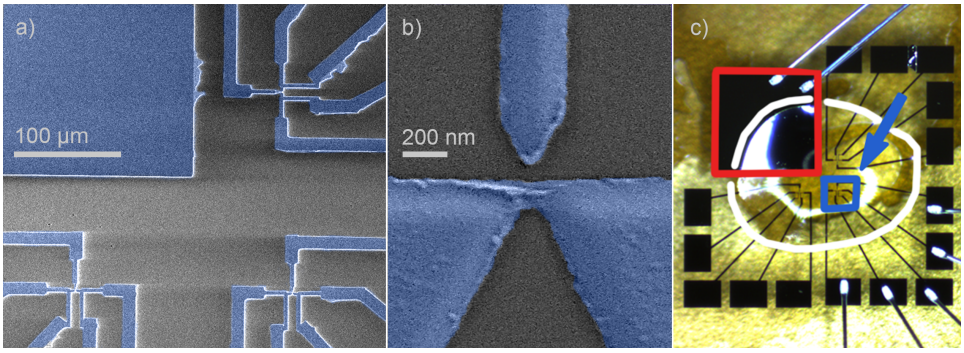

Figure 6.3: a) Coloured SEM images showing three devices near the large metal pad that is used to polarize the ionic liquid. Every device features four leads to allow for four-wire measurements, and a side gate. b) A coloured SEM close up of a representative device, showing the Dayem bridge and side gate. c) A bonded sample with the ionic liquid applied. The gate is outlined in red, the ionic liquid drop in white, and the sample in blue.

coupling improving thermalization.

Ionic liquid gating

Fig 6.5a shows how the critical current I_C is affected, when polarizing the liquid up to 4 V in 1 V steps. Initially, there is little effect. At $V_{\text{Liquid}} = 1$ V, the device occasionally switches early to the normal state, but in general the I_C is close to I_C^0, where the liquid was unpolarized (see the grey line). Starting from 2 V, the magnitude of I_C becomes slightly reduced, and the critical current profile becomes irregular. At 4 V I_C is noisy and significantly reduced at low temperature. Closer to T_C, the reduction of I_C appears to be limited by the retrapping current I_R, which itself was never effected in these measurements.

After these measurements, the polarization voltage was swept down to 0 V (as always at room temperature), see Fig. 6.5b. Now back at 0 V, the effect is as strong as before. This is not too surprising, as ionic liquids are known to be strongly hysteretic. Fig. 6.5c shows the evolution of I_C as the polarization voltage is swept down to -4 V in 1 V steps. Moving into the negative voltages, I_C recovers, indicating that the liquid is now depolarizing. At -3 V and -4 V, many points coincide with the original I_C^0, yet the devices switches to the normal state early on several occasions as well, so that the switching distribution is more irregular than before. It is unclear what exactly drives this behaviour. Partial inhomogeneous polarization / depolarization of the liquid might play a role.

To map the range of the switching distribution, I_C has been measured 30 times at various temperatures at -4 and 4 V, see Fig. 6.5d. Again we see

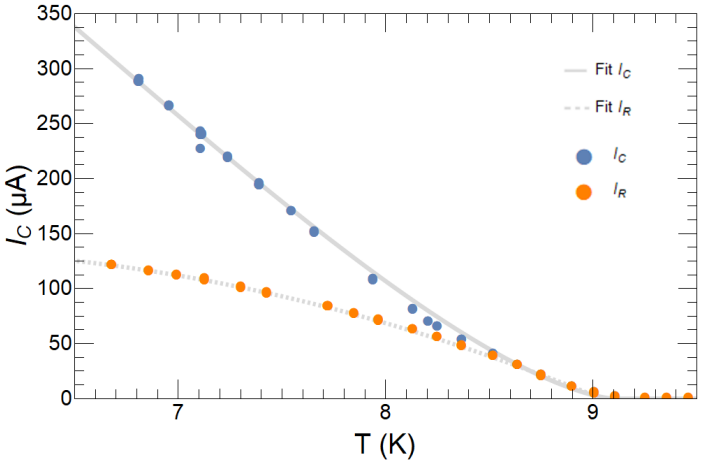

Figure 6.4: The critical current I_C and the retrapping current I_R of the device as a function of temperature, after the liquid has been applied, but before it is polarized. I_C shows typical BCS behaviour and is fitted with Bardeen's profile (see main text for details). I_R is fitted with a simple quadratic function. The fits will be used as a reference in Fig. 6.5.

that at 4 V, the switching distribution is limited by the retrapping current I_R. On the other hand, the maximum I_C is clearly below I_C^0. At -4 V, the suppression of I_C is less strong, but there is still a noticeable spread in the switching distribution. A large broadening of the supercurrent switching distribution has been observed previously in side gated Ti Dayem bridges as well. [168]

6.4 Discussion

The results presented in this chapter show that the supercurrent through a Nb Dayem bridge can be affected and reduced by gating via an ionic liquid. For the parameter range explored in these measurements, the suppression of the critical current seems to be limited by the retrapping current, which itself was never affected. This suggest that thermal effects play an important role. Such behaviour is consistent with experiments performed with a side or back gate, where I_R is affected only after I_C is already strongly suppressed down to similar values, see also Sec. 5.2. In conjunction with a suppression of I_C, the gating induces a strong broadening of the switching distribution.

As the electrolyte is electrically insulating, and as the effect persists without an external voltage applied, the injection of high-energy quasiparticles can be ruled out. Together with other observations discussed in Sec. 5.4 that appear inconsistent with the electron emission hypothesis, presented previously, this is strong evidence that quasiparticle emission / injection is

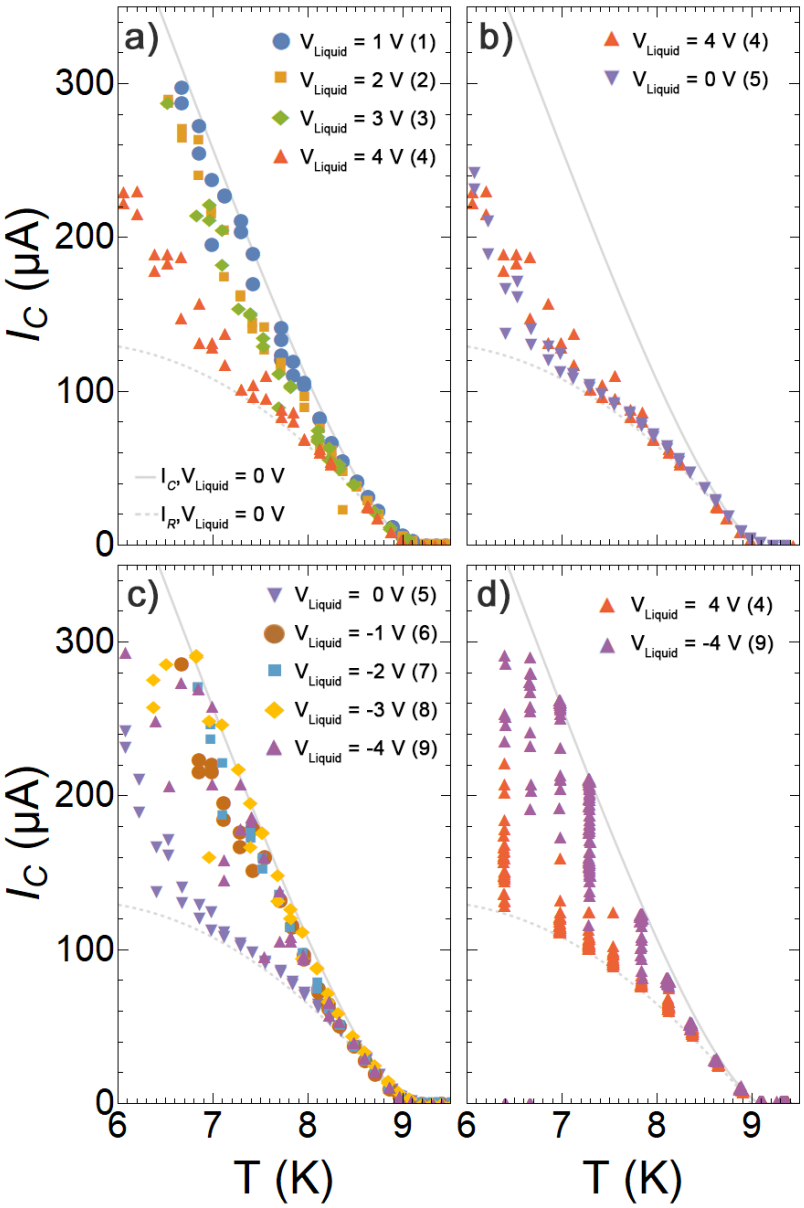

Figure 6.5: I_C versus temperature at various liquid polarization voltages. The original I_C and I_R are indicated by the solid and dashed grey lines, respectively. For a) - c), two values of I_C are measured per temperature. The order of the measurements is indicated in the legend by the number in parenthesis. a) Polarizing the liquid up to 4 V in 1 V steps. b) I_C at 4 V and after the liquid polarization voltage source has been ramped back to 0 V. c) Sweeping down from 0 V to -4 V in 1 V steps. d) Thirty points measured per T with the V_{Liquid} at 4 and -4 V.

not the fundamental mechanism underlying the effect.

While the experiments presented in Refs. [191–194] are superficially similar, they were focused on measuring the device resistance as a function of temperature $R(T)$, to determine the critical temperature T_C. Only Choi *et al.* show measurements of the critical current I_C, taken at $T = 1.9$ K $\approx 0.5\ T_C$. Starting from $I_C \approx 208$ μA (unpolarized liquid), a small modulation ≈ 18 μA is reported between $V_{\text{Liquid}} = -4$ V and $V_{\text{Liquid}} = 5$ V. Notably, the devices used in that study are both much thinner (8 nm versus 50 nm), and much wider (10 μm versus 120 nm), which suggest that the device dimensions might play a crucial role.

Further, more detailed and extensive measurements are required to fully explore the effect of ionic liquid gating on metallic Dayem bridges, and to shed light on if or how it differs from side or back gating. What the mechanisms underlying the field effect is, remains unsettled. Any theory describing the effect will have to account for the observed increase in quasi-particle population, and its exponential quality.

In the next chapter, a recently proposed microscopic theory is introduced. Furthermore, gate-controlled superconductivity is investigated in combination with in-, and out-of-plane magnetic fields, and the aforementioned theory is extended, in an attempt to understand the fundamental properties of the effect.

Chapter 7

Gate-induced suppression of the Supercurrent in Magnetic Fields

The content of this chapter is based on the publication *Unveiling mechanisms of electric field effects on superconductors by magnetic field response.*

7.1 Introduction

As detailed in chapter 5, it has recently been shown that the superconducting (SC) properties of metallic Bardeen-Cooper-Schrieffer (BCS) superconductors can be influenced via electrostatic gating [174]. The most striking effect, reduction and suppression of the critical supercurrent, has been broadly demonstrated in metallic nanowires [145], Dayem bridges [161–163] made of titanium, aluminium and vanadium, as well as in aluminium–copper–aluminium Josephson junctions [166]. Moreover, recent experiments have probed the effect of electrostatic gating on the SC-phase in a SQUID [167], and on the nature of the switching current distributions in gated titanium Dayem bridges [168].

While these observations clearly indicate that the electric field can suppress the supercurrent, whether and how it acts on the amplitude or the phase of the SC order parameter are questions so far unanswered. To develop a deeper insight into this fundamental problem we investigate how the superconducting state is modified by the simultaneous presence of electric and magnetic fields. In this context, probing both the in-, and out-of-plane magnetic fields (B_Y and B_Z, respectively) is particularly relevant because the two orientations affect the superconducting thin films via very different mechanisms [201].

In thin films B_Z generally leads to screening currents and a spatially varying order parameter, marked by 2π-phase slips, as flux vortices penetrate

the sample. On the other hand, B_Y ideally only affects the pairing amplitude homogeneously via electron spin paramagnetism, inducing pair breaking and spin polarization [202, 203]. Thus, the search for magneto-electric cross-talking effects in superconducting thin films can provide indications and constraints on the quantum states at superconductivity breakdown, and reveal the origin of the unexpected coupling between the electric field and the superconducting phase and/or pairing amplitude.

In the following sections, we demonstrate that superconducting Al nano-bridges can be electrically driven into a state with complete suppression of the critical supercurrent. The magnetic field response of Al nano-bridges has been investigated with the aim to explore the nature of the phase transitions and the mechanisms that mark the electric field effects in metallic superconductors. Therefore, we have measured the effect of a strong electric field combined with in-, and out-of-plane magnetic fields, at several temperatures, on the critical current of the nano bridge.

Remarkably, we will find that the magnetic field has only a weak influence on gating effect in the superconducting bridges. Moreover, this phenomenology is starkly independent on the magnetic field orientation, despite the very different interactions between superconducting thin films and in-, and out-of-plane magnetic fields. These findings suggest the absence of a direct electric coupling between the electric field and the amplitude of the superconducting order parameter, or 2π phase slips generated by vortices. In both cases a significant variation of the superconducting/normal critical boundaries is expected in response to the presence of magnetic fields.

Our observations are consistent with a recently proposed microscopic model, in which the surface electric field is a source of inversion-symmetry breaking that strongly affects the orbital polarization at the surface layers of a multi-band SC thin film. [204] This results in an electric-field-driven phase transition into a mixed SC state where the relative SC phases between different bands are shifted by π. This state is hardly influenced by the applied magnetic field, as shown in the phase diagram, and is thus consistent with the experimental results.

In addition to the fundamental aspects, the full supercurrent suppression observed in the Al-based devices (previously only a 35% reduction was achieved for Al [145]), is relevant from the technological point of view. Considering the broad application of Al-based thin films as SC qubits [205], Josephson devices [206–208], photon detectors [35, 209] and bolometers [210], one can envision a new generation of SC electronics that can fully exploit the demonstrated gate-controlled superconductivity.

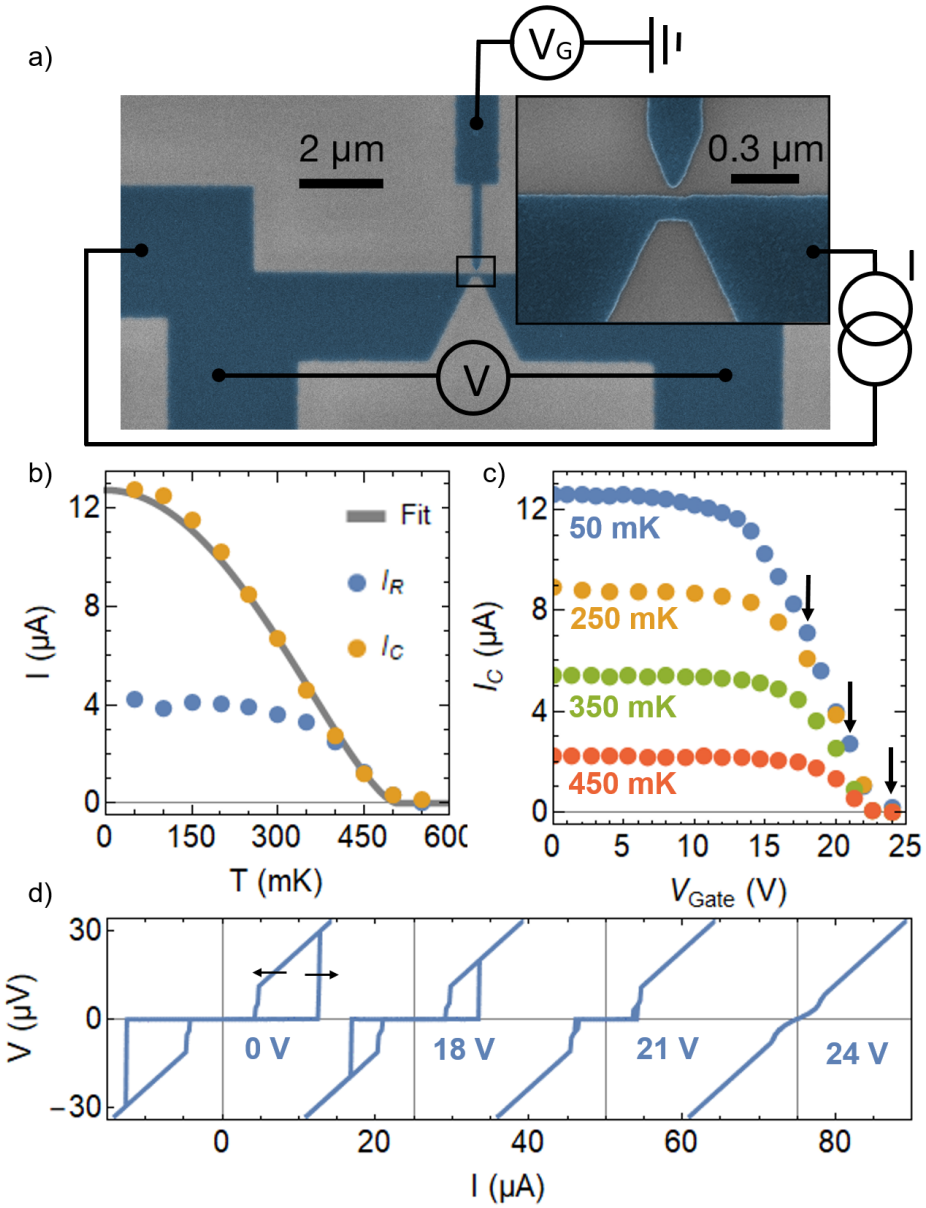

Figure 7.1: a) False colour SEM image of a typical device. Inset: close up of the region indicated by the black square showing the Dayem bridge and gate electrode. b) Critical current I_C and retrapping current I_R versus temperature. I_C follows the typical BCS evolution (gray line). c) I_C versus gate voltage V_{Gate} at four different temperatures. d) Voltage drop across the bridge versus bias current, for four values of V_{Gate} at 50 mK. Arrows indicate sweep direction, and the curves are horizontally offset for clarity. The black arrows in c) indicate the curves with $V_{\mathrm{Gate}} = 18$, 21 and 24 V.

7.2 Experimental results

Electrical characterization

From critical current measurements, we find a critical temperature $T_C \approx 500$ mK, cq. Fig 7.1b. This T_C is relatively low for Al, likely due to an inverse proximity effect from the Ti layer. Using the BCS relation, we find that $\Delta_0 = 1.764\ k_B T_C = 91$ μeV (k_B being the Boltzmann constant). Via the conductivity σ, Δ_0 and the magnetic permeability of the vacuum μ_0, we estimate the London penetration depth $\lambda_{\mathrm{L}} = \sqrt{\hbar/\mu_0 \pi \sigma \Delta_0} \approx 100$ nm, and the superconducting coherence length $\xi_0 = \sqrt{\hbar\sigma/N_{\mathrm{F}} e^2 \Delta_0} \approx 170$ nm. Here we take the electron density at the Fermi energy of aluminium to be $N_F = 2.15 \cdot 10^{47}$ $\mathrm{J}^{-1}\mathrm{m}^{-3}$ [89, 211, 212].

Fig. 7.1b shows the critical and retrapping currents versus temperature. At the base temperature of 50 mK, the critical current $I_C \approx 12.8$ μA. The evolution of I_C as a function of temperature follows the conventional Bardeen's profile $I_C \cong I_C^0[1 - (\frac{T}{T_C})^2]^{3/2}$ [195–197] . The IV characteristics show a considerable hysteresis at low temperature (see the blue dots in Fig. 7.1b and the IV curves in Fig. 7.1d, with a retrapping current $I_R \approx 4.2$ μA at $T = 50$ mK. The hysteresis is likely thermal in origin [198–200], and it disappears when $T > 400$ mK, which is consistent with an enhanced thermalization mediated by phonon coupling.

As in similar experiments [145, 162, 163, 166–168, 174], the critical current can be reduced by applying a gate voltage V_{Gate}. While at first the effect is small, I_C starts to rapidly decrease around $V_{\mathrm{Gate}} \approx 13.5$ V (at 50 mK), up to complete suppression at the critical gate voltage $V_{\mathrm{Gate}}^C \approx 23$ V. This is shown in Fig. 7.1c, for several temperatures. The effect is bipolar in V_{Gate} (not shown here) and is consistent with what has been reported for different materials [174]. V_{Gate} has little to no effect at low values until a sudden decrease close to V_{Gate}^C. At higher temperatures, the region where V_{Gate} is ineffective widens, while V_{Gate}^C is unaffected. In Fig. 7.1d, we show four IV curves for different V_{Gate}, taken at $T = 50$ mK. In line with previous field effect experiments, the retrapping current I_R is not affected by V_{Gate} until it coincides with I_C, see also Fig. 7.3. Above V_{Gate}^C some residual non-linearity lingers, before the device becomes completely ohmic (see the 24 V line in Fig. 7.1d. [174]

While the critical current is easily identified when the switch to the normal state is abrupt, this is less evident when I_C is close to zero and the transition is more gradual. We have defined I_C as the value of the bias current I for which the differential resistance is larger than 10 Ω, which is of the same order of magnitude as the normal state resistance $R_{\mathrm{N}} \approx 25\,\Omega$, and can be reliably identified over the background noise. Unlike the switching process, the retrapping generally does not occur in one step, but tends to happen in two successive events (see e.g. the 18 V line in fig. 7.1d). The

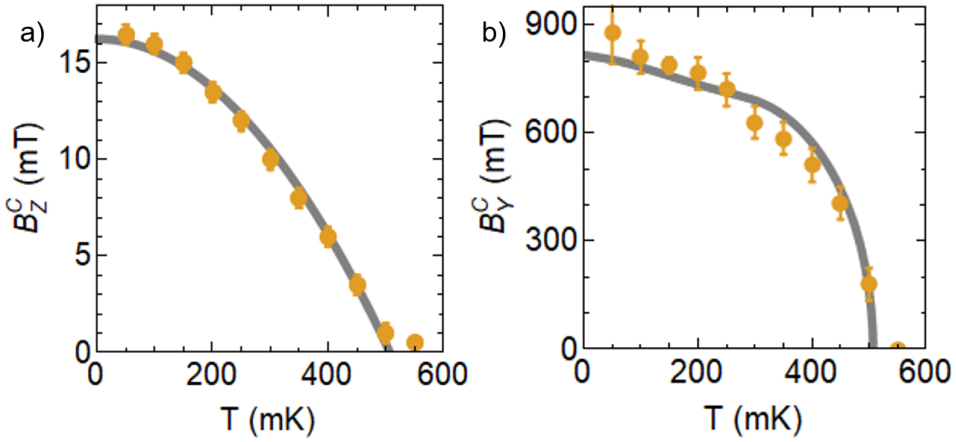

Figure 7.2: a) Critical out-of-plain magnetic field B_Z^C versus temperature, error bars indicate the resolution in B. Fitted with an empirical expression (see main text). b) Critical in-plain magnetic field B_Y^C (along the direction of the current) versus temperature. Error bars indicate the resolution in B. Fitted with the calculated temperature dependence of the critical field assuming perfect spin paramagnetism (see main text).

exact origin of this 'partial' switching is not yet fully settled, but it is likely related to two local thermalization processes taking place in different regions of the device.

The leakage current between the gate and device was carefully measured by applying a voltage to the gate in the usual manner, and amplifying the current flowing into the device using a room temperature current amplifier over a long period of time. At $V_{\text{Gate}} = 25$ V, the leakage current $I \approx 7 * 10^{-11}$ A, giving a gate-device resistance of $R \approx 0.63$ TΩ. This is of the same order of magnitude as reported in previous works [174]. Some portion of this leakage occurs in the cabling of the cryostat, as at 30 V, leakage currents of the order of 10^{-12} have been measured between unconnected cables in this cryostat.

Magnetic field response

It is well known, that magnetic fields suppress superconductivity. In particular, in-, and out-of-plane magnetic fields affect superconducting thin films very differently. The out-of-plane field B_Z induces screening currents, and is thus an orbital effect. However the thin nature of the film, prevents such a response to the in-plane field, here referred to as B_Y. Thus, the main impact of B_Y is its coupling to the electron spin, and a much larger field is required to disrupt superconductivity.

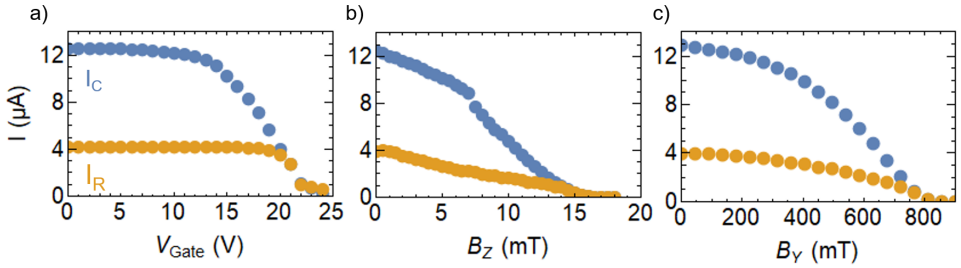

Figure 7.3: a) The critical and retrapping current versus gate voltage, b) out-of-plane field B_Z and c) in-plane field B_Y.

In Fig. 7.2a, we show the critical out of plain field versus temperature, where the error bars indicate the resolution in B_Z. The data is fitted with the phenomenological expression $B_Z(T) = B_Z(T=0)(1-(T/T_C)^2)$ [213], which yields $T_C = 507$ mK and $B_Z(T=0) = 16.25$ mT. Fig. 7.2b, shows the critical in-plane field $B_Y^C(T)$, fitted with a calculation of the temperature dependence of the critical in-plane field assuming a homogeneous spin splitting, also minimizing the free energy. [203, 214, 215] At $T = 50$ mK, the critical field $B_Y^C \approx 850$ mT.

Via the two critical magnetic fields, we estimate the London penetration depth $\lambda_{\mathrm{L}}^{\mathrm{GL}} \approx B_Y^C d/B_Z^C\sqrt{24} = 160$ nm [213] via the Ginzburg-Landau theory using d = 17 nm. Since the thickness of the SC film is $d \ll \lambda$, it is reasonable to assume that the in-plane field B_Y penetrates the superconductor completely. Indeed, the critical in-plane field's temperature dependence $B_Y^C(T)$ is consistent with the evolution of a spin-split BCS condensate with a critical Zeeman field near the Clogston-Chandrasekhar limit $\mu_{\mathrm{B}}H_C = \Delta_0/\sqrt{2}$ [203, 214, 215].

Fig. 7.3 shows the behaviour of the critical and retrapping currents as a function of V_{Gate}, B_Z and B_Y. While for the magnetic fields, both I_C and I_R are immediately suppressed, this is not the case when a gate voltage is applied. Instead, there is a region where I_C is not or hardly effected. Moreover, when considering the effect of V_{Gate}, the retrapping current remains unaffected, even when I_C is already significantly reduced. Only when I_C is reduced to a value comparably to the original I_R, the latter is affected, and from that point on the two coincide.

Combined electric and magnetic fields

The simultaneous application of magnetic and electric fields is shown in Fig. 7.4, where the evolution of I_C is plotted as a function of both temperature T and out-of-plane magnetic field B_Z. The reduction of I_C is monotonous in B_Z and T.

It is interesting to compare the dependence of I_C on T and B_Z, with

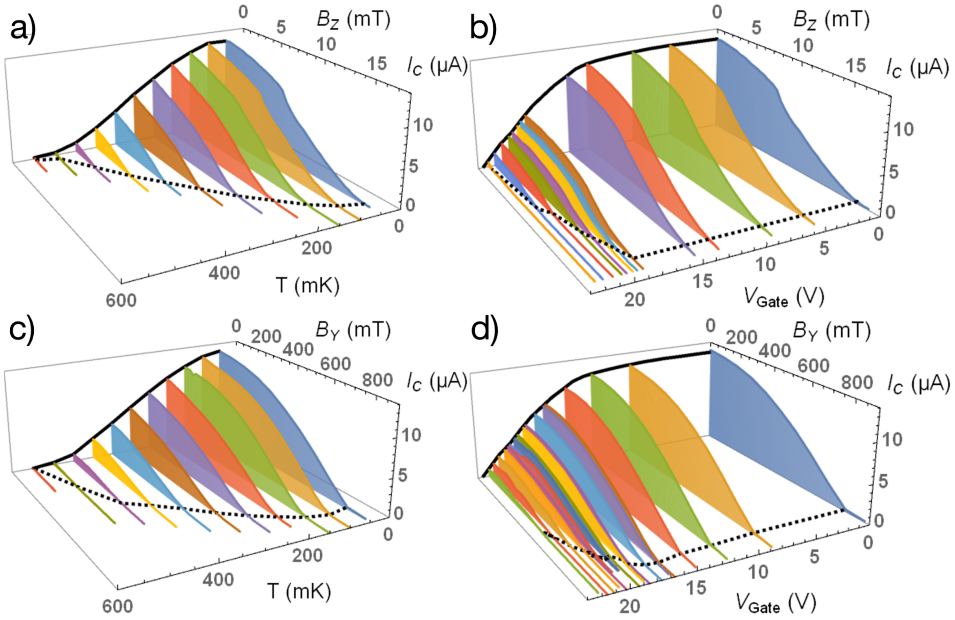

Figure 7.4: a) 3D plot of I_C as a function of the out-of-plane magnetic field B_Z and temperature T. The full black line shows $I_C(T)$ at zero field, the dashed black line shows the critical field B_Z^C versus temperature. b) 3D plot of I_C as a function of the out-of-plane magnetic field B_Z and the gate voltage at 50 mK. The full black line indicates $I_C(V_{\mathrm{Gate}})$ at zero field, the dashed black line indicates the critical field B_Z^C. c) 3D plot of I_C as a function of the in-plane magnetic field B_Y and temperature T. The full black line shows $I_C(T)$ at zero field, the dashed black line shows the critical field B_Y^C versus temperature. d) 3D plot of I_C as a function of the in-plane magnetic field B_Y and the gate voltage at 50 mK. The full black line indicates $I_C(V_{\mathrm{Gate}})$ at zero field, the dashed black line indicates the critical field B_Y^C.

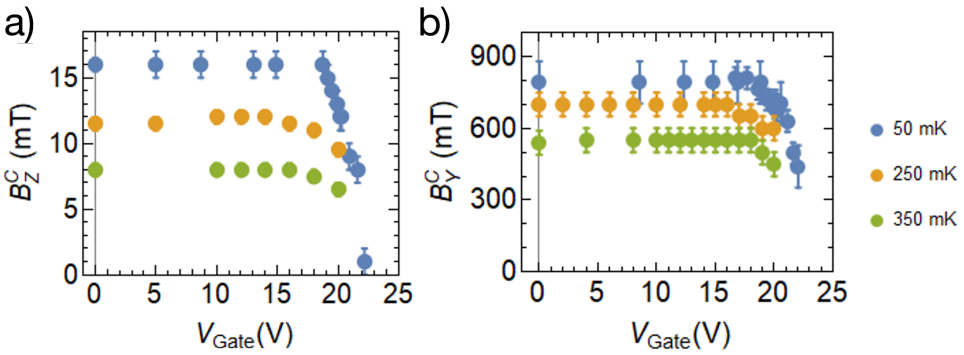

Figure 7.5: c) Critical field B_Z^C versus V_{Gate} at $T = 50$, 250 and 350 mK. The error bars indicate the resolution in B_Z. f) Critical field B_Y^C versus V_{Gate} at $T = 50$, 250 and 350 mK. The error bars indicate the resolution in B_Y.

the dependence on V_{Gate} and B_Z, which is presented in Fig. 7.4b. While the critical magnetic field B_Z^C decreases continuously with temperature, the same is not true for V_{Gate}. For $V_{\mathrm{Gate}} < 17$ V, the B_Z^C appears unaffected. Only when V_{Gate} exceeds this value, we see a reduction in both I_C and a sharp decrease of B_Z^C. The dependence of B_Z^C on V_{Gate} is shown in Fig. 7.5a, for three different temperatures. At higher T, the onset of the reduction of B_Z^C is not drastically changed, although B_Z^C is slightly reduced at lower values of V_{Gate}.

The complete evolution of I_C as a function of both T and B_Y is shown in Fig. 7.4c. Analogous to the effect of B_Z, I_C is reduced monotonously. Also the behaviour of I_C versus T and V_{Gate} is similar; for $V_{\mathrm{Gate}} < 17$ V, the dependence of I_C on B_Y is not significantly affected. Fig. 7.5b depicts the evolution of the critical magnetic field B_Y^C versus V_{Gate} for several T.

Even though the two magnetic field orientations affect the superconducting device via very different mechanisms, the effect of V_{Gate} on B_Z^C and B_Y^C is remarkably similar. Notably, the critical magnetic field values are not affected until $V_{\mathrm{Gate}} \approx 17$ V. This is unlike the behaviour of I_C, which is already reduced by$\approx 30\%$ at $V_{\mathrm{Gate}} = 17$ V (see Fig. 7.1). For neither B_Z nor B_Y does the relation between I_C, B and V_{Gate} depend on the sign of either B or V_{Gate}.

7.3 Microscopic theory, introduction

Recently, a microscopic theory has been proposed [204] that aims to describe gate-controlled superconductivity. The theory is built on the idea that the electric field breaks inversion symmetry at the surface of the superconductor, inducing an emergent Orbital Rashba (OR) interaction that leads to a mixing of atomic orbitals that does not exist in an inversion symmetric environment. The induced orbital polarization affects the electron pairing within a certain distance of the surface. The effect is expected to be ubiquitous in metals as well as in semiconductors, since it can occur in pure $p-$, and $d-$ orbitals, as well as in $-sp$ and $-sd$ hybridized configurations.

The superconducting thin film is modelled as a stack of 6, 12 or 30 layers, and conventional spin-singlet pairing is assumed. The electronic orbitals are described as $d-$orbitals that belong to the $t2g$ sector the tetragonal symmetry i.e. yz, xz and xy, and in the surface layer an orbital dependent asymmetric coupling is present. A standard Hamiltonian that describes layered superconductors with multiple bands at the Fermi energy level and conventional intra-orbital spin-singlet pairing is formulated. Importantly, orbital Rashba couplings close to the surface are also incorporated. A computational analysis is performed, in which the superconducting order parameters, that correspond to a minimum of the free energy, are determined self-consistently until the desired accuracy is reached.

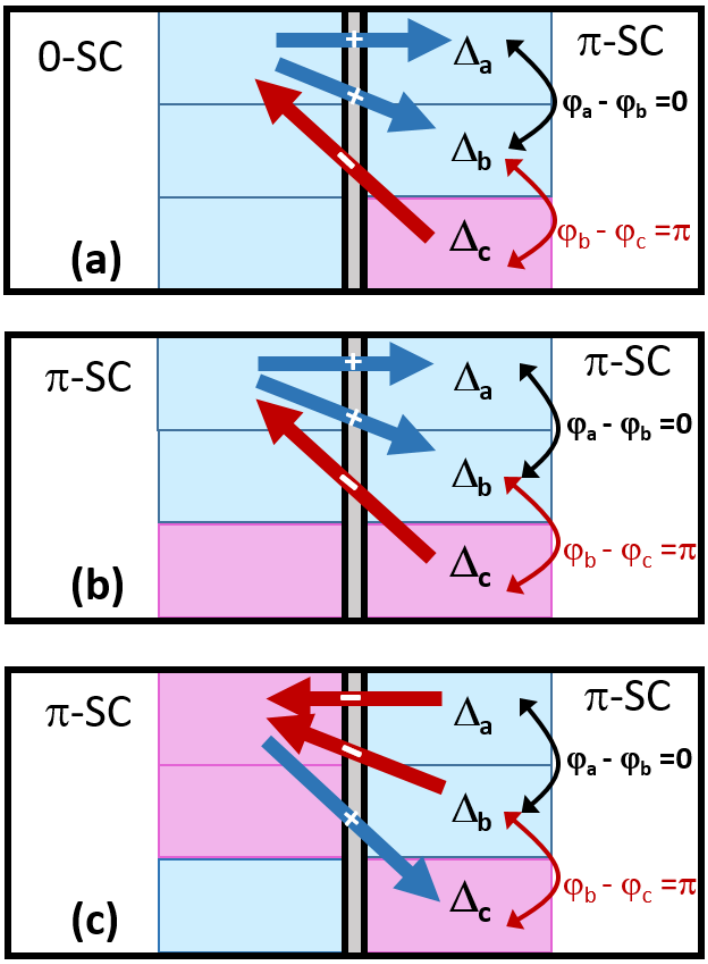

Figure 7.6: (a) Schematic description of the competing directions among Josephson pair currents (arrows) at the interface between superconducting domains having a multiband character with 0- and π-phase (a) or with π-phases on both sides (b)-(c). For graphical clarity we have depicted only the arrows from the a bands to all the other bands across the interface. Taking into account the charge transfer processes at the interface of the superconducting domains between homologue or different bands there can be Josephson currents with positive or negative sign. Consequently, there is an overall tendency to cancel out the total supercurrent. Since the configurations (b) and (c) are approximately degenerate in energy, it is plausible to expect a suppression of the overall supercurrent especially when considering inhomogeneous (e.g. polycrystalline) superconducting films.

In this framework, the electric field affects only the (first two) surface layers, where it 'twists' the electronic states, inducing an intra-, and inter-layer mixing of the orbitals. This effect is described via two parameters: the strength of the orbital Rashba interaction α_{OR} induced at the surface layer, and the inter layer orbital mixing λ between the first and the second layer. The induced orbital polarization at the surface is associated with an orbital configuration that has non-vanishing angular momenta, which tends to reduce the superconducting order parameter.

The intra-layer processes such as λ and the usual electron hopping $t_\perp$ propagate the effect into the inner layers of the superconducting film. Furthermore, the symmetry breaking of the orbital processes induced by λ, can lead to an orbital specific phase of the superconducting order parameters, i.e., it can lead to a phase difference of π between the different electronic bands.

Three different regimes are identified, depending on the strength of α_{OR} and λ. If λ is small (relative to the inter-layer electron hopping energy t), the superconductor will be in the trivial superconducting state, regardless of the strength of α_{OR}. If both are sufficiently large, superconductivity is completely suppressed and the thin film becomes normal. The transition from the trivial to the normal phase seems to be continues, affects all three orbitals simultaneously, and has weak precursors.

A third, more interesting phase occurs when λ is large, yet α_{OR} is small. In this so called π-phase one of the three bands has a superconducting phase with a sign opposite to the others. The transition from the trivial phase to the π-phase is of first order. Such an unconventional phase state is expected to manifest itself in a non-standard current-phase relation. Inter-orbital scattering between the different bands as a consequence of disorder, is expected to result in an overall suppression of the superconducting state, that ultimately results in a transition to a normal state.

Before superconductivity is completely suppressed, inter-band π-phase slips between different regions in the π-phase can account for a suppression of the supercurrent, due to a cancellation between positive and negative pair currents among the various bands that are present at the Fermi level. This mechanism is illustrated in Fig. 7.6. In this scenario it is assumed that domains with different states are formed in the superconducting film, due to the an inhomogeneous distribution of the electric field on the surface, and due to the intrinsic polycrystalline character of the investigated materials.

There is a link between the obtained phase transitions and the electron itinerancy of the film, and thus its thickness. As many of the arguments and outcomes derive from symmetry arguments, a similar model can also be constructed for $p-$orbitals, as well as for $sp-$ or $pd-$hybridized systems, suggesting that the theory has a wide applicability. In the following section the theory is extended to also take into account the effects of an in-plane magnetic field. For more details regarding the original model see Refs. [204],

[III].

7.4 Microscopic theory, extension

In conjunction with the experimental efforts reported above, the microscopic model has been extended to include the effects of an in-plane magnetic field.

Assumptions

Like before, conventional BCS s-wave spin-singlet pairing and a multi-layered geometry with n_z layers is assumed. The electric field appears as a source of inversion symmetry breaking, introducing an orbital Rashba (OR) coupling for the intra-layer and inversion asymmetric inter-layer electronic processes. Due to screening effects, this process is limited to the surface layers. Thus, the electric field determines the strength of the inversion symmetry breaking interactions at the surface, and creates an electronic coupling that induces an orbital polarization at the Fermi level, that would not exist in an inversion symmetric environment. For our purposes the two key points are the surface layer OR coupling, indicated as α_{OR}, and the surface inter-layer inversion asymmetric interaction λ, which are the electronic parameters by which the electric field influences the superconducting (SC) state.

On the surface the electric field E_s is parallel to $\hat{z}$, and is thus described by a potential $V_s = -E_s z$. Following the standard approach, the surface orbital Rashba coupling is derived [216–218]. The matrix elements of V_s lead to an intra- (α_{OR}) and inter-layer (λ) inversion asymmetric interactions (in the Bloch basis), whose amplitude is proportional to E_s while the relative ratio depends on the inter-atomic distances and distortions at the surface (see Appendix A of Ref. [III] for details). Orbital polarization driven by an external electric field can play an important role in materials with p- or d-orbitals at each atomic site. Aluminium is included in the proposed modelling because its p-bands contribute to the electronic states at its the Fermi level.

In the model the pairing strength g is not modified by the electric field. This is physically consistent with the fact that due to screening effects the electric field cannot induce an inversion asymmetric potential inside the thin film beyond the Thomas-Fermi length. After formulating a tight binding model, the study is conducted by determining the superconducting order parameters (OPs) that correspond to the free energy minimum. $t_{||} = t$ denotes the planar hopping energy, while the interlayer hopping is orbital independent, i.e., $t_{\perp,\alpha} = t_\perp$, and the pairing coupling is $g = 2\,t$. Variations of the pairing coupling strength do not qualitatively alter the phase diagram.

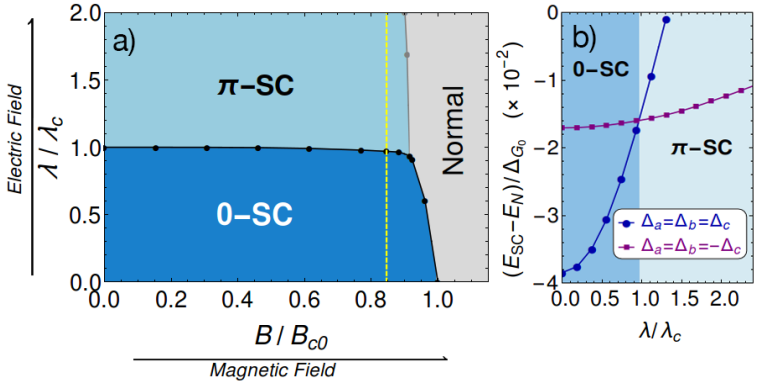

Figure 7.7: a) Phase diagram in the (B, λ) plane corresponding to an applied Zeeman field (B_Y) and an effective electric field for an orbital Rashba coupling $\alpha_{OR} = 0.2\,t$. We have three different phases: conventional superconducting state (0-SC), unconventional π-phase (π-SC), and normal metallic state (Normal). The transition line is obtained by comparing the free energy of the two states. B_{c0} is the critical field at $\alpha_{OR} = \lambda = 0$. The critical λ amplitude (or effective electric field) for the 0-π transition does not change as a function of the applied magnetic field B, except close to the critical field B_{c0}. b) Comparison of the minima of the free energy corresponding to the profiles in shown in 7.8 for the 0 and π phase, respectively.

Results

Without considering the magnetic field, the coupling λ can drive transitions of the type 0-π (i.e. conventional to unconventional superconductivity) or superconducting-normal depending on whether the α_{OR} is smaller or comparable to the planar kinetic energy scale set by the hopping amplitude t. Here, the term π-phase is used for the phase in which one of the bands contributing to the pairing at the Fermi level has a SC order parameter with opposite sign compared to those of the other bands. This is distinct from the 0-phase, where there is no phase difference among the bands. Within the model, a minimal set of three bands (i.e., a, b, c) is sufficient to simulate OR effects. In the π-phase we thus have that $\Delta_a = \Delta_b = -\Delta_c$.

The most important conclusion that comes from the microscopic model is that the electric field can break the inter-orbital phase rigidity before fully suppressing the amplitude of the order parameter. This is a result of the field breaking inversion-symmetry at the surface layers, by polarizing the orbitals of the electronic states at the Fermi level. The electric field has two main effects on the superconducting state. It rearranges the orbital dependent superconducting phases, introducing a phase difference of π between different bands (the π-phase), and it suppresses the amplitude of the order parameter by increasing the population of depaired orbitally

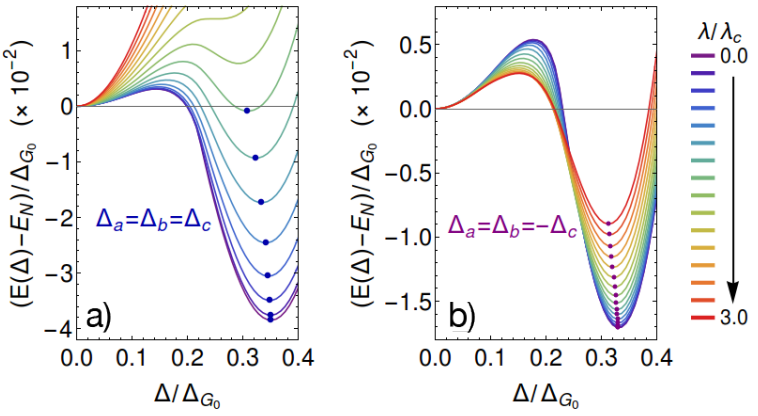

Figure 7.8: a) Behaviour of the free-energy as a function of the SC-order parameter Δ for the conventional and b) unconventional superconducting phases. Δ_{G_0} is the energy gap when $\alpha_{OR} = \lambda = 0$ and $B_Y = 0$. The free energy is shown for several values of λ, ranging from 0 to 3 λ_C, for a fixed value of the magnetic field which is marked by the yellow line in the panel a) of Fig. 7.7. The dots indicate the free energy minima. Other parameters: $n_z = 6$ (number of layers); $t_\perp = 1.5t, \mu = -0.4t, \eta = 0.1$ (see [III] SM).

polarized quasi-particles (the electric field driven normal phase). Both phases feature a vanishing supercurrent. However, the underlying mechanisms that leads to the supercurrent suppression is fundamentally different. In the π-phase the vanishing supercurrent is a result of frustration of the phase of the superconducting order parameter that originates from orbital effects, while in the electrically induced normal phase it is due to the suppression of the pairing order parameter. As an external in-plane magnetic field ideally affects only the order parameter, these two scenarios can be distinguished by the response of the critical voltage to an external in-plane magnetic field.

We start by considering a representative case with $\alpha_{OR} = 0.2\ t$ at zero temperature (Fig. 7.7). For $B_Y = 0$ the superconductor undergoes a 0-π transition above a critical λ which mimics the effect of the applied electric field. As expected, when considering a Zeeman field B_Y, the superconductor transitions into a normal state if B_Y exceeds a critical field B_Y^C. This SC-Normal transition is also obtained in the presence of a non-vanishing λ. Interestingly, both the 0-π phase boundary and the critical lines separating the 0- or π-phases from the normal state show only a weak interplay between the electric and magnetic fields (Fig. 7.7a). In fact, λ_C does not exhibit significant changes as a function of the magnetic field B_Y, except for close to the transition point. A similar behaviour is also observed for B_Y^C.

The phase diagram of Fig. 7.7 is determined by evaluating the behaviour of the free energy at a given magnetic field for the 0 and π phases, as shown

in Fig. 7.8a and b. While the free energy minimum of the 0-phase is strongly affected by the electric field, via λ, the π-phase is more resilient and at $\lambda \sim \lambda_C$ there is a transition from 0- to π-phase due to the crossing of the corresponding free energies (Fig. 7.7b). This transition is starkly unaffected by the magnetic field B_Y and it varies only close to the critical point where both 0- and π phases can be brought into the normal state. The weak dependence of λ_C on the magnetic field can be ascribed to the π-phase, in which the relative phases of the band-dependent SC order parameters have been rearranged, while their order parameter amplitudes are not significantly effected.

Now, we can try to compare the dependence of B_Y^C on V_{Gate} reported in Fig. 7.5b with the calculated phase diagram shown in Fig. 7.7a. We observe that in Fig. 7.7a the critical magnetic field B_C, which determines the boundary between the 0- or π-phase and the normal state, is practically unaffected by the variation of the electric field. This outcome is consistent with the behaviour of B_Y^C found experimentally (Fig. 7.5b) that remains unchanged until very close to the critical voltage, even though the I_C is already reduced before. We thus argue that the π-phase is induced by the electric field before reaching the critical voltage, to account for the preceding decrease of the supercurrent. Within the π-phase the supercurrent suppression is first driven by the inter-band phase sign frustration and later further amplified by the reduction of the amplitude of the superconducting order parameter. On the other hand, the rapid decrease of the critical magnetic field close to the critical voltage can be attributed to the occurrence of a normal state configuration. In this regime, we expect that the magnetic field phenomenology can be captured by the character of the 0-normal phase transition.

When considering the transition from the 0-SC to N state by varying the electric field amplitude (λ) at a larger value of the α_{OR}, one finds a stronger correlation between the critical electric field and the magnetic field, see Fig. 7.9 and Fig. 7.10.

In order to assess the role of the thermal fluctuations we have also determined the phase diagram at finite temperature for the case of a small orbital Rashba coupling. In Fig. 7.11 we report the phase diagram with the evolution of the transition lines among the 0-, π-SC phases and the normal metallic state by considering the effects of the temperature and of the effective electric field through the λ coupling. We compare the zero magnetic field case with one representative configuration corresponding to $B_Y \sim 0.6 B_Y^C$. There are two relevant observations to highlight: firstly, the critical boundary from the 0-SC state to the π-phase is practically unaffected by the temperature and by the applied magnetic field. Secondly, the critical temperature of the superconducting-normal transition is also independent on the 0- or π-character of the superconducting phase, as is observed experimentally. The evolution of the superconducting order

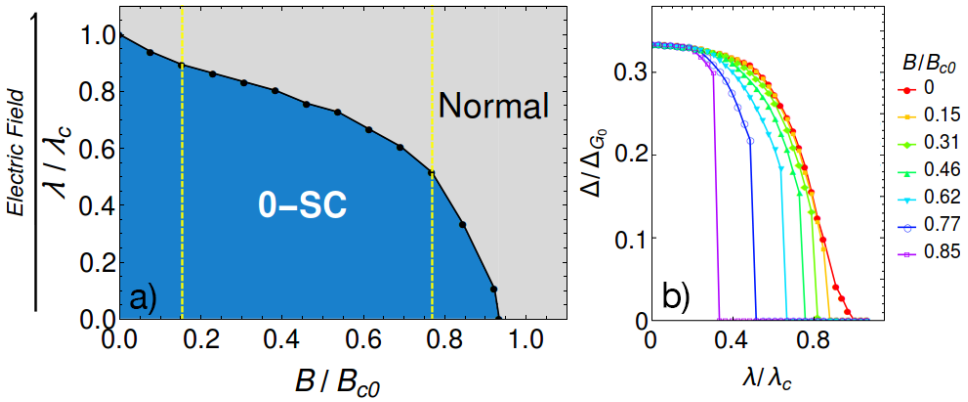

Figure 7.9: a) Phase diagram in the (B, λ) plane for $\alpha_{OR} = 1.0t$ assuming an in-plane magnetic field (B_Y). For this value of α_{OR}, there is no stable π-SC state as the π-SC free-energy is larger than that of the normal phase. B_{c0} is the critical field when $\alpha_{OR} = \lambda = 0$ and the other parameters are: $n_z = 6$ (number of layers); $t_\perp = 1.5t, \mu = -0.4t, \eta = 0.1$. b) Behaviour of the SC order parameter Δ as a function of λ for various values of the in-plane magnetic fields strength.

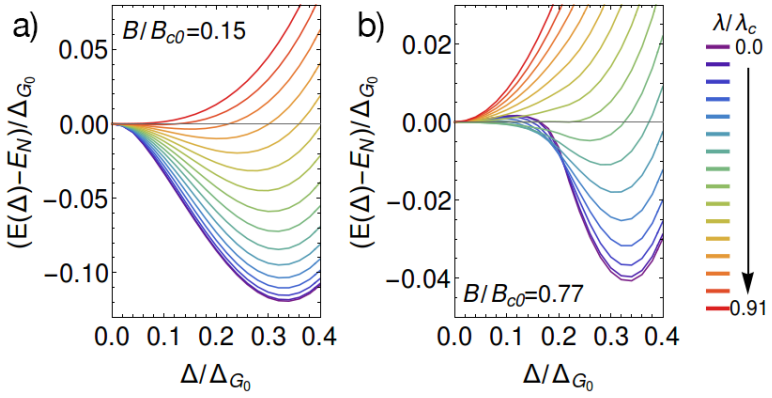

Figure 7.10: a), b) Behaviour of the free-energy as function of the SC-order parameter Δ for two different values of the magnetic field B_Y, indicated by the yellow lines in Fig. 7.9a. Δ_{G_0} is the energy gap when $\alpha_{OR} = \lambda = 0$ and $B = 0$. The free energy is shown for several values of λ, ranging from 0 to $\sim 0.9\lambda_c$ ($\lambda_c \simeq 0.33t$).

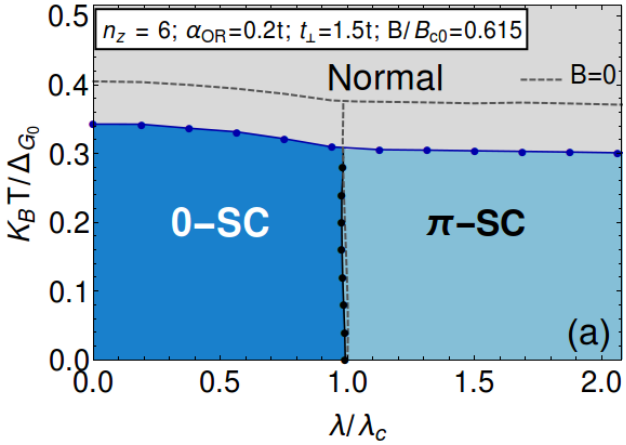

Figure 7.11: Phase diagram in the (λ, T) plane showing three different states: conventional superconducting state (0-SC), unconventional (π-SC), and normal state for $\alpha_{OR} = 0.2t$ for $B = 0.615 B_{c0}$. We assume an in-plane magnetic field orientation, e.g. B_Y. The critical λ amplitude for the 0-π transition (black line) does not change as a function of temperature. The transition from the SC to normal state (blue line) is of second order. The grey dashed lines are the transition lines in absence of magnetic field ($B = 0$).

parameters in temperature demonstrates a conventional trend with a weak dependence on the electric (via λ) and magnetic (B_Y) fields, as explicitly reported in Fig. 7.12.

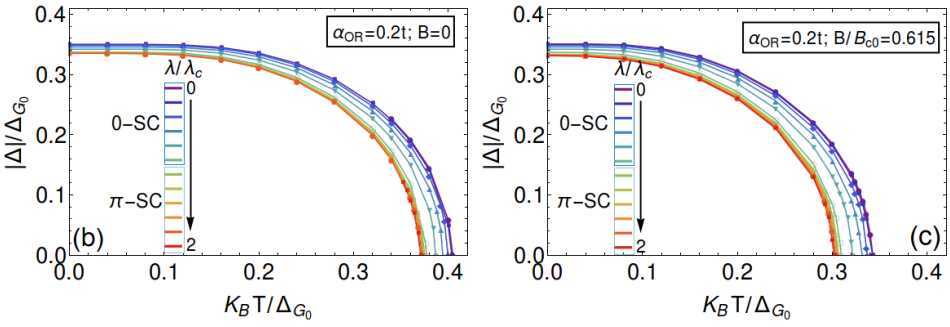

Figure 7.12: a) Behaviour of the order parameter as a function of temperature for $B = 0$ and b) $B \neq 0$, for several values of λ.

7.5 Summary and conclusions

Comparing the above theoretical results with the experimental observations we argue that the experimental outcome supports the existence of a π-phase in order to account for the magnetic field response of the SC nano-bridges in the presence of a strong electrostatic field. We note that in the π-phase, the presence of inter-band π-phase slips can naturally account for a suppression of the supercurrent, due to a cancellation between positive and negative pair currents among the various bands that are present at the Fermi level.

In Fig. 7.6 this scenario has been illustrated, assuming that domains with different phases are formed in the superconducting film, due to the expected inhomogeneous distribution of the electric field on the surface and due to the intrinsic polycrystalline character of the investigated materials. Thus, it is plausible to expect that an inhomogeneous phase with 0-π (small electric fields) and π-π interfaces (intermediate electric fields) is created, before the electric field is so strong that the superconductor becomes normal. Moreover, since the π-phase does not exhibit spatial modulations or gradients of the superconducting order parameter, we also expect a weak influence from the formation of a vortex phase, as induced by the out of plane magnetic field B_Z. Which is consistent with the experimental results. This is in line with the observation that the electric field can disrupt the superconducting state by inducing π-phase slips between the electronic states that contribute to the pairing at the Fermi level. This is also consistent with the enhancement of non-thermal phase fluctuations that have been observed in the switching current distributions of Ti Dayem bridges. [168]

In conclusion, we have investigated the suppression of supercurrent effected by the electric field, combined with and in-plane, or out-of-plane magnetic field, and ascertained that the two are weakly coupled. The critical magnetic fields are only affected for gate voltages close to the critical gate voltage. These findings are consistent with a microscopic model based on a multiband description of the superconducting state where the electric field is

assumed to induce an electrostatic interaction at the surface and in turn a strong orbital polarization at the Fermi level. The effect of a magnetic field on the electrically driven phase transitions has been thoroughly explored and the way the electric and magnetic fields can affect the superconductivity in thin films has been set out clearly. Furthermore, we have, for the first time, realized a complete suppression of the critical current in an aluminium-based Dayem bridge via electrostatic gating. Since aluminium is an important material from the technological point of view, this paves the way for future applications of gate-controlled superconductivity.

For completeness, it is also valuable to comment on recent results showing an increase of quasi-particle population induced by gate effects on superconducting nanowires [171]. Our proposed model, although completely different in microscopic structure and nature in comparison to the high-energy injection scenario, is however compatible with the increase of the quasi-particle population and the modification of the in-gap spectral weight. In fact, in both the 0-phase and in particular in the π-phase (due to the sign frustration of the superconducting order parameters) the electric field is able to induce a variation of the in-gap quasi-particles through the orbital polarization effect.

Chapter 8

Conclusion

In this thesis, two systems involving confined superconductivity have been presented. In the first part, we considered the TSQUIPT, a device that combines superconductivity with a 2D topological insulator.

Due to the combination of the localized nature of the topological edge states, and screening currents induced in the superconducting leads by a magnetic field, the density of states of the edge channels can be modified by exposing the device to small magnetic fields. The superconductor induces superconducting correlations and a gap in the density of states of the topological edge channels. Screening currents, that appear in the superconducting leads in response to a small magnetic field, shift the two spin density of states in energy via a Doppler shift-like effect. This effect can be detected and exploited in the TSQUIPT, which can function as a sensitive magnetometer.

By shifting the density of states, the induced superconducting gap can effectively be closed completely. This has dramatic consequences, for both the electronic transport transport through the edge channels, as well as for the thermal transport. Notably, the TSQUIPT functions as a thermal rectifier as well, for it permits the conduction of heat much more readily in one direction than in the other, and markedly outperforms superconductor-insulator-normal metal rectifiers. Structures based on topological superconductivity are a possible candidate for quantum computing, and in such a scenario, the management of heat and the associated decoherence is of paramount importance. A structure such as the TSQUIPT might be integrated in topological architectures, as it offers a fine control over electronic heat flow.

The second type of systems that have been treated, are nano-constrictions made of elementary, thin film superconductors exposed to a strong electric field. The recent discovery that electric fields affect such structures at all came as a great surprise, since it was long believed that their impact should be negligible.

While gate-controlled superconductivity has been observed in a substantial amount of experiments, there is still, as of the writing of this thesis, an

ongoing debate around the mechanism behind the effect. In particular, an attempt was made to answer the question of whether or not the effect can be understood as heating by the injection of electrons that are emitted from the gate via Fowler-Nordheim emission. To this end, an overview of all the current arguments for and against has been given. To rule out any possible quasi-particle injection, results of an experiment where niobium devices were gated using an ionic liquid, have also been presented.

To move beyond a trivial understanding, measurements of gate-controlled superconductivity in conjunction with magnetic fields have been reported as well. As in-, and out-of-plane magnetic fields affect thin, superconducting films in distinct ways, they can reveal important information regarding the action of the gate on e.g. the superconducting pairing strength.

In conjunction with the experimental efforts, a recently proposed microscopic theory was extended to take into account the effect of the in-plane magnetic field as well. The theoretical results are in agreement with the experimental observations, an encouraging sign. To fully understand the effect however, more experimental and theoretical efforts will be needed. For example, it would be interesting to see which role the device's dimension plays exactly. Even more interesting would be to investigate whether or not the effect is the same when single-crystal films are gated, instead of the multi-crystalline films used to far. Since film inhomogeneity due to the presence of many superconducting domains plays a role in the mechanism suggested in the preceding chapter, it is something that should be explored in order to test our current understanding. If for example, the gate-induced suppression of the supercurrent would be absent, that would be a definite blow to theory.

While the effect remains surrounded by many questions, it is not hard to foresee it applied in the near future. Regardless of the underlying mechanism, the prospect of super fast, ultra efficient, superconducting transistors is an attractive one. Especially since superconducting architectures play an important role in many emerging solid state quantum technologies. In fact, a great variation of possible (logic) devices that can be made exploiting the effect has already been proposed.

Thus, it seems only a matter of a short time before the gated superconducting transistors find an application. Less clear is, whether the effect will be fully understood by then. Looking back at the history, one counts near fifty years between the discovery of superconductivity, and the seminal BCS theory that describes the underlying mechanism. So, it could take a while yet...

Appendix A

Nanofabrication and experimental setup

The devices described in this thesis were fabricated in the cleanroom facility of the NEST laboratory, employing standard nanofabrication techniques. A brief overview of used methods is presented, as well as details of the experimental setup.

A.1 Device fabrication

The workhorse of modern nanofabrication, at the least in the academic world, is Electron Beam Lithography (EBL). First, a thin layer of PMMA (polymethyl methacrylate, AR-P 679.04) polymer resist is spincoated on a substrate at 4000 RPM for 1 minute. Hereafter the PMMA is baked for 1 minute at 160 degrees Celsius. Depending on the experiment, the substrate can be either SiO_2 or sapphire. The coating results in an even layer of resist that covers the substrate, ~ 200 nm thick.

When using sapphire as a substrate, a significant amount of charge builds up during the exposure, which distorts and deflects the beam. This leads to the loss or resolution and, in the worst cases, can lead to significant distortions of the designed pattern. To counteract this charging, the PMMA is covered with a thin layer of the conductive liquid, commonly known as *Electra* (AR-PC 5090). The liquid is spincoated on top of the PMMA layer at 4000 RPM for one minute, followed by a 2 minute baking at 120 degrees Celsius.

The sample is then placed in an EBL machine, that features a high vacuum chamber in which a beam of electrons is used to expose arbitrary patterns polymer resist. The technique offers a great freedom on the shape and size of the patterned masks. The typical minimal resolution reached is around ~ 30 nm. After the exposure, the conductive liquid is removed using demineralized water (if applicable), and the sample is developed in *Ar*

600-56 for 1.5 minutes, removing the exposed parts of the polymer layer, such that the substrate surface is exposed in the desired pattern.

Once the resist is developed the sample is transferred to another machine in order to deposit a thin film of one or more metals. Depending on the desired material, this is done in via evaporation or via sputtering.

Metals such as aluminium, titanium, vanadium, copper and aluminium-manganese can be deposited in the high vacuum electron beam evaporator, that has a base pressure of $\sim 10^{-11}$ torr. Using an electron beam, a crucible containing the target metal is heated until the material evaporates and covers the entire sample in a thin layer of metal. If desired, several materials can be deposited on top of each other. When the desired thickness and composition is reached, the sample is removed from the vacuum chamber and placed into acetone. The acetone dissolves the remaining PMMA, which lifts off the metal that was deposited on top, leaving behind only the material that has been deposited in the exposed regions.

Post evaporation

After the evaporation, the quality of the device can be checked using Scanning Electron Microscopy (SEM). If the result is satisfactory, the sample is glued to a 24 pin dual in-line sample holder. Via an ultrasonic wire bonder, thin aluminium wires are connected to the pads on the sample and pads on the sample holder, electrically connecting the device to the sample holder. The sample holder can then be placed on the cold finger of the cryostats, at which point it is ready to be measured.

A.2 Aluminium Dayem bridges

The Aluminium Dayem bridges, discussed in chapter 7, were fabricated by using single step electron beam lithography to pattern a resist mask on a sapphire substrate. Titanium and aluminium were evaporated at room temperature in an electron beam evaporator with a base pressure of 10^{-11} Torr. 3 nm of titanium was deposited at 1 Å/s (to improve adhesion), after which 14 nm of aluminium was deposited at 2.5 Å/s. The Dayem bridges are approximately 120 nm wide, 100 nm long, and have a normal-state resistance $R_{\mathrm{N}} \approx 25\,\Omega$. Gate-bridge separation is approximately 30 nm, and the leads on either side of the bridge are 2 μm wide, see figure 7.1. Resistance versus temperature measurements, performed using a 3 μV square wave excitation indicate a critical temperature $T_C \approx 600$ mK, and a transition width of $\approx$ 60 mK.

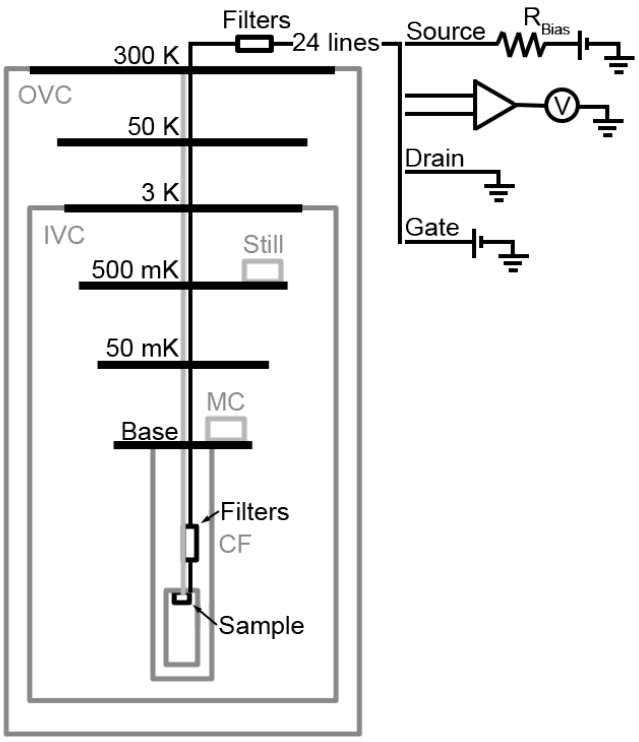

Figure A.1: A schematic representation of the dilution refrigerator and a typical four wire measurement setup. Abbreviations stand for: Outer Vacuum Shield (OVC), Inner Vacuum Shield (IVC), Mixing Chamber (MC), and Cold Finger (CF). For details regarding the filters and instruments see the main text.

A.3 Niobium Dayem bridges

The Niobium Dayem bridges, discussed in chapter 6, were fabricated via single step electron beam lithography and sputtering, on a sapphire substrate. After patterning the resist, a ≈ 10 nm thick sticking layer of Ti was deposited via sputtering, followed by a ≈ 50 nm thick layer of Niobium. After sputtering the excess metal is removed via lift-off and mild sonification. The bridge dimensions are similar to before: approximately 120 nm wide and 100 nm long. The critical temperature of the Niobium devices is typically between 6 and 8 K. This is slightly below the bulk value of 9.2 K, likely due to a minor inverse proximity effect from the titanium sticking layer.

A.4 Experimental set-up

The experiments presented in chapter 6 have been done at the department of physics laboratories of the university of Pisa, in an *Optistat Dry BLV* cryostat from *Oxford Instruments*. It is a dry cryostat that has a base temperature of ≈ 2.36 K. It features 20 DC lines that are outfitted with LC and RF filters. A major advantage of this cryostat is that it needs a mere 3 hours to reach base temperature from room temperature.

All the experiments described in chapter 7 have been performed at the NEST laboratory, in a either a *Leiden Cryogenics*, or an *Oxford Instruments* cryo-free dilution refrigerator. The *Leiden Cryogenics* cryostat, is the CF-CS81, CF-1400 Maglev model. The *Oxford Instruments* cryostat is of the type Triton 300. Both have a base temperature < 10 mK.

The DC lines that connect the external room-temperature instruments with the dual-in-line sample holder are fitted with double stage low-pass RC filters ($R = 1.2$ kΩ, $C = 10$ nF) and a pair of *Oxley red* π-filters (1500 pF), one in the breaking box and one on the cold finger. See also Fig. A.1 for a schematic illustration of the cryotstat.

In the *Leiden* refrigerator, the sample holder is situated at the centre of an *American Magnetics* superconducting vectorial magnet, that can reach fields of 1 Tesla in the X and Y directions, and 5 Tesla in the Z direction. The cryostat temperature, magnetic field and other measurement instruments are controlled via a custom made LabVIEW program.

After fabrications, the samples are glued to a standard, C-DIP 24 pin dual in-line sample holder, and connected to it using a wire bonder. The sample holder can then be mounted on the cold finger. To reduce noise, the sample is shielded by two close fitting brass cylinders, which are mounted to the cold finger.

Measurement techniques

The results presented in chapters 6 and 7 have been collected using standard measurement techniques. The critical current I_C is determined via IV measurements performed in a four wire configuration. The junction was current biased, typically with a *Yokogawa GS200* voltage source over a large ($10^5 - 10^7$ Ω) resistance. The voltage drop over the superconducting junction was measured using a room temperature *DL instruments 1201* voltage pre-amplifier –operated in battery mode– and a multimeter such as the *Agilent 34410*.

For the ionic liquid experiment, the liquid was polarized with a *Keithley 2400* voltage source, at 200+ K temperatures. The polarising current, which decays exponentially, was measured as a control. The ionic gate voltage source was typically left on during the entire measurement, but some of the measurements have been repeated with the voltage source disconnected with

the same results.

For the magnetic field measurements, the gate voltage was also supplied by a low noise sourcemeter, such as the *Keithley 2400*. To determine the critical current I_C, current-voltage $I-V$ measurements were repeated 30 to 50 times. During data analysis the I_C is detected using *Mathematica* software specifically written for this task. The results of this program have been manually checked to make sure they are correct.

Leakage current measurements

The leakage current between the gate and device was carefully measured by applying a voltage to the gate in the usual manner, and amplifying the current flowing into the device using a room temperature current amplifier over a long period of time, while all the other lines are left floating. The *DL instruments 1211* current amplifier –operated in battery mode– was used with a sensitivity around $10^6 - 10^7$ V/A, which corresponds to an output resistance of 0.2 - 2 kΩ, to convert the current into a voltage signal. Finally, the current amplifier output is measured by a multimeter such as the *Agilent 34410*.

Bibliography

[1] J. Clarke and A. I. Braginski, *The SQUID Handbook: Fundamentals and Technology of SQUIDs and SQUID Systems, Vol. 1.* Wiley-VCH Publication, Weinheim, 2004.

[2] R. N. Jabdaraghi, M. Meschke, and J. P. Pekola, "Non-hysteretic superconducting quantum interference proximity transistor with enhanced responsivity," *Applied Physics Letters*, vol. 104, no. 8, p. 082601, 2014.

[3] A. Ronzani, C. Altimiras, and F. Giazotto, "Highly sensitive superconducting quantum-interference proximity transistor," *Phys. Rev. Applied*, vol. 2, p. 024005, Aug 2014.

[4] S. D'Ambrosio, M. Meissner, C. Blanc, A. Ronzani, and F. Giazotto, "Normal metal tunnel junction-based superconducting quantum interference proximity transistor," *Applied Physics Letters*, vol. 107, no. 11, p. 113110, 2015.

[5] M. Z. Hasan and C. L. Kane, "Colloquium: Topological insulators," *Reviews of Modern Physics*, vol. 82, pp. 3045–3067, Nov. 2010.

[6] X.-L. Qi and S.-C. Zhang, "Topological insulators and superconductors," *Reviews of Modern Physics*, vol. 83, pp. 1057–1110, Oct. 2011.

[7] M. Z. Hasan and J. E. Moore, "Three-dimensional topological insulators," *Annual Review of Condensed Matter Physics*, vol. 2, no. 1, pp. 55–78, 2011.

[8] Y. Ando, "Topological insulator materials," *Journal of the Physical Society of Japan*, vol. 82, no. 10, p. 102001, 2013.

[9] G. Tkachov and E. M. Hankiewicz, "Spin-helical transport in normal and superconducting topological insulators," *Phys. Status Solidi Basic Res.*, vol. 250, no. 2, pp. 215–232, 2013.

[10] O. Pankratov, S. Pakhomov, and B. Volkov, "Supersymmetry in heterojunctions: Band-inverting contact on the basis of pb1/xSnxTe and hg1/xCdxTe," *Solid State Communications*, vol. 61, pp. 93–96, Jan. 1987.

[11] C. L. Kane and E. J. Mele, "Quantum spin hall effect in graphene," *Physical Review Letters*, vol. 95, Nov. 2005.

[12] C. L. Kane and E. J. Mele, "Z2topological order and the quantum spin hall effect," *Physical Review Letters*, vol. 95, Sept. 2005.

[13] B. A. Bernevig and S.-C. Zhang, "Quantum spin hall effect," *Physical Review Letters*, vol. 96, Mar. 2006.

[14] B. A. Bernevig, T. L. Hughes, and S.-C. Zhang, "Quantum spin hall effect and topological phase transition in HgTe quantum wells," *Science*, vol. 314, pp. 1757–1761, Dec. 2006.

[15] J. E. Moore and L. Balents, "Topological invariants of time-reversal-invariant band structures," *Physical Review B*, vol. 75, Mar. 2007.

[16] L. Fu, C. L. Kane, and E. J. Mele, "Topological insulators in three dimensions," *Physical Review Letters*, vol. 98, Mar. 2007.

[17] C. Liu, T. L. Hughes, X.-L. Qi, K. Wang, and S.-C. Zhang, "Quantum spin hall effect in inverted type-II semiconductors," *Physical Review Letters*, vol. 100, June 2008.

[18] R. Roy, "Topological phases and the quantum spin hall effect in three dimensions," *Physical Review B*, vol. 79, May 2009.

[19] M. König, S. Wiedmann, C. Brüne, A. Roth, H. Buhmann, L. W. Molenkamp, X.-l. Qi, and S.-c. Zhang, "Quantum Spin Hall Insulator State in HgTe Quantum Wells," *Science*, vol. 318, no. November, pp. 766–771, 2007.

[20] D. Hsieh, D. Qian, L. Wray, Y. Xia, Y. S. Hor, R. J. Cava, and M. Z. Hasan, "A topological dirac insulator in a quantum spin hall phase," *Nature*, vol. 452, pp. 970–974, Apr. 2008.

[21] Y. Xia, D. Qian, D. Hsieh, L. Wray, A. Pal, H. Lin, A. Bansil, D. Grauer, Y. S. Hor, R. J. Cava, and M. Z. Hasan, "Observation of a large-gap topological-insulator class with a single dirac cone on the surface," *Nature Physics*, vol. 5, pp. 398–402, May 2009.

[22] A. Roth, C. Brüne, H. Buhmann, L. W. Molenkamp, J. Maciejko, X.-L. Qi, and S.-C. Zhang, "Nonlocal transport in the quantum spin Hall state.," *Science*, vol. 325, no. 5938, pp. 294–297, 2009.

[23] C. Brüne, A. Roth, E. G. Novik, M. König, H. Buhmann, E. M. Hankiewicz, W. Hanke, J. Sinova, and L. W. Molenkamp, "Evidence for the ballistic intrinsic spin hall effect in HgTe nanostructures," *Nature Physics*, vol. 6, pp. 448–454, May 2010.

[24] C. Brüne, A. Roth, H. Buhmann, E. M. Hankiewicz, L. W. Molenkamp, J. Maciejko, X.-L. Qi, and S.-C. Zhang, "Spin polarization of the quantum spin Hall edge states," *Nat. Phys.*, vol. 8, no. 6, pp. 486–491, 2012.

[25] K. C. Nowack, E. M. Spanton, M. Baenninger, M. König, J. R. Kirtley, B. Kalisky, C. Ames, P. Leubner, C. Brüne, H. Buhmann, L. W. Molenkamp, D. Goldhaber-Gordon, and K. A. Moler, "Imaging currents in HgTe quantum wells in the quantum spin Hall regime," *Nat. Mater.*, vol. 12, no. 9, pp. 787–791, 2013.

[26] M. König, M. Baenninger, A. G. F. Garcia, N. Harjee, B. L. Pruitt, C. Ames, P. Leubner, C. Brüne, H. Buhmann, L. W. Molenkamp, and D. Goldhaber-Gordon, "Spatially resolved study of backscattering in the quantum spin hall state," *Physical Review X*, vol. 3, Apr. 2013.

[27] I. Knez, R.-R. Du, and G. Sullivan, "Evidence for helical edge modes in InvertedInAs/GaSbQuantum wells," *Physical Review Letters*, vol. 107, Sept. 2011.

[28] F. Nichele, A. N. Pal, P. Pietsch, T. Ihn, K. Ensslin, C. Charpentier, and W. Wegscheider, "Insulating state and giant nonlocal response in anInAs/GaSbQuantum well in the quantum hall regime," *Physical Review Letters*, vol. 112, Jan. 2014.

[29] I. Knez, C. T. Rettner, S.-H. Yang, S. S. Parkin, L. Du, R.-R. Du, and G. Sullivan, "Observation of edge transport in the disordered regime of topologically InsulatingInAs/GaSbQuantum wells," *Physical Review Letters*, vol. 112, Jan. 2014.

[30] F. Qu, A. J. Beukman, S. Nadj-Perge, M. Wimmer, B.-M. Nguyen, W. Yi, J. Thorp, M. Sokolich, A. A. Kiselev, M. J. Manfra, C. M. Marcus, and L. P. Kouwenhoven, "Electric and magnetic tuning between the trivial and topological phases in InAs/GaSb double quantum wells," *Physical Review Letters*, vol. 115, July 2015.

[31] T. Li, P. Wang, H. Fu, L. Du, K. A. Schreiber, X. Mu, X. Liu, G. Sullivan, G. A. Csáthy, X. Lin, and R.-R. Du, "Observation of a helical luttinger liquid inInAs/GaSbQuantum spin hall edges," *Physical Review Letters*, vol. 115, Sept. 2015.

[32] L. Du, I. Knez, G. Sullivan, and R.-R. Du, "Robust helical edge transport in GatedInAs/GaSbBilayers," *Physical Review Letters*, vol. 114, Mar. 2015.

[33] S. Mueller, A. N. Pal, M. Karalic, T. Tschirky, C. Charpentier, W. Wegscheider, K. Ensslin, and T. Ihn, "Nonlocal transport via

edge states in InAs/GaSb coupled quantum wells," *Physical Review B*, vol. 92, Aug. 2015.

[34] C. Wu, B. A. Bernevig, and S.-C. Zhang, "Helical liquid and the edge of quantum spin hall systems," *Physical Review Letters*, vol. 96, Mar. 2006.

[35] D. R. Schmidt, H.-M. Cho, J. Hubmayr, P. Lowell, M. D. Niemack, G. C. O'Neil, J. N. Ullom, K. W. Yoon, K. D. Irwin, W. L. Holzapfel, M. Lueker, E. M. George, and E. Shirokoff, "Al-mn transition edge sensors for cosmic microwave background polarimeters," *IEEE Transactions on Applied Superconductivity*, vol. 21, pp. 196–198, June 2011.

[36] F. Ronetti, L. Vannucci, G. Dolcetto, M. Carrega, and M. Sassetti, "Spin-thermoelectric transport induced by interactions and spin-flip processes in two-dimensional topological insulators," *Physical Review B*, vol. 93, Apr. 2016.

[37] A. Calzona, M. Acciai, M. Carrega, F. Cavaliere, and M. Sassetti, "Time-resolved energy dynamics after single electron injection into an interacting helical liquid," *Physical Review B*, vol. 94, July 2016.

[38] P. Delplace, J. Li, and M. Büttiker, "Magnetic-field-induced localization in 2d topological insulators," *Physical Review Letters*, vol. 109, Dec. 2012.

[39] J. M. Edge, J. Li, P. Delplace, and M. Büttiker, "Z2peak of noise correlations in a quantum spin hall insulator," *Physical Review Letters*, vol. 110, June 2013.

[40] J. I. Väyrynen, M. Goldstein, and L. I. Glazman, "Helical edge resistance introduced by charge puddles," *Physical Review Letters*, vol. 110, May 2013.

[41] S. Das and S. Rao, "Spin-polarized scanning-tunneling probe for helical luttinger liquids," *Physical Review Letters*, vol. 106, June 2011.

[42] R. Holm and W. Meissner, "Messungen mit hilfe von flüssigem helium. xiii," *Zeitschrift für Physik*, vol. 74, no. 11-12, pp. 715–735, 1932.

[43] H. Meissner, "Superconductivity of contacts with interposed barriers," *Physical Review*, vol. 117, pp. 672–680, Feb. 1960.

[44] J. Nicol, S. Shapiro, and P. H. Smith, "Direct measurement of the superconducting energy gap," *Physical Review Letters*, vol. 5, pp. 461–464, Nov. 1960.

[45] P. de Gennes and D. Saint-James, "Elementary excitations in the vicinity of a normal metal-superconducting metal contact," *Physics Letters*, vol. 4, pp. 151–152, Mar. 1963.

[46] G. E. Blonder, M. Tinkham, and T. M. Klapwijk, "Transition from metallic to tunneling regimes in superconducting microconstrictions: Excess current, charge imbalance, and supercurrent conversion," *Physical Review B*, vol. 25, pp. 4515–4532, Apr. 1982.

[47] K. D. Usadel, "Generalized diffusion equation for superconducting alloys," *Physical Review Letters*, vol. 25, pp. 507–509, Aug. 1970.

[48] F. Zhou, P. Charlat, B. Spivak, and B. Pannetier, "Density of states in superconductor-normal metal-superconductor junctions," *Journal of Low Temperature Physics*, vol. 110, no. 3/4, pp. 841–850, 1998.

[49] J. C. Hammer, J. C. Cuevas, F. S. Bergeret, and W. Belzig, "Density of states and supercurrent in diffusive SNS junctions: Roles of nonideal interfaces and spin-flip scattering," *Physical Review B*, vol. 76, Aug. 2007.

[50] H. le Sueur, P. Joyez, H. Pothier, C. Urbina, and D. Esteve, "Phase controlled superconducting proximity effect probed by tunneling spectroscopy," *Physical Review Letters*, vol. 100, May 2008.

[51] G. D. Guttman, B. Nathanson, E. Ben-Jacob, and D. J. Bergman, "Thermoelectric and thermophase effects in josephson junctions," *Physical Review B*, vol. 55, pp. 12691–12700, May 1997.

[52] A. V. Timofeev, C. P. García, N. B. Kopnin, A. M. Savin, M. Meschke, F. Giazotto, and J. P. Pekola, "Recombination-limited energy relaxation in a bardeen-cooper-schrieffer superconductor," *Physical Review Letters*, vol. 102, Jan. 2009.

[53] E. Strambini, F. S. Bergeret, and F. Giazotto, "Proximity nanovalve with large phase-tunable thermal conductance," *Applied Physics Letters*, vol. 105, p. 082601, Aug. 2014.

[54] H. Rabani, F. Taddei, O. Bourgeois, R. Fazio, and F. Giazotto, "Phase-dependent electronic specific heat of mesoscopic josephson junctions," *Physical Review B*, vol. 78, July 2008.

[55] H. Rabani, F. Taddei, F. Giazotto, and R. Fazio, "Influence of interface transmissivity and inelastic scattering on the electronic entropy and specific heat of diffusive superconductor-normal metal-superconductor josephson junctions," *Journal of Applied Physics*, vol. 105, p. 093904, May 2009.

[56] T. T. Heikkilä and F. Giazotto, "Phase sensitive electron-phonon coupling in a superconducting proximity structure," *Physical Review B*, vol. 79, Mar. 2009.

[57] F. Giazotto, J. T. Peltonen, M. Meschke, and J. P. Pekola, "SQUIPT - Superconducting Quantum Interference Proximity Transistor," *Nat. Phys.*, vol. 6, no. 4, pp. 254–259, 2010.

[58] L. Maier, J. B. Oostinga, D. Knott, C. Brüne, P. Virtanen, G. Tkachov, E. M. Hankiewicz, C. Gould, H. Buhmann, and L. W. Molenkamp, "Induced superconductivity in the three-dimensional topological insulator HgTe," *Physical Review Letters*, vol. 109, Nov. 2012.

[59] J. R. Williams, A. J. Bestwick, P. Gallagher, S. S. Hong, Y. Cui, A. S. Bleich, J. G. Analytis, I. R. Fisher, and D. Goldhaber-Gordon, "Unconventional josephson effect in hybrid superconductor-topological insulator devices," *Physical Review Letters*, vol. 109, July 2012.

[60] I. Knez, R.-R. Du, and G. Sullivan, "Andreev reflection of helical edge modes inInAs/GaSbQuantum spin hall insulator," *Physical Review Letters*, vol. 109, Oct. 2012.

[61] J. B. Oostinga, L. Maier, P. Schüffelgen, D. Knott, C. Ames, C. Brüne, G. Tkachov, H. Buhmann, and L. W. Molenkamp, "Josephson supercurrent through the topological surface states of strained bulk HgTe," *Physical Review X*, vol. 3, May 2013.

[62] A. Finck, C. Kurter, Y. Hor, and D. V. Harlingen, "Phase coherence and andreev reflection in topological insulator devices," *Physical Review X*, vol. 4, Nov. 2014.

[63] S. Hart, H. Ren, T. Wagner, P. Leubner, M. Mühlbauer, C. Brüne, H. Buhmann, L. W. Molenkamp, and A. Yacoby, "Induced superconductivity in the quantum spin Hall edge," *Nat. Phys.*, vol. 10, no. 9, pp. 638–643, 2014.

[64] V. S. Pribiag, A. J. A. Beukman, F. Qu, M. C. Cassidy, C. Charpentier, W. Wegscheider, and L. P. Kouwenhoven, "Edge-mode superconductivity in a two-dimensional topological insulator," *Nature Nanotechnology*, vol. 10, pp. 593–597, May 2015.

[65] L. Fu and C. L. Kane, "Superconducting proximity effect and majorana fermions at the surface of a topological insulator," *Physical Review Letters*, vol. 100, Mar. 2008.

[66] G. Tkachov and E. M. Hankiewicz, "Helical andreev bound states and superconducting klein tunneling in topological insulator josephson junctions," *Physical Review B*, vol. 88, Aug. 2013.

[67] L. Fu and C. L. Kane, "Josephson current and noise at a superconductor / quantum-spin-hall-insulator / superconductor junction," *Physical Review B*, vol. 79, Apr. 2009.

[68] D. M. Badiane, M. Houzet, and J. S. Meyer, "Nonequilibrium josephson effect through helical edge states," *Physical Review Letters*, vol. 107, Oct. 2011.

[69] C. W. J. Beenakker, D. I. Pikulin, T. Hyart, H. Schomerus, and J. P. Dahlhaus, "Fermion-parity anomaly of the critical supercurrent in the quantum spin-hall effect," *Physical Review Letters*, vol. 110, Jan. 2013.

[70] F. Crépin and B. Trauzettel, "Parity measurement in topological josephson junctions," *Physical Review Letters*, vol. 112, Feb. 2014.

[71] J. Wiedenmann, E. Bocquillon, R. S. Deacon, S. Hartinger, O. Herrmann, T. M. Klapwijk, L. Maier, C. Ames, C. Brüne, C. Gould, A. Oiwa, K. Ishibashi, S. Tarucha, H. Buhmann, and L. W. Molenkamp, "4π-periodic josephson supercurrent in HgTe-based topological josephson junctions," *Nature Communications*, vol. 7, Jan. 2016.

[72] E. Bocquillon, R. S. Deacon, J. Wiedenmann, P. Leubner, T. M. Klapwijk, C. Brüne, K. Ishibashi, H. Buhmann, and L. W. Molenkamp, "Gapless andreev bound states in the quantum spin hall insulator HgTe," *Nature Nanotechnology*, vol. 12, pp. 137–143, Aug. 2016.

[73] R. Deacon, J. Wiedenmann, E. Bocquillon, F. Domínguez, T. Klapwijk, P. Leubner, C. Brüne, E. Hankiewicz, S. Tarucha, K. Ishibashi, H. Buhmann, and L. Molenkamp, "Josephson radiation from gapless andreev bound states in HgTe-based topological junctions," *Physical Review X*, vol. 7, Apr. 2017.

[74] I. Sochnikov, L. Maier, C. A. Watson, J. R. Kirtley, C. Gould, G. Tkachov, E. M. Hankiewicz, C. Brüne, H. Buhmann, L. W. Molenkamp, and K. A. Moler, "Nonsinusoidal current-phase relationship in josephson junctions from the 3d topological insulator HgTe," *Physical Review Letters*, vol. 114, Feb. 2015.

[75] C. Kurter, A. Finck, Y. S. Hor, and D. J. V. Harlingen, "Evidence for an anomalous current–phase relation in topological insulator josephson junctions," *Nature Communications*, vol. 6, June 2015.

[76] B. Sothmann and E. M. Hankiewicz, "Fingerprint of topological andreev bound states in phase-dependent heat transport," *Physical Review B*, vol. 94, Aug. 2016.

[77] G. Tkachov, P. Burset, B. Trauzettel, and E. M. Hankiewicz, "Quantum interference of edge supercurrents in a two-dimensional topological insulator," *Phys. Rev. B*, vol. 92, p. 045408, Jul 2015.

[78] A. M. Black-Schaffer and J. Linder, "Magnetization dynamics and majorana fermions in ferromagnetic josephson junctions along the quantum spin hall edge," *Physical Review B*, vol. 83, June 2011.

[79] D. I. Pikulin, T. Hyart, S. Mi, J. Tworzydło, M. Wimmer, and C. W. J. Beenakker, "Disorder and magnetic-field-induced breakdown of helical edge conduction in an inverted electron-hole bilayer," *Phys. Rev. B*, vol. 89, p. 161403, Apr 2014.

[80] B. Sothmann, F. Giazotto, and E. M. Hankiewicz, "High-efficiency thermal switch based on topological josephson junctions," *New Journal of Physics*, vol. 19, no. 2, p. 023056, 2017.

[81] M. J. Martínez-Pérez, P. Solinas, and F. Giazotto, "Coherent caloritronics in josephson-based nanocircuits," *J. Low Temp. Phys.*, vol. 175, no. 5-6, pp. 813–837, 2014.

[82] B. Baxevanis, V. P. Ostroukh, and C. W. J. Beenakker, "Even-odd flux quanta effect in the fraunhofer oscillations of an edge-channel josephson junction," *Physical Review B*, vol. 91, Jan. 2015.

[83] M. Meschke, J. T. Peltonen, J. P. Pekola, and F. Giazotto, "Tunnel spectroscopy of a proximity josephson junction," *Phys. Rev. B*, vol. 84, p. 214514, Dec 2011.

[84] P. Virtanen, A. Ronzani, and F. Giazotto, "Spectral characteristics of a fully superconducting squipt," *Phys. Rev. Applied*, vol. 6, p. 054002, Nov 2016.

[85] E. Strambini, S. D'ambrosio, F. Vischi, F. S. Bergeret, Y. V. Nazarov, and F. Giazotto, "The ω-SQUIPT as a tool to phase-engineer Josephson topological materials," *Nat. Nano.*, vol. 11, no. 12, pp. 1055–1059, 2016.

[86] F. Vischi, M. Carrega, E. Strambini, S. D'Ambrosio, F. S. Bergeret, Y. V. Nazarov, and F. Giazotto, "Coherent transport properties of a three-terminal hybrid superconducting interferometer," *Phys. Rev. B*, vol. 95, p. 054504, Feb 2017.

[87] F. Giazotto and F. Taddei, "Hybrid superconducting quantum magnetometer," *Phys. Rev. B*, vol. 84, p. 214502, Dec 2011.

[88] A. Ronzani, S. D'Ambrosio, P. Virtanen, F. Giazotto, and C. Altimiras, "Phase-driven collapse of the cooper condensate in a nanosized superconductor," *Phys. Rev. B*, vol. 96, p. 214517, Dec 2017.

[89] N. Ligato, G. Marchegiani, P. Virtanen, E. Strambini, and F. Giazotto, "High operating temperature in V-based superconducting quantum interference proximity transistors," *Sci. Rep.*, vol. 7, no. 8810, pp. 1–9, 2017.

[90] E. Enrico, E. Strambini, and F. Giazotto, "Phase-driven charge manipulation in Hybrid Single-Electron Transistor," *Sci. Rep.*, vol. 7, no. 13492, pp. 1–7, 2017.

[91] E. Enrico and F. Giazotto, "Superconducting quantum interference single-electron transistor," *Phys. Rev. Applied*, vol. 5, p. 064020, Jun 2016.

[92] R. N. Jabdaraghi, D. S. Golubev, J. P. Pekola, and J. T. Peltonen, "Noise of a superconducting magnetic flux sensor based on a proximity Josephson junction," *Sci. Rep.*, vol. 7, no. 8011, pp. 1–11, 2017.

[93] R. N. Jabdaraghi, J. T. Peltonen, O.-P. Saira, and J. P. Pekola, "Low-temperature characterization of nb-cu-nb weak links with ar ion-cleaned interfaces," *Applied Physics Letters*, vol. 108, no. 4, p. 042604, 2016.

[94] B. Zhou, H.-Z. Lu, R.-L. Chu, S.-Q. Shen, and Q. Niu, "Finite size effects on helical edge states in a quantum spin-hall system," *Phys. Rev. Lett.*, vol. 101, p. 246807, Dec 2008.

[95] M. Wada, S. Murakami, F. Freimuth, and G. Bihlmayer, "Localized edge states in two-dimensional topological insulators: Ultrathin bi films," *Phys. Rev. B*, vol. 83, p. 121310, Mar 2011.

[96] G. Tkachov, "Suppression of surface p-wave superconductivity in disordered topological insulators," *Phys. Rev. B*, vol. 87, p. 245422, Jun 2013.

[97] C. W. J. Beenakker, "Universal limit of critical-current fluctuations in mesoscopic josephson junctions," *Phys. Rev. Lett.*, vol. 67, pp. 3836–3839, Dec 1991.

[98] J. Pearl, "Current distribution in superconducting films carrying quantized fluxoids," *Applied Physics Letters*, vol. 5, pp. 65–66, Aug. 1964.

[99] P. Carelli, M. G. Castellano, K. Flacco, R. Leoni, and G. Torrioli, "An absolute magnetometer based on dc superconducting QUantum interference devices," *Europhysics Letters (EPL)*, vol. 39, pp. 569–574, Sept. 1997.

[100] J. Beyer and D. Drung, "A SQUID series array dc current sensor," *Superconductor Science and Technology*, vol. 21, p. 095012, July 2008.

[101] J. Bardeen, "Tunnelling from a many-particle point of view," *Phys. Rev. Lett.*, vol. 6, no. 2, pp. 57–59, 1961.

[102] E. Bocquillon, R. S. Deacon, J. Wiedenmann, P. Leubner, T. M. Klapwijk, C. Brüne, K. Ishibashi, H. Buhmann, and L. W. Molenkamp, "Gapless Andreev bound states in the quantum spin Hall insulator HgTe," *Nat. Nanotechnol.*, vol. 12, no. 2, pp. 137–143, 2017.

[103] G. Tkachov and E. M. Hankiewicz, "Ballistic quantum spin hall state and enhanced edge backscattering in strong magnetic fields," *Physical Review Letters*, vol. 104, Apr. 2010.

[104] R. W. Keyes, "Physical limits of silicon transistors and circuits," *Reports Prog. Phys.*, vol. 68, no. 12, pp. 2701–2746, 2005.

[105] J. Mannhart and D. G. Schlom, "Oxide Interfaces - An Opportunity for Electronics," *Science*, vol. 327, no. March, pp. 1607–1611, 2010.

[106] D. Sánchez and H. Linke, "Focus on thermoelectric effects in nanostructures," *New Journal of Physics*, vol. 16, no. 11, p. 110201, 2014.

[107] S. Spilla, F. Hassler, and J. Splettstoesser, "Measurement and dephasing of a flux qubit due to heat currents," *New Journal of Physics*, vol. 16, no. 4, p. 045020, 2014.

[108] S. Spilla, F. Hassler, A. Napoli, and J. Splettstoesser, "Dephasing due to quasiparticle tunneling in fluxonium qubits: a phenomenological approach," *New Journal of Physics*, vol. 17, no. 6, p. 065012, 2015.

[109] H. L. Edwards, Q. Niu, G. A. Georgakis, and A. L. de Lozanne, "Cryogenic cooling using tunneling structures with sharp energy features," *Phys. Rev. B*, vol. 52, pp. 5714–5736, Aug 1995.

[110] J. P. Pekola, A. J. Manninen, M. M. Leivo, K. Arutyunov, J. K. Suoknuuti, T. I. Suppula, and B. Collaudin, "Microrefrigeration by quasiparticle tunnelling in NIS and SIS junctions," *Phys. B Condens. Matter*, vol. 280, no. 1-4, pp. 485–490, 2000.

[111] N. A. Miller, W. D. Duncan, J. A. Beall, G. C. Hilton, K. D. Irwin, D. R. Schmidt, and J. N. Ullom, "Development of a solid-state 100 mK refrigerator for user-supplied microelectronics," *Nucl. Instruments Methods Phys. Res. Sect. A Accel. Spectrometers, Detect. Assoc. Equip.*, vol. 559, no. 2, pp. 633–635, 2006.

[112] F. Giazotto, T. T. Heikkilä, A. Luukanen, A. M. Savin, and J. P. Pekola, "Opportunities for mesoscopics in thermometry and refrigeration: Physics and applications," *Rev. Mod. Phys.*, vol. 78, no. 1, pp. 217–274, 2006.

[113] I. Chowdhury, R. Prasher, K. Lofgreen, G. Chrysler, S. Narasimhan, R. Mahajan, D. Koester, R. Alley, and R. Venkatasubramanian, "On-chip cooling by superlattice-based thin-film thermoelectrics," *Nat. Nanotechnol.*, vol. 4, no. 4, pp. 235–238, 2009.

[114] F. Vischi, M. Carrega, P. Virtanen, E. Strambini, A. Braggio, and F. Giazotto, "Coherent Josephson thermodynamic cycles," *arXiv preprint*, pp. 1–16, 2018.

[115] N. Li, J. Ren, L. Wang, G. Zhang, P. Hänggi, and B. Li, "Colloquium: Phononics: Manipulating heat flow with electronic analogs and beyond," *Rev. Mod. Phys.*, vol. 84, no. 3, pp. 1045–1066, 2012.

[116] R. Bosisio, S. Valentini, F. Mazza, G. Benenti, R. Fazio, V. Giovannetti, and F. Taddei, "Magnetic thermal switch for heat management at the nanoscale," *Phys. Rev. B*, vol. 91, p. 205420, May 2015.

[117] F. Paolucci, G. Marchegiani, E. Strambini, and F. Giazotto, "Phase-tunable thermal logic: Computation with heat," *Phys. Rev. Applied*, vol. 10, p. 024003, Aug 2018.

[118] C. Guarcello, P. Solinas, A. Braggio, M. Di Ventra, and F. Giazotto, "Josephson thermal memory," *Phys. Rev. Applied*, vol. 9, p. 014021, Jan 2018.

[119] M. Meschke, W. Guichard, and J. P. Pekola, "Single-mode heat conduction by photons," *Nature*, vol. 444, no. 7116, pp. 187–190, 2006.

[120] A. Fornieri and F. Giazotto, "Towards phase-coherent caloritronics in superconducting circuits," *Nat. Nanotechnol.*, vol. 12, no. 10, pp. 944–952, 2017.

[121] P. Virtanen, F. Vischi, E. Strambini, M. Carrega, and F. Giazotto, "Quasiparticle entropy in superconductor/normal metal/superconductor proximity junctions in the diffusive limit," *Phys. Rev. B*, vol. 96, p. 245311, Dec 2017.

[122] C. Guarcello, A. Braggio, P. Solinas, and F. Giazotto, "Nonlinear critical-current thermal response of an asymmetric josephson tunnel junction," *Physical Review Applied*, vol. 11, Feb. 2019.

[123] G. Chen, "Nanoscale heat transfer and nanostructured thermoelectrics," *IEEE Trans. Components Packag. Technol.*, vol. 29, no. 2, pp. 238–246, 2006.

[124] R. Scheibner, M. König, D. Reuter, A. D. Wieck, C. Gould, H. Buhmann, and L. W. Molenkamp, "Quantum dot as thermal rectifier," *New Journal of Physics*, vol. 10, no. 8, p. 083016, 2008.

[125] X.-O. Chen, B. Dong, and L. X.-L., "Thermal rectification effect of an interacting quantum dot," *Chinese Physics Letters*, vol. 25, no. 8, p. 3032, 2008.

[126] D. M.-T. Kuo and Y.-C. Chang, "Thermoelectric and thermal rectification properties of quantum dot junctions," *Phys. Rev. B*, vol. 81, p. 205321, May 2010.

[127] T. Ruokola and T. Ojanen, "Single-electron heat diode: Asymmetric heat transport between electronic reservoirs through coulomb islands," *Phys. Rev. B*, vol. 83, p. 241404, Jun 2011.

[128] R. López and D. Sánchez, "Nonlinear heat transport in mesoscopic conductors: Rectification, peltier effect, and wiedemann-franz law," *Phys. Rev. B*, vol. 88, p. 045129, Jul 2013.

[129] F. Giazotto and F. S. Bergeret, "Thermal rectification of electrons in hybrid normal metal-superconductor nanojunctions," *Applied Physics Letters*, vol. 103, no. 24, p. 242602, 2013.

[130] M. J. Martínez-Pérez and F. Giazotto, "Efficient phase-tunable Josephson thermal rectifier," *Appl. Phys. Lett.*, vol. 102, no. 18, 2013.

[131] A. Fornieri, M. J. Martínez-Pérez, and F. Giazotto, "A normal metal tunnel-junction heat diode," *Appl. Phys. Lett.*, vol. 104, no. 18, 2014.

[132] M. J. Martínez-Pérez, A. Fornieri, and F. Giazotto, "Rectification of electronic heat current by a hybrid thermal diode," *Nat. Nano.*, vol. 10, no. 4, pp. 303–307, 2015.

[133] A. Fornieri, M. J. Martínez-Pérez, and F. Giazotto, "Electronic heat current rectification in hybrid superconducting devices," *AIP Advances*, vol. 5, no. 5, p. 053301, 2015.

[134] G. Granger, J. P. Eisenstein, and J. L. Reno, "Observation of chiral heat transport in the quantum hall regime," *Phys. Rev. Lett.*, vol. 102, p. 086803, Feb 2009.

[135] S.-G. Nam, E. H. Hwang, and H.-J. Lee, "Thermoelectric Detection of Chiral Heat Transport in Graphene in the Quantum Hall Regime," *Phys. Rev. Lett.*, vol. 110, no. 22, p. 226801, 2013.

[136] R. Sánchez, B. Sothmann, and A. N. Jordan, "Heat diode and engine based on quantum Hall edge states," *New J. Phys.*, vol. 17, no. 7, 2015.

[137] D. G. Rothe, E. M. Hankiewicz, B. Trauzettel, and M. Guigou, "Spin-dependent thermoelectric transport in hgte/cdte quantum wells," *Phys. Rev. B*, vol. 86, p. 165434, Oct 2012.

[138] J. Ren and J.-X. Zhu, "Anomalous energy transport across topological insulator superconductor junctions," *Phys. Rev. B*, vol. 87, p. 165121, Apr 2013.

[139] A. C. Durst, "Low-temperature thermal transport at the interface of a topological insulator and a d-wave superconductor," *Phys. Rev. B*, vol. 91, p. 094519, Mar 2015.

[140] H. Li and Y. Y. Zhao, "Thermal transport in topological-insulator-based superconducting hybrid structures with mixed singlet and triplet pairing states," *J. Phys. Condens. Matter*, vol. 29, no. 46, 2017.

[141] B. Rizzo, L. Arrachea, and M. Moskalets, "Transport phenomena in helical edge state interferometers: A green's function approach," *Phys. Rev. B*, vol. 88, p. 155433, Oct 2013.

[142] L. Vannucci, F. Ronetti, G. Dolcetto, M. Carrega, and M. Sassetti, "Interference-induced thermoelectric switching and heat rectification in quantum hall junctions," *Phys. Rev. B*, vol. 92, p. 075446, Aug 2015.

[143] F. Ronetti, M. Carrega, D. Ferraro, J. Rech, T. Jonckheere, T. Martin, and M. Sassetti, "Polarized heat current generated by quantum pumping in two-dimensional topological insulators," *Phys. Rev. B*, vol. 95, p. 115412, Mar 2017.

[144] J. A. Sauls, "Andreev bound states and their signatures," *Philosophical Transactions of the Royal Society A: Mathematical, Physical and Engineering Sciences*, vol. 376, p. 20180140, June 2018.

[145] G. De Simoni, F. Paolucci, P. Solinas, E. Strambini, and F. Giazotto, "Metallic supercurrent field-effect transistor," *Nat. Nano.*, vol. 13, pp. 802–805, 2018.

[146] F. London and H. London, "The electromagnetic equations of the supraconductor," *Proceedings of the Royal Society of London. Series A - Mathematical and Physical Sciences*, vol. 149, pp. 71–88, Mar. 1935.

[147] H. London and F. A. Lindemann, "An experimental examination of the electrostatic behaviour of supraconductors.," *Proceedings of the Royal Society A: Mathematical, Physical and Engineering Sciences*, vol. 155, pp. 102–110, May 1936.

[148] M. v. Laue, F. London, and H. London, "Zur theorie der supraleitung," *Zeitschrift für Physik*, vol. 96, pp. 359–364, May 1935.

[149] F. London, *Superfluids*. Wiley, New York, 1950.

[150] J. Bardeen, L. N. Cooper, and J. R. Schrieffer, "Theory of superconductivity," *Physical Review*, vol. 108, pp. 1175–1204, Dec. 1957.

[151] I. Landau, "Temperature dependence of the reflection coefficient of electrons on the interface between superconducting and normal phases," *JETP Lett. (USSR) (Engl. Transl.); (United States)*, vol. 11, 5 1970.

[152] A. B. Pippard, J. G. Shepherd, and D. A. Tindall, "Resistance of superconducting-normal interfaces," *Proceedings of the Royal Society of London. A. Mathematical and Physical Sciences*, vol. 324, pp. 17–35, July 1971.

[153] S. N. Artemenko and A. F. Volkov, "Electric fields and collective oscillations in superconductors," *Soviet Physics Uspekhi*, vol. 22, pp. 295–310, May 1979.

[154] T. J. Rieger, D. J. Scalapino, and J. E. Mercereau, "Charge conservation and chemical potentials in time-dependent ginzburg-landau theory," *Physical Review Letters*, vol. 27, pp. 1787–1790, Dec. 1971.

[155] N. Kopnin and O. U. Press, *Theory of Nonequilibrium Superconductivity*. International Series of Monographs on Physics, Clarendon Press, 2001.

[156] R. Moro, "Ferroelectricity in free niobium clusters," *Science*, vol. 300, pp. 1265–1269, May 2003.

[157] R. Tao, X. Xu, Y. Lan, and Y. Shiroyanagi, "Electric-field induced low temperature superconducting granular balls," *Physica C: Superconductivity*, vol. 377, pp. 357–361, Sept. 2002.

[158] X. X. Xi, C. Doughty, A. Walkenhorst, C. Kwon, Q. Li, and T. Venkatesan, "Effects of field-induced hole-density modulation on normal-state and superconducting transport inYBa2cu3o7-x," *Physical Review Letters*, vol. 68, pp. 1240–1243, Feb. 1992.

[159] T. Frey, J. Mannhart, J. G. Bednorz, and E. J. Williams, "Mechanism of the electric-field effect in the high-tccuprates," *Physical Review B*, vol. 51, pp. 3257–3260, Feb. 1995.

[160] C. H. Ahn, J.-M. Triscone, and J. Mannhart, "Electric field effect in correlated oxide systems," *Nature*, vol. 424, pp. 1015–1018, Aug. 2003.

[161] K. K. Likharev, "Superconducting weak links," *Rev. Mod. Phys.*, vol. 51, pp. 101–159, Jan 1979.

[162] F. Paolucci, G. De Simoni, E. Strambini, P. Solinas, and F. Giazotto, "Ultra-efficient superconducting dayem bridge field-effect transistor," *Nano lett.*, vol. 18, pp. 4195–4199, 2018.

[163] F. Paolucci, G. De Simoni, P. Solinas, E. Strambini, N. Ligato, P. Virtanen, A. Braggio, and F. Giazotto, "Magnetotransport experiments

on fully metallic superconducting dayem-bridge field-effect transistors," *Phys. Rev. Applied*, vol. 11, p. 024061, Feb 2019.

[164] G. D. Simoni, C. Puglia, and F. Giazotto, "Niobium dayem nano-bridge josephson gate-controlled transistors," *Applied Physics Letters*, vol. 116, p. 242601, June 2020.

[165] C. Puglia, G. D. Simoni, N. Ligato, and F. Giazotto, "Vanadium gate-controlled josephson half-wave nanorectifier," 2020.

[166] G. De Simoni, F. Paolucci, C. Puglia, and F. Giazotto, "Field-effect controllable metallic josephson interferometer," *Nano lett.*, vol. 13, pp. 7871–7876, 2019.

[167] F. Paolucci, F. Vischi, G. De Simoni, C. Guarcello, P. Solinas, and F. Giazotto, "Field-effect controllable metallic josephson interferometer," *Nano lett.*, vol. 19, pp. 6263–6269, 2019.

[168] C. Puglia, G. De Simoni, and F. Giazotto, "Electrostatic control of phase slips in Ti josephson nanotransistors," *Phys. Rev. Applied*, vol. 13, p. 054026, May 2020.

[169] M. Rocci, G. D. Simoni, C. Puglia, D. D. Esposti, E. Strambini, V. Zannier, L. Sorba, and F. Giazotto, "Gate-controlled suspended titanium nanobridge supercurrent transistor," *ACS Nano*, Aug. 2020.

[170] M. F. Ritter, A. Fuhrer, D. Z. Haxell, S. Hart, P. Gumann, H. Riel, and F. Nichele, "A superconducting switch actuated by injection of high energy electrons," 2020.

[171] L. D. Alegria, C. G. Bøttcher, A. K. Saydjari, A. T. Pierce, S. H. Lee, S. P. Harvey, U. Vool, and A. Yacoby, "High-energy quasiparticle injection in mesoscopic superconductors," 2020.

[172] R. H. Fowler and L. Nordheim, "Electron emission in intense electric fields," *Proceedings of the Royal Society of London. Series A, Containing Papers of a Mathematical and Physical Character*, vol. 119, pp. 173–181, May 1928.

[173] P. Virtanen, A. Braggio, and F. Giazotto, "Superconducting size effect in thin films under electric field: Mean-field self-consistent model," *Physical Review B*, vol. 100, Dec. 2019.

[174] F. Paolucci, G. D. Simoni, P. Solinas, E. Strambini, C. Puglia, N. Ligato, and F. Giazotto, "Field-effect control of metallic superconducting systems," *AVS Quantum Science*, vol. 1, p. 016501, Dec. 2019.

[175] J. L. Levine and S. Y. Hsieh, "Recombination time of quasiparticles in superconducting aluminum," *Phys. Rev. Lett.*, vol. 20, pp. 994–997, Apr 1968.

[176] L. N. Smith and J. M. Mochel, "Phonon and quasiparticle dynamics in superconducting aluminum tunnel junctions," *Phys. Rev. Lett.*, vol. 35, pp. 1597–1600, Dec 1975.

[177] A. F. Morpurgo, T. M. Klapwijk, and B. J. van Wees, "Hot electron tunable supercurrent," *Applied Physics Letters*, vol. 72, pp. 966–968, Feb. 1998.

[178] J. N. Ullom, P. A. Fisher, and M. Nahum, "Measurements of quasiparticle thermalization in a normal metal," *Phys. Rev. B*, vol. 61, pp. 14839–14843, Jun 2000.

[179] I. Golokolenov, A. Guthrie, S. Kafanov, Y. Pashkin, and V. Tsepelin, "On the origin of the controversial electrostatic field effect in superconductors," 2020.

[180] M. Rocci, D. Suri, A. Kamra, G. Vilela, N. M. Nemes, J. L. Martinez, M. G. Hernandez, and J. S. Moodera, "Large enhancement of critical current in superconducting devices by gate voltage," 2020.

[181] J. S. Langer and V. Ambegaokar, "Intrinsic resistive transition in narrow superconducting channels," *Physical Review*, vol. 164, pp. 498–510, Dec. 1967.

[182] W. A. Little, "Decay of persistent currents in small superconductors," *Physical Review*, vol. 156, pp. 396–403, Apr. 1967.

[183] T. Sato, G. Masuda, and K. Takagi, "Electrochemical properties of novel ionic liquids for electric double layer capacitor applications," *Electrochimica Acta*, vol. 49, pp. 3603–3611, Sept. 2004.

[184] M. J. Panzer, C. R. Newman, and C. D. Frisbie, "Low-voltage operation of a pentacene field-effect transistor with a polymer electrolyte gate dielectric," *Applied Physics Letters*, vol. 86, p. 103503, Mar. 2005.

[185] A. S. Dhoot, J. D. Yuen, M. Heeney, I. McCulloch, D. Moses, and A. J. Heeger, "Beyond the metal-insulator transition in polymer electrolyte gated polymer field-effect transistors," *Proceedings of the National Academy of Sciences*, vol. 103, pp. 11834–11837, July 2006.

[186] R. Misra, M. McCarthy, and A. F. Hebard, "Electric field gating with ionic liquids," *Applied Physics Letters*, vol. 90, p. 052905, Jan. 2007.

[187] H. Shimotani, H. Asanuma, A. Tsukazaki, A. Ohtomo, M. Kawasaki, and Y. Iwasa, "Insulator-to-metal transition in ZnO by electric double layer gating," *Applied Physics Letters*, vol. 91, p. 082106, Aug. 2007.

[188] D. K. Efetov and P. Kim, "Controlling electron-phonon interactions in graphene at ultrahigh carrier densities," *Physical Review Letters*, vol. 105, Dec. 2010.

[189] R. S. Gonnelli, F. Paolucci, E. Piatti, K. Sharda, A. Sola, M. Tortello, J. R. Nair, C. Gerbaldi, M. Bruna, and S. Borini, "Temperature dependence of electric transport in few-layer graphene under large charge doping induced by electrochemical gating," *Scientific Reports*, vol. 5, Apr. 2015.

[190] A. S. Dhoot, S. C. Wimbush, T. Benseman, J. L. MacManus-Driscoll, J. R. Cooper, and R. H. Friend, "Increased tc in electrolyte-gated cuprates," *Advanced Materials*, vol. 22, pp. 2529–2533, May 2010.

[191] J. Choi, R. Pradheesh, H. Kim, H. Im, Y. Chong, and D.-H. Chae, "Electrical modulation of superconducting critical temperature in liquid-gated thin niobium films," *Applied Physics Letters*, vol. 105, p. 012601, July 2014.

[192] T. Tsuchiya, S. Moriyama, K. Terabe, and M. Aono, "Modulation of superconducting critical temperature in niobium film by using all-solid-state electric-double-layer transistor," *Applied Physics Letters*, vol. 107, p. 013104, July 2015.

[193] E. Piatti, A. Sola, D. Daghero, G. A. Ummarino, F. Laviano, J. R. Nair, C. Gerbaldi, R. Cristiano, A. Casaburi, and R. S. Gonnelli, "Superconducting transition temperature modulation in NbN via EDL gating," *Journal of Superconductivity and Novel Magnetism*, vol. 29, pp. 587–591, Dec. 2015.

[194] E. Piatti, D. Daghero, G. A. Ummarino, F. Laviano, J. R. Nair, R. Cristiano, A. Casaburi, C. Portesi, A. Sola, and R. S. Gonnelli, "Control of bulk superconductivity in a BCS superconductor by surface charge doping via electrochemical gating," *Physical Review B*, vol. 95, Apr. 2017.

[195] J. Bardeen, "Critical fields and currents in superconductors," *Rev. Mod. Phys.*, vol. 34, pp. 667–681, Oct 1962.

[196] Y.-d. Song and G. I. Rochlin, "Transition from bulklike behavior to josephson-junction—like behavior in superconducting microbridges," *Phys. Rev. Lett.*, vol. 29, pp. 416–419, Aug 1972.

[197] S. Khlebnikov, "Metastability and bifurcation in superconducting nanorings," *Phys. Rev. B*, vol. 95, p. 174507, May 2017.

[198] W. J. Skocpol, M. R. Beasley, and M. Tinkham, "Self-heating hotspots in superconducting thin-film microbridges," *Journal of Applied Physics*, vol. 45, no. 9, pp. 4054–4066, 1974.

[199] H. Courtois, M. Meschke, J. T. Peltonen, and J. P. Pekola, "Origin of hysteresis in a proximity josephson junction," *Phys. Rev. Lett.*, vol. 101, p. 067002, Aug 2008.

[200] D. Hazra, J. R. Kirtley, and K. Hasselbach, "Retrapping current in bridge-type nano-squids," *Phys. Rev. Applied*, vol. 4, p. 024021, Aug 2015.

[201] P. Fulde, "High field superconductivity in thin films," *Advances in Physics*, vol. 22, no. 6, pp. 667–719, 1973.

[202] B. S. Chandrasekhar, "A note on the maximum critical field of high-field superconductos," *Applied Physics Letters*, vol. 1, no. 1, pp. 7–8, 1962.

[203] P. W. Adams, H. Nam, C. K. Shih, and G. Catelani, "Zeeman-limited superconductivity in crystalline al films," *Phys. Rev. B*, vol. 95, p. 094520, Mar 2017.

[204] M. T. Mercaldo, P. Solinas, F. Giazotto, and M. Cuoco, "Electrically tunable superconductivity through surface orbital polarization," *Phys. Rev. Applied*, vol. 14, p. 034041, Sep 2020.

[205] W. D. Oliver and P. B. Welander, "Materials in superconducting quantum bits," *MRS Bulletin*, vol. 38, no. 10, p. 816–825, 2013.

[206] Y. Makhlin, G. Schön, and A. Shnirman, "Quantum-state engineering with josephson-junction devices," *Rev. Mod. Phys.*, vol. 73, pp. 357–400, May 2001.

[207] J. P. Pekola, O.-P. Saira, V. F. Maisi, A. Kemppinen, M. Möttönen, Y. A. Pashkin, and D. V. Averin, "Single-electron current sources: Toward a refined definition of the ampere," *Rev. Mod. Phys.*, vol. 85, pp. 1421–1472, Oct 2013.

[208] Z.-L. Xiang, S. Ashhab, J. Q. You, and F. Nori, "Hybrid quantum circuits: Superconducting circuits interacting with other quantum systems," *Rev. Mod. Phys.*, vol. 85, pp. 623–653, Apr 2013.

[209] A. Holland, G. Fraser, P. Roth, S. Trowell, E. Gu, R. Hart, P. Brink, and S. Guy, "Transition edge sensors for x-ray astronomy," *Nuclear*

Instruments and Methods in Physics Research Section A: Accelerators, Spectrometers, Detectors and Associated Equipment, vol. 436, pp. 226–232, Oct. 1999.

[210] T. M. Klapwijk and A. V. Semenov, "Engineering physics of superconducting hot-electron bolometer mixers," *IEEE Transactions on Terahertz Science and Technology*, vol. 7, pp. 627–648, Nov 2017.

[211] A. Anthore, H. Pothier, and D. Esteve, "Density of states in a superconductor carrying a supercurrent," *Phys. Rev. Lett.*, vol. 90, Mar. 2003.

[212] V. F. Maisi, S. V. Lotkhov, A. Kemppinen, A. Heimes, J. T. Muhonen, and J. P. Pekola, "Excitation of single quasiparticles in a small superconducting al island connected to normal-metal leads by tunnel junctions," *Phys. Rev. Lett.*, vol. 111, p. 147001, Oct 2013.

[213] M. Tinkham, *Introduction to superconductivity*. Courier Dover Publications, 1976.

[214] G. Sarma, "On the influence of a uniform exchange field acting on the spins of the conduction electrons in a superconductor," *Journal of Physics and Chemistry of Solids*, vol. 24, no. 8, pp. 1029 – 1032, 1963.

[215] F. S. Bergeret, M. Silaev, P. Virtanen, and T. T. Heikkilä, "Colloquium: Nonequilibrium effects in superconductors with a spin-splitting field," *Rev. Mod. Phys.*, vol. 90, p. 041001, Oct 2018.

[216] S. R. Park, C. H. Kim, J. Yu, J. H. Han, and C. Kim, "Orbital-angular-momentum based origin of rashba-type surface band splitting," *Phys. Rev. Lett.*, vol. 107, p. 156803, Oct 2011.

[217] J.-H. Park, C. H. Kim, J.-W. Rhim, and J. H. Han, "Orbital rashba effect and its detection by circular dichroism angle-resolved photoemission spectroscopy," *Phys. Rev. B*, vol. 85, p. 195401, May 2012.

[218] B. Kim, P. Kim, W. Jung, Y. Kim, Y. Koh, W. Kyung, J. Park, M. Matsunami, S.-i. Kimura, J. S. Kim, J. H. Han, and C. Kim, "Microscopic mechanism for asymmetric charge distribution in rashba-type surface states and the origin of the energy splitting scale," *Phys. Rev. B*, vol. 88, p. 205408, Nov 2013.

Acknowledgements

Western culture has a tendency to focus on the person, to ascribe achievements to the individual. While it makes for a neat picture of the world, this is of course a bit of nonsense. No one, no matter how genius, talented, or hard working, would achieve anything in a void, and I cannot in good conscience claim those predicates. Therefore, I want to thank and acknowledge the many people that have made my PhD possible in one way or another.

First of all, Francesco, thank you for offering me the opportunity to work in your research group, for guiding my research, and for always pushing me forward. Secondly, Elia. Thank you for always being available to help me with matters big and small, for all that you taught me about doing measurements and science, and for all the useful advise you have given me through the years. I fear I would need another PhD to learn everything you could teach me. To both of you: thank extending your trust to me, and for letting me make my own mistakes.

Moving on, I want to thank the people who have contributed to my published works. That is: Matteo Carrega, Alessandro Braggio, Björn Sothmann, Ewelina hankiewicz, Maria-Teresa Mercaldo, and Mario Cuoco. I am happy to look back on fruitful and pleasant collaborations with all of you, and I could not have produced any of the papers without your help.

I want to thank everyone in the research group for welcoming me, even though you had to speak English just for me. Maria, you joined our group during a bad time, but together with Andrea we made the most out of it, and I greatly enjoyed our trips together. Furthermore, I want to thank the people with whom I shared more than just an office. Giuliano, Giampiero, Claudio, Francesco and Andrea, I am extremely grateful for the many fun discussions, trips, cups of tea, ups, and downs we had together. Without you, I would have never learned how to curse and swear in Italian, so thank you for that. And also for the slightly less offensive language I learned from you, I guess...

There is more to life than work, and for that reason I want to mention the friends I made outside of the group as well. Manuela, Nadia, William, Keagan, Shelly, Leonardo and Federica, thank you for all the nice meals, parties and gossip.

In a similar vein, I want to thank the friends back home in The Netherlands. It was a blast to have you all come and visit me throughout the years, and even though I have been to Cinque Terre 20 times, I would happily go 20 times more with you. Moreover, due to our frequent game nights I never felt alone. In particular I thank Edo for the wonderful thesis cover he graciously designed for me.

I want to thank my family from the bottom of my heart. Mom, Dad, Dewi, Madelon and Andreas, thank you for your support and faith in me.

Finally, Didi. Thank you for coming here on this adventure with me. Thank you for dragging me up and down mountains. Thank you for loving me.

Tiger got to sleep
Bird got to land
Man got to tell himself
he understand

— Kurt Vonnegut